

Search for decay $\Upsilon(5S) \rightarrow \gamma W_{bJ}$

Nicholas Corrado, Vladimir Savinov

University of Pittsburgh, Pittsburgh, PA-15260, USA

Abstract

The recent discovery of the states Z_b and Z'_b implies the possible existence of a new family of hadronic resonances including molecular states dubbed W_{bJ} . We describe a search for W_{bJ} in the decay $\Upsilon(5S) \rightarrow \gamma W_{bJ}$ using 121.4 fb^{-1} of data collected at the $\Upsilon(5S)$ resonance with the Belle detector at the KEKB asymmetric-energy electron-positron collider. Using Monte Carlo simulation, we study Belle's sensitivity to the decay $\Upsilon(5S) \rightarrow \gamma W_{bJ}$, search for its presence in Belle data and describe the procedure we would use to establish an upper limit on the visible production cross section for these new states.

16 Contents

17	1 Introduction	1
18	1.1 Motivation	1
19	1.2 New Spectroscopy	1
20	1.3 Radiative Decays $\Upsilon(5S) \rightarrow \gamma W_{bJ}$	3
21	1.4 Expected Signal in Data	4
22	2 Monte Carlo and Data Samples	6
23	3 Selection Criteria	6
24	3.1 Selection of Photon Candidates	7
25	3.2 Selection of Pion and Muon Candidates	8
26	3.3 Selection of $\Upsilon(5S)$ Candidates	8
27	3.4 Best Candidate Selection	8
28	4 Signal Monte Carlo Studies	8
29	4.1 Signal Monte Carlo Distributions	8
30	4.2 Description of the Signal Region	12
31	4.3 Trigger Simulation	15
32	5 Background Studies	18
33	5.1 Generic Monte Carlo and Blinded Data	18
34	6 Background from $\Upsilon(5S) \rightarrow \Upsilon(1S)\pi^+\pi^-$ with Initial State Radiation (ISR)	20
35	6.1 $\Upsilon(5S) \rightarrow \Upsilon(1S)\pi^+\pi^-$ ISR Monte Carlo Sample	20
36	6.2 Background Shape of $\Upsilon(5S) \rightarrow \Upsilon(1S)\pi^+\pi^-$ with ISR	22
37	7 Contribution from $\Upsilon(5S) \rightarrow Z_b^{(\prime)\pm}\pi^\mp$	26
38	8 Fitting	26
39	8.1 Signal and Background PDFs	26
40	8.2 Confidence Belts	28
41	8.3 Linearity Study	29
42	8.4 Sensitivity Estimation	31
43	9 Search Strategy Summary	33
44	10 Appendix	34
45	10.1 Final State Radiation	34
46	10.2 Changes in the Analysis between Note v1.5 and v2.0	35
47	10.2.1 Signal Photon Energy Conundrum	36
48	10.3 Fitting Strategy	41

49 List of Figures

50	1	Pure $b\bar{b}$ bottomonium mass spectrum for a relativized quark model	2
51	2	Spectrum of bottomonium and bottomonium-like mesons.	3
52	3	Expected family of molecular isotriplet resonances.	5
53	4	Various MC distributions which informed our selection criteria.	7
54	5	Signal MC distributions	10
55	6	$M(\pi^+\pi^+\mu^+\mu^-)$ and $M(\pi^+\pi^-(\mu^+\mu^-)_{\text{fit}})$ resolutions for signal events	11
56	7	ΔE resolution and quantities contributing to ΔE resolution.	12
57	8	Definitions of important regions	14
58	9	Offline trigger selection for reconstructed signal MC events.	16
59	10	Offline trigger efficiency for reconstructed signal MC events.	17
60	11	Identifying background present in data but not in generic MC.	18
61	12	Motivation for ISR studies.	20
62	13	Reweighted ISR energy spectrum	21
63	14	Background due to ISR.	22
64	15	Effect of decay models on $M(\pi^+\pi^-(\mu^+\mu^-)_{\text{fit}})$ distribution.	23
65	16	Effect of decay models on muon angular distribution.	24
66	17	Effect of ΔE cut on ISR background shape.	25
67	18	Definitions of subdivisions of the grand sideband region	25
68	19	Distribution of $M(\pi^+\pi^-(\mu^+\mu^-)_{\text{fit}})$ vs $M_{\text{rec}}(\gamma)$ for $\Upsilon(5S) \rightarrow Z_b^{(\prime)\pm}\pi^\mp$ MC	27
69	20	Distribution of $M(\pi^+\pi^-(\mu^+\mu^-)_{\text{fit}})$ for $\Upsilon(5S) \rightarrow Z_b^{(\prime)\pm}\pi^\mp$	27
70	21	Fitting background MC and data	29
71	22	90% confidence belts for frequentist method.	30
72	23	Average $N_{\text{sig}}^{\text{fit}}$ for varying values of $N_{\text{sig}}^{\text{gen}}$. The solid black line is the result of fitting these points to the linear function $f(x) = p_0 + p_1x$. The resulting fit parameters are shown in the box on the top right.	31
73			
74			
75	24	$N_{\text{sig}}^{\text{fit}}$ Distributions for ensemble tests with different $N_{\text{sig}}^{\text{gen}}$	32
76	25	Final state radiation from charged tracks	34
77	26	Signal invariant mass for a special MC sample with the original selection criteria.	38
78	27	Photon energy vs signal invariant mass for a special MC sample with the original selection criteria.	39
79			
80	28	Photon energy vs signal invariant mass for a special MC sample with relaxed selection criteria.	40
81			
82	29	Signal invariant mass for a special MC sample with relaxed selection criteria.	41
83	30	Signal invariant mass for a special MC sample with relaxed selection criteria (log scale).	42
84			
85	31	Photon energy vs signal invariant mass for blinded data with relaxed selection criteria.	43
86			
87	32	Signal invariant mass for blinded data with relaxed selection criteria.	44
88	33	Signal invariant mass for blinded data with relaxed selection criteria (log scale).	45
89	34	Signal invariant mass for blinded data with relaxed selection criteria (log scale, finer bins).	46
90			
91	35	Signal invariant mass for blinded data with relaxed selection criteria (log scale, fitting region).	47
92			

93	36	Photon energy vs signal invariant mass for ISR MC sample described in section 6 with relaxed selection criteria.	48
94			
95	37	Signal invariant mass for ISR MC sample described in section 6 with relaxed selection criteria.	49
96			
97	38	Signal invariant mass for ISR MC sample described in section 6 with relaxed selection criteria (log scale).	50
98			
99	39	Signal invariant mass for ISR MC sample described in section 6 with relaxed selection criteria (log scale, fitting region only).	51
100			
101	40	The results of the ML fit for ISR MC sample.	52
102	41	The results of the ML fit for ISR MC sample excluding the signal region. . .	52
103	42	The results of the ML fit for sidebands of the blinded data sample.	53
104	43	The results of the ML fit for ISR MC sample with background model and signal PDF shape.	53
105			
106	44	The results of the ML fit for ISR MC sample with background model and signal PDF shape (mass is a free parameter).	54
107			
108	45	The results of the ML fit for ISR + signal (50 events) MC sample with background model and signal PDF shape (mass is a free parameter).	54
109			
110	46	The results of the scan for ISR MC sample with background model and signal PDF shape.	55
111			
112	47	The results of the scan for ISR MC sample + 50 toy MC signal events with background model and signal PDF shape.	55
113			

114 **List of Tables**

115	1	Possible molecular isotriplet states in decays of $\Upsilon(5S)$ and $\Upsilon(6S)$	4
116	2	EvtGen decay models used in Monte Carlo simulation of signal processes. . .	6
117	3	Selection criteria for $\Upsilon(5S) \rightarrow \gamma W_{bJ}$	9
118	4	Quantities contributing to widths of measured quantities	10
119	5	Definitions of the signal region and other important regions.	13
120	6	Backgrounds labeled in Fig. 11.	19
121	7	Decay models used in background ISR MC	22
122	8	Definitions of subdivisions of the grand sideband region	24
123	9	Comparing the number of events in ISR MC and blinded data in the subdivided grand sideband region	26
124			
125	10	Values of fixed quantities in the signal PDF model	28
126	11	Values of quantities used in upper limit calculation	33
127	12	The new (wider) blinded region in data. The important change is shown in	
128		red color. However, it is redundant and adds nothing new as compared to the	
129		second line in this table.	36

1 Introduction

Version 1.5 of this Note includes new plots, various corrections suggested and the answers to the questions asked by the referees. Also, this version includes two new appendices: section 10.2, “Changes in the Analysis between Note v1.5 and v2.0” and section 10.3, “Fitting Strategy”. Note that the plots in the main part of the note (*i.e.* excluding the plots in the Appendix part) have been prepared using the original analysis. The changes outlined in the section 10.2 and used for preparing plots in sections 10.2 and 10.3, have not yet been applied to the main body of the text of this Note.

1.1 Motivation

In this document, we describe a search for new hadronic states of matter – bottomonium-like particles dubbed W_{bJ} – in radiative decays of $\Upsilon(5S)$. These states are believed to be of molecular nature, where a pair of colored $B_{(s)}^{(*)}$ mesons, each containing a b or an anti- b quark, are held together by the strong interaction (in a way similar to single-pion exchange force mechanism in QCD-inspired low-energy models). As with conventional bottomonium, *i.e.* $b\bar{b}$ states, these molecular states exhibit their own spectroscopy. However, their masses and properties obviously could not be predicted using $q\bar{q}$ potential models. We are motivated by Belle’s discoveries [1, 2, 3, 4] of the $Z_b(10610)$ and $Z_b(10650)$ states (referred to in the rest of this document as Z_b and Z'_b or just Z_b) and theoretical predictions which use the molecular picture to explain the nature of the Z_b and predict the existence of additional hadronic states. These predictions can be used to explain various long-standing puzzles in the (no longer pure) bottomonium at energies above the threshold for B meson pair production.

1.2 New Spectroscopy

Since the discovery of the Υ meson, the b quark, and B mesons [5], conventional bottomonium states have been a rich source of information about strong interaction dynamics in the approximately non-relativistic $b\bar{b}$ system. Vector bottomonium and bottomonium-like states ($\Upsilon(nS)$ mesons) can be produced directly in the e^+e^- annihilation. Three of these states – $\Upsilon(1S)$, $\Upsilon(2S)$, and $\Upsilon(3S)$ – have masses below the $B\bar{B}$ threshold [6]. These states are believed to be pure $b\bar{b}$, and their properties are relatively easy to understand using potential models. Such relativized models [7] predict 34 $b\bar{b}$ bound states below $\Upsilon(4S)$ energy, 15 of which have been observed. We show the predictions for the energy levels in the $b\bar{b}$ spectroscopy [8, 9] in Fig. 1.

Hadronic transitions (such as, *e.g.* $\Upsilon(3S) \rightarrow \pi^+\pi^-\Upsilon(1S)$) between bottomonium states provide an excellent opportunity to study QCD dynamics in non-perturbative regime by comparing the measured masses, widths, branching fractions, angular and invariant mass distributions with the theoretical predictions. For pure bottomonium states – $b\bar{b}$ resonances below $B\bar{B}$ threshold – the hadronic transitions proceed via radiating the strong field, *i.e.*, by emitting the gluons which convert into light hadrons. States above $B\bar{B}$ threshold, starting with $\Upsilon(4S)$, are significantly wider than the lower-mass states, and their hadronic transitions are known to exhibit certain properties that are unexpected for pure $b\bar{b}$ states. While the latter are well described from the perspective of Heavy Quark Spin Symmetry (HQSS) where

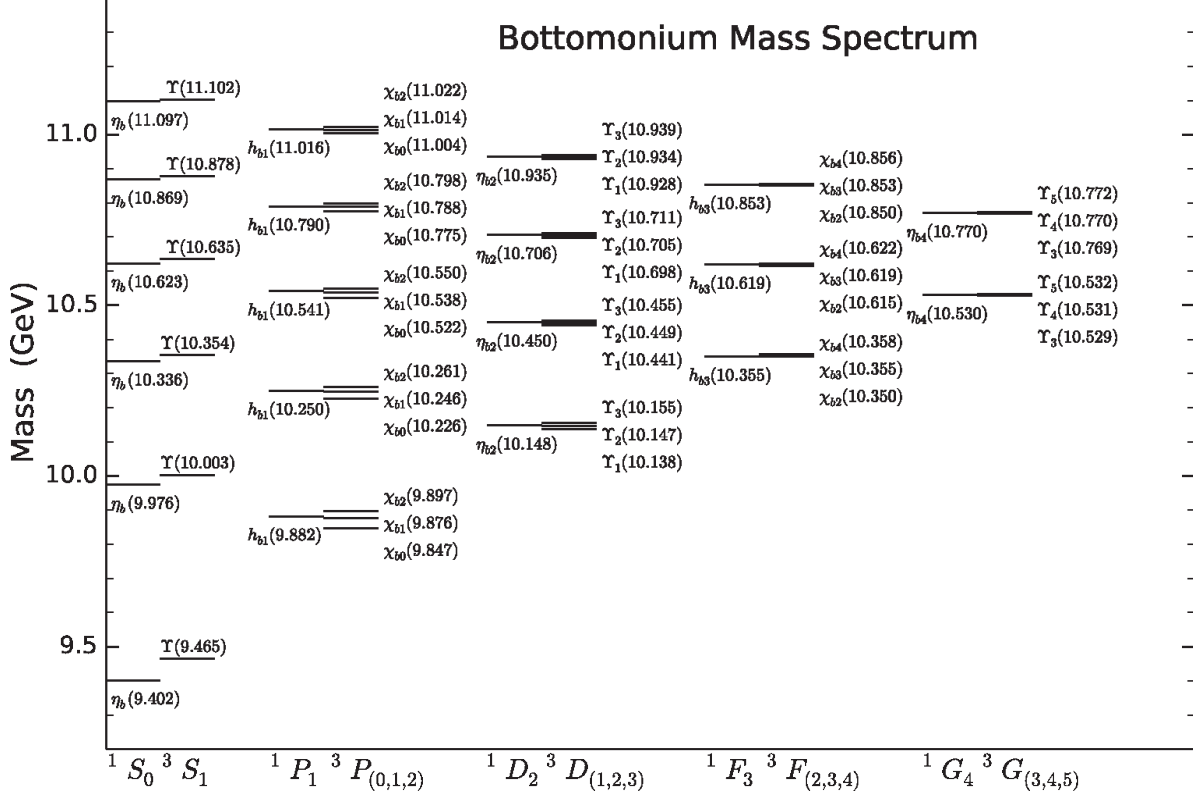


Figure 1: Pure (*i.e.* $b\bar{b}$) bottomonium mass spectrum [8] calculated using a relativized quark model [7].

170 transitions involving the spin of the heavy b quark are strongly suppressed, the former states,
171 including the $\Upsilon(5S)$, require a different explanation [10].

172 The favored explanation for the properties of $\Upsilon(5S)$, including its decays to Z_b , is based
173 on the molecular picture, where these vector bottomonium-like resonances are assumed to
174 contain an admixture of pairs of colored heavy mesons. This hypothesis has been successfully
175 employed [11] to explain the decays to and the existence of the six Z_b states. However,
176 the details of the interaction responsible for these processes are not yet fully understood.
177 Alternative explanations include a model with a diquark-antidiquark pair, where a pair of
178 quarks and a pair of antiquarks are each bound with a stronger force than the force holding
179 diquark and antidiquark together. While the search described in this document is model-
180 independent, our motivation is somewhat biased in favor of the molecular picture and has
181 likely impacted our decisions about how to perform the analysis.

182 The main goal of our study is to test some of the predictions of the new spectroscopy [12]
183 that predicts energy levels for the molecular bottomonium-like states depicted in Fig. 2,
184 Namely, we describe a search for the partner states of Z_b , referred to as W_{bJ} , and we aim to
185 obtain new information about hadronic dynamics in presence of the heavy b quarks. Improv-
186 ing the current understanding of such dynamics is of paramount importance for being able to
187 use the hadronic decays of B mesons to extract possible contributions from the Beyond-the-
188 Standard-Model (BSM) amplitudes, where the interplay between the strong interaction and
189 the new BSM weak phases could not be reliably understood without the precise theoretical

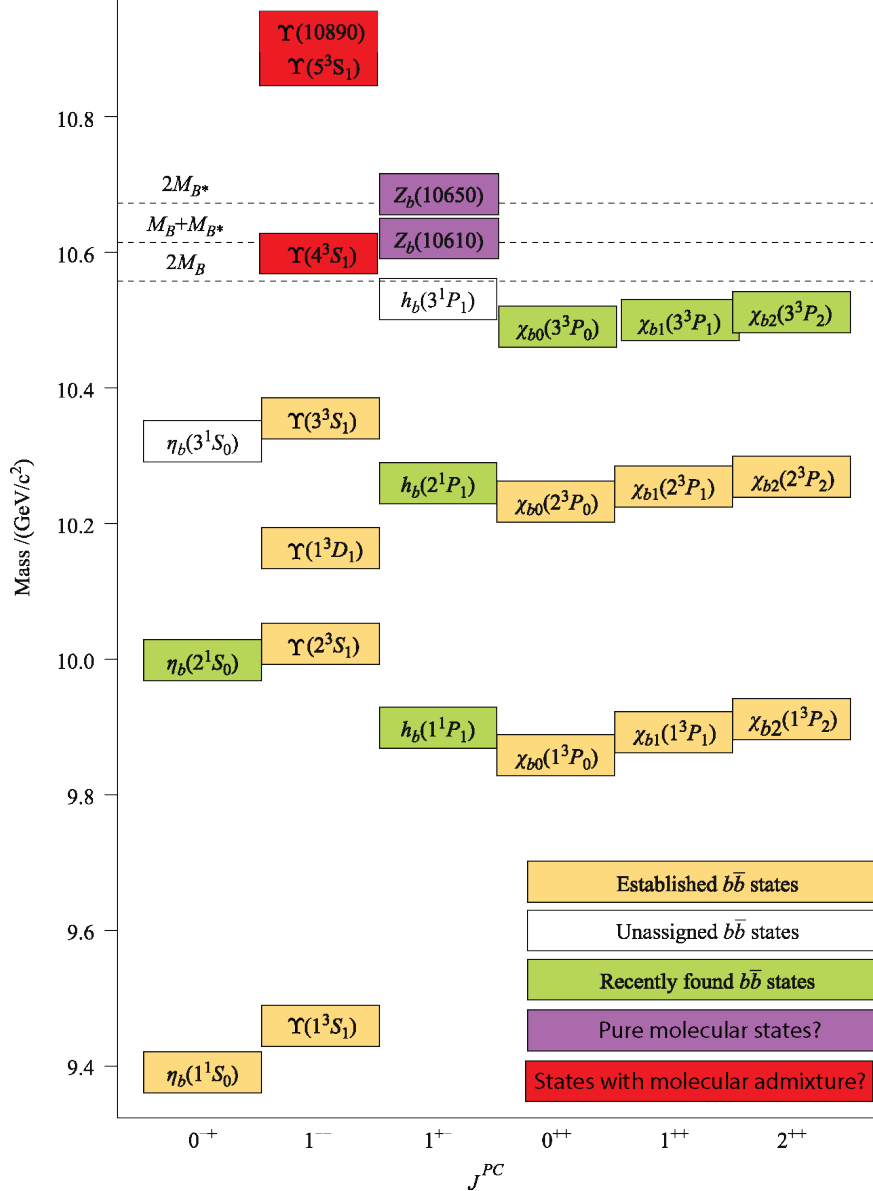


Figure 2: Most relevant (for our study) states in conventional bottomonium and bottomonium-like spectroscopies. We stole this figure from S. Olsen’s excellent review article [12]. Note that we took liberty to modify the original figure to better represent the contents of this Note, namely, we relabeled $\Upsilon(nS)$ ($n = 4, 5, 6$) as “States with molecular admixture?” and Z_b states as “Pure molecular states?”.

190 predictions for the QCD part.

191 1.3 Radiative Decays $\Upsilon(5S) \rightarrow \gamma W_{bJ}$

192 The Z_b states were discovered in single-pion transitions of $\Upsilon(5S)$ and $\Upsilon(6S)$, followed by
 193 another single-pion transition to the bottomonium states. According to molecular interpre-
 194 tation, $Z_b(10610)$ is primarily a $B\bar{B}^*$ state, while $Z_b(10650)$ (a.k.a. Z'_b) is a $B^*\bar{B}^*$ state.

$I^G(J^P)$	Name	Co-produced with (threshold, GeV/c ²)	Assumed composition	Decay channels
1 ⁺ (1 ⁺)	$Z_b(10610)$	π (10.75)	$B\bar{B}^*$	$\Upsilon(nS)\pi, h_b(nP)\pi, \eta_b(nS)\rho$
1 ⁺ (1 ⁺)	$Z'_b(10650)$	π (10.79)	$B^*\bar{B}^*$	$\Upsilon(nS)\pi, h_b(nP)\pi, \eta_b(nS)\rho$
1 ⁻ (0 ⁺)	W_{b0}	ρ (11.34), γ (10.56)	$B\bar{B}$	$\Upsilon(nS)\rho, \eta_b(nS)\pi, \chi_{b\pi}$
1 ⁻ (0 ⁺)	W'_{b0}	ρ (11.43), γ (10.65)	$B^*\bar{B}^*$	$\Upsilon(nS)\rho, \eta_b(nS)\pi, \chi_{b\pi}$
1 ⁻ (1 ⁺)	W_{b1}	ρ (11.38), γ (10.61)	$B\bar{B}^*$	$\Upsilon(nS)\rho, \chi_{b\pi}$
1 ⁻ (2 ⁺)	W_{b2}	ρ (11.43), γ (10.65)	$B^*\bar{B}^*$	$\Upsilon(nS)\rho, \chi_{b\pi}$

Table 1: Molecular isotriplet states which could be produced in the decays of $\Upsilon(5S)$ and $\Upsilon(6S)$ according to [10]. Note that the ρ could be replaced by a photon in the decays of $I_3 = 0$ states, but this would suppress the expected rate even more. Please see Fig. 3 as well.

195 Z_b are spin-1 isotriplets (both neutral and charged states were discovered in transitions
196 $\Upsilon(nS) \rightarrow \pi Z_b$ ($n = 5, 6$). The hypothetical partners of positive G -parity states Z_b , *i.e.* the
197 W_{bJ} states, would also be isotriplets but of negative G -parity (quantum numbers of the new
198 molecular states are defined by quantum numbers of their partners in two-body decays of the
199 $\Upsilon(5S)$ parent: while Z_b is accompanied by a pion, each W_{bJ} is accompanied by a ρ meson (or
200 a photon)). Therefore the W_{bJ} states are expected to appear in transitions $\Upsilon(nS) \rightarrow \rho W_{bJ}$.
201 Conservation of angular momentum allows J in W_{bJ} to be 0, 1 or 2. Excited states such as
202 W'_{b0} could exist as well. Quantum numbers assigned to Z_b and W_{bJ} states are summarized
203 in Table 1.

204 The $\Upsilon(5S)$ resonance does not have enough energy to allow the transition to W_{bJ} with
205 sufficient amount of energy left for the two pions in the tail of the ρ invariant mass. In
206 our analysis, instead of searching for decays with the ρ mesons, we have to allow for the $q\bar{q}$
207 annihilation and pay the price of approximately α_{em} in the branching fraction:

$$\frac{\Gamma(\Upsilon(5S) \rightarrow \gamma W_{bJ})}{\Gamma(\Upsilon(5S) \rightarrow Z_b \pi)} \sim \alpha_{\text{em}} \approx \frac{1}{137} \quad (1)$$

208 Therefore, we search for the transitions $\Upsilon(5S) \rightarrow \gamma W_{bJ}$. This indirect phase space limitation
209 allows us to search only for the $I_3 = 0$ partners of the Z_b states, *i.e.* only the neutral
210 component of each isotriplet can be found in such radiative transitions. We explain this
211 strategy, suggested [13] by M.B. Voloshin, in Fig. 3.

212 To search for all new resonances expected in the new spectroscopy would require to
213 collect a sizeable data sample at $\Upsilon(6S)$ or above its energy. Such possible future studies [14]
214 at Belle II and many more interesting discussions (such as possible existence of isoscalar
215 partners of Z_b and W_{bJ}) can be found elsewhere [10]. In the rest of this paper, we focus on
216 the analysis of the full $\Upsilon(5S)$ data sample where we search for the decay $\Upsilon(5S) \rightarrow \gamma W_{bJ}$.

217 1.4 Expected Signal in Data

218 Belle previously reported [15] that charged Z_b states comprise approximately 2.54% of the
219 1819 $\Upsilon(1S)\pi^+\pi^-$ (followed by $\Upsilon(1S) \rightarrow \mu^+\mu^-$) events observed with the full data sample.

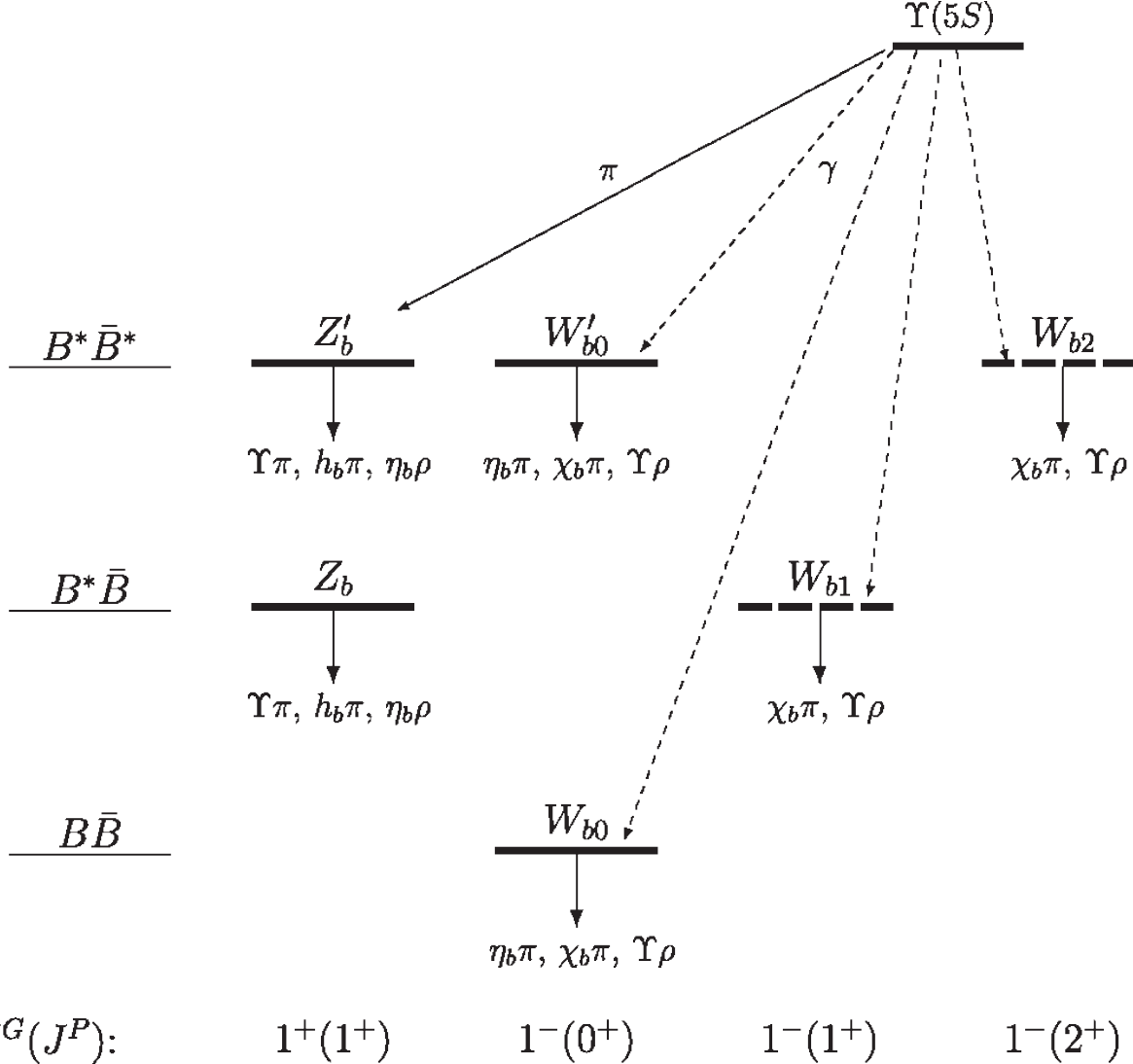


Figure 3: The expected family of isotriplet resonances from Ref. [13] (which the reader is advised to consult for relevant details). For $\Upsilon(6S)$ transitions, the photon is replaced by ρ . This would also allow to access charged W_{bJ} states. Also, please see Table 1.

220 The overall reconstruction efficiency in Z_b analysis was estimated to be around 46%. This
 221 allows us to estimate that, with an ideal, *i.e.* 100% efficient detector, we would expect to
 222 detect, approximately, 100 (charged) Z_b events.

223 While searching for W_{bj} events in radiative decays of $\Upsilon(5S)$, as elaborated in Section 1.3,
 224 we have to pay the price of α_{em} . Jumping a little bit ahead of ourselves, with our overall
 225 detection efficiency of 29%, we therefore expect to observe, on average, 0.2 W_{b0} events. This
 226 number, however, has a (hopefully very) large uncertainty, and, after all, we are (always!)
 227 driven by hope that nature might be kinder to us than we deserve. Also, tangentially, our
 228 LHC colleagues have been searching for signatures of SUSY for some time already, and, no
 229 matter how little has been observed so far, their noble quest will stop not. So why should we
 230 stop ours? On this philosophical note we conclude this discussion and proceed to describe

231 our actual analysis.

232 2 Monte Carlo and Data Samples

233 To study the properties of signal events, we generate 100,000 Monte Carlo (MC) events
 234 for $\Upsilon(5S) \rightarrow \gamma W_{bJ}$ followed by $W_{bJ} \rightarrow \Upsilon(1S)\rho^0$, $\Upsilon(1S) \rightarrow \mu^+\mu^-$, $\rho^0 \rightarrow \pi^+\pi^-$ using MC
 235 generator EvtGen [16]. Detector response is simulated using GEANT4 [17]. W_{bJ} is generated
 236 with an intrinsic width of 15 MeV, similar to the widths of Z_b and Z'_b . Table 2 displays the
 237 decay models [18] used in MC simulation of signal processes. The PHOTOS package [19] is
 238 used to simulated final state radiation (FSR). To allow for softer FSR photons in simulation,
 239 we modified the PHOTOS package to lower the minimum energy of final state radiation.
 240 Please see Section 10.1 for details.

241 We use six streams of generic MC to study background events. Each stream is equivalent
 242 to a full Belle data sample of 121.4 fb^{-1} of $\Upsilon(5S)$ resonance data. We generate additional MC
 243 samples to study background events originating from $\Upsilon(5S) \rightarrow \Upsilon(1S)\pi^+\pi^- \rightarrow \mu^+\mu^-\pi^+\pi^-$
 244 with initial state radiation (ISR) as well as events originating from $\Upsilon(5S) \rightarrow Z_b^\pm\pi^\mp \rightarrow$
 245 $\Upsilon(1S)\pi^\pm\pi^\mp \rightarrow \mu^+\mu^-\pi^\pm\pi^\mp$. We describe our studies of these processes in Section 6 and
 246 Section 7, respectively.

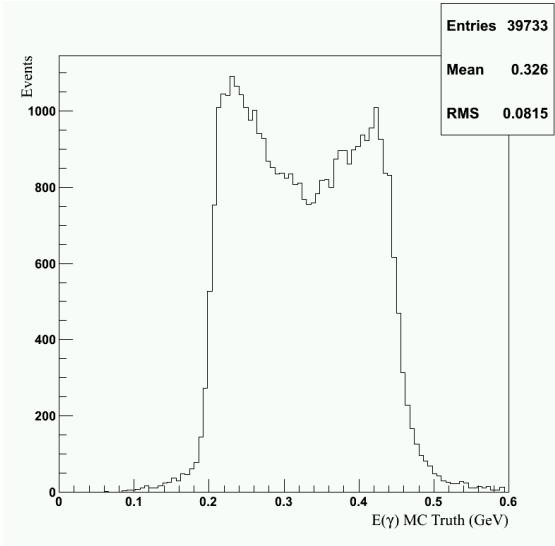
247 In this analysis, we use the full 121.4 fb^{-1} of on-resonance $\Upsilon(5S)$ data collected by the
 248 Belle detector at the KEKB collider from asymmetric energy e^+e^- collisions with $\sqrt{s} = 10.86$
 249 GeV [20].

Decay Process	Decay Model used in Mote Carlo Simulation
$\Upsilon(5S) \rightarrow W_{bJ}\gamma$	VSP_PWAVE
$W_{bJ} \rightarrow \Upsilon(1S)\rho^0$	SVV_HELAMP
$\rho^0 \rightarrow \pi^+\pi^-$	VSS
$\Upsilon(1S) \rightarrow \mu^+\mu^-$	VLL
Final state radiation	PHOTOS (modified)

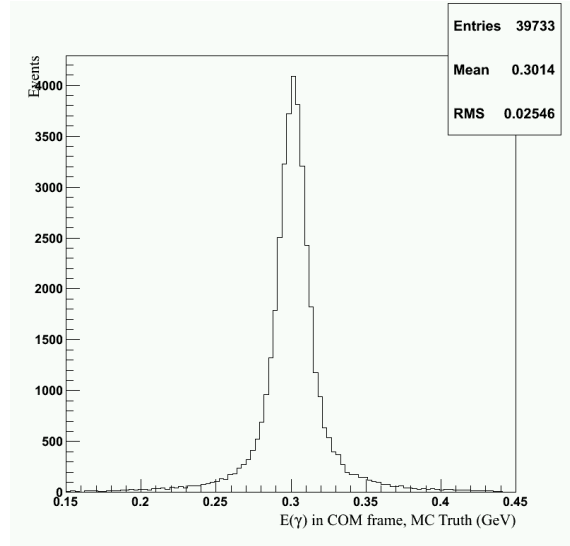
Table 2: EvtGen decay models used in Mote Carlo simulation of signal processes.

250 3 Selection Criteria

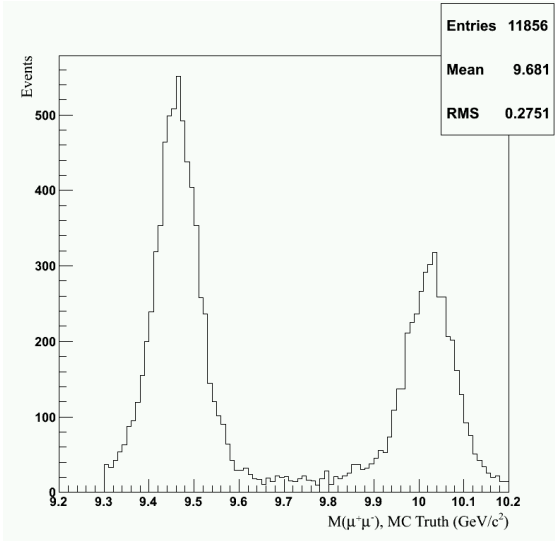
251 We reconstruct the decay mode $\Upsilon(5S) \rightarrow \gamma W_{bJ}$ followed by the decays $W_{bJ} \rightarrow \Upsilon(1S)\rho^0$,
 252 $\Upsilon(1S) \rightarrow \mu^+\mu^-$, $\rho^0 \rightarrow \pi^+\pi^-$. We select a fully-reconstructed final state particle combination
 253 consisting of $\pi^+\pi^-\mu^+\mu^-\gamma$. **The selection criteria that follow, though not systematically**
 254 **optimized, are based on MC truth distributions and typical choices made in previous Belle**
 255 **analyses.**



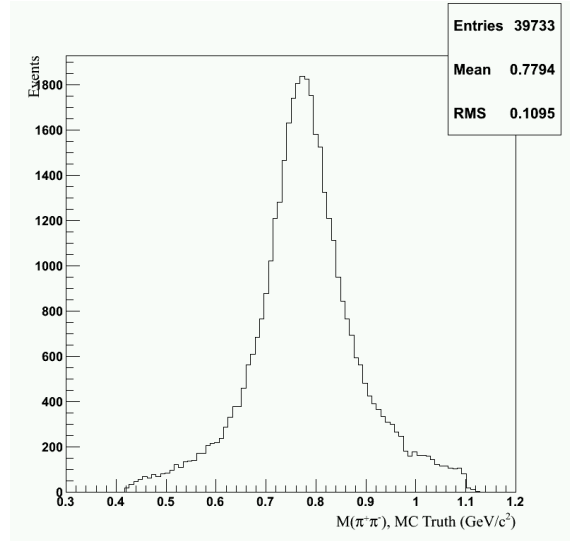
(a) Photon energy in the lab frame for events in signal MC.



(b) Photon energy in the COM frame for events in signal MC.



(c) $M(\mu^+\mu^-)$ for events in generic MC. The left peak is $\Upsilon(1S)$ and the right peak is $\Upsilon(2S)$. Note that the right tail of $\Upsilon(1S)$ overlaps with the left tail of $\Upsilon(2S)$.



(d) $M(\pi^+\pi^-)$ for events in signal MC.

Figure 4: Various MC distributions which informed our selection criteria.

256 3.1 Selection of Photon Candidates

257 We require reconstructed photons have energy between 100 and 600 MeV (in the lab frame)
 258 and polar angle between 17° and 150° . In the center of mass reference frame, the radiative
 259 photon is expected to be monochromatic with energy of approximately 300 MeV. To reject
 260 showers produced by neutral hadrons, we require $E_9/E_{25} > 0.75$, where the E_9/E_{25} ratio is
 261 defined as the energy summed in the 3×3 array of crystals surrounding the center of the

262 shower (E_9) to that of the 5 x 5 array of crystals surrounding the center of the shower (E_{25}).
263 See Fig. 4a and Fig. 4b for relevant distributions.

264 3.2 Selection of Pion and Muon Candidates

265 Pion candidates must satisfy $R_{K,\pi} < 0.9$, where $R_{K,\pi}$ is the “Kaon identification variable”
266 defined as the likelihood ratio of the charged track to be due to a kaon versus a pion, and
267 $R_{e,\text{hadron}} < 0.9$, where $R_{e,\text{hadron}}$ is the likelihood ratio of the charged track to be due to
268 an electron versus a hadron. Similarly, muon candidates must satisfy $R_\mu > 0.1$, where
269 R_μ is the likelihood ratio of the charged track to be due to a muon versus other particles
270 detected by the KLM detector subsystem. After imposing the aforementioned requirements,
271 we additionally require there to be four unique charged tracks – two pions and two muons.
272 Events with more than four such tracks are rejected.

273 To select reconstructed tracks that originate near the interaction point, we require pion
274 and muon candidates have $dr < 0.3$ cm and $|dz| < 2$ cm, where dr and dz are impact
275 parameters in the radial and z directions, respectively. We also require pion and muon
276 candidates to have transverse momenta $p_T > 100$ MeV. Candidate muon pairs must have
277 an invariant mass between $9.3 \text{ GeV}/c^2$ and $9.6 \text{ GeV}/c^2$. Candidate pion pairs must have an
278 invariant mass between $0.42 \text{ GeV}/c^2$ and $1.02 \text{ GeV}/c^2$. See Fig. 4c and Fig. 4d for relevant
279 distributions.

280 3.3 Selection of $\Upsilon(5S)$ Candidates

281 $\Upsilon(5S)$ candidates are required to have an invariant mass between 10.2 GeV and 11.5 GeV.
282 The muon pairs of selected $\Upsilon(5S)$ candidates are mass constrained to the nominal $\Upsilon(1S)$
283 invariant mass of $9.460 \text{ GeV}/c^2$. A summary of our selection criteria is shown in Table 3.

284 3.4 Best Candidate Selection

285 Approximately 32% of signal MC events satisfying our selection criteria have multiple signal
286 candidates. This is exclusively due to relatively soft photons. In events with multiple signal
287 candidates, we select the candidate that has an energy most consistent with the center of
288 mass energy of the experimental run. The selected candidates are correctly MC-tagged to full
289 MC truth for signal 90% of the time. For fully reconstructed signal MC events with multiple
290 candidates, our best candidate selection method selects a candidate correctly MC-tagged to
291 full MC truth 88% of the time.

292 4 Signal Monte Carlo Studies

293 4.1 Signal Monte Carlo Distributions

294 To understand properties of signal events, we investigate two invariant mass variables,
295 $M(\pi^+\pi^-(\mu^+\mu^-)_{\text{fit}})$ and $M_{\text{rec}}(\gamma)$, where subscript “fit” indicates that the muon pair is con-
296 strained to the nominal mass of $\Upsilon(1S)$. We define the invariant mass recoiling against X
297 as

Particle Candidate	Selection Criteria
γ	$100 < \text{MeV } E(\gamma) < 600 \text{ MeV}$
π^\pm, μ^\pm	$dr < 0.3 \text{ cm}$ $ dz < 2 \text{ cm}$ $p_T > 100 \text{ MeV}/c$
π^\pm PID	$R_{K,\pi} < 0.9$ $R_{e,hadron} < 0.9$
μ^\pm	$R_\mu > 0.10$
ρ^0	$0.420 \text{ GeV}/c^2 < M_{\pi^+\pi^-} < 1.020 \text{ GeV}/c^2$
$\Upsilon(1S)$	$9.3 \text{ GeV}/c^2 < M_{\mu^+\mu^-} < 9.6 \text{ GeV}/c^2$
$\Upsilon(5S)$	$10.2 \text{ GeV}/c^2 < M_{\pi^+\pi^-\mu^+\mu^-} < 11.5 \text{ GeV}/c^2$ $-0.05 \text{ GeV} < \Delta E < 0.03 \text{ GeV}$
(full event reconstruction)	Exactly four tracks: two muons and two pions

Table 3: Selection criteria for $\Upsilon(5S) \rightarrow \gamma W_{bJ}$

$$M_{\text{rec}}(X) = \sqrt{(E_{\text{cm}}(\text{exp}) - E_{\text{cm}}(X))^2 - |\vec{0} - \vec{p}_{\text{cm}}(X)|^2} \quad (2)$$

where $E_{\text{cm}}(\text{exp})$ is the run's average energy, and $E_{\text{cm}}(X)$ and $\vec{p}_{\text{cm}}(X)$ are the energy and momentum of system X . Subscript "cm" is used for quantities evaluated in the center of mass reference frame of the experiment. For signal events, $M_{\text{rec}}(\gamma)$ and $M(\pi^+\pi^-(\mu^+\mu^-)_{\text{fit}})$ are two independent ways to estimate the invariant mass of W_{bJ} . Fully reconstructed signal events fall along the main diagonal of the $M(\pi^+\pi^-(\mu^+\mu^-)_{\text{fit}})$ vs $M_{\text{rec}}(\gamma)$ plot shown in Fig. 5. We define energy balance ΔE as

$$\Delta E = E_{\text{cm}}(\pi^+\pi^-(\mu^+\mu^-)_{\text{fit}}\gamma) - E_{\text{cm}}(\text{exp}). \quad (3)$$

ΔE is the most important variable we can use to select fully reconstructed signal event candidates.

There are two effects contributing to the observed width of $M(\pi^+\pi^-(\mu^+\mu^-)_{\text{fit}})$: (1) the intrinsic width of W_{bJ} , and (2) the charged track reconstruction. Fig. 6 shows $M(\pi^+\pi^+\mu^+\mu^-)$ and $M(\pi^+\pi^-(\mu^+\mu^-)_{\text{fit}})$ resolutions for signal events within the signal region and sideband regions (defined in Section 4.2). We model both resolutions as the sum of two Gaussians with the same mean and fit both resolutions. Contribution to $M(\pi^+\pi^-(\mu^+\mu^-)_{\text{fit}})$ resolution from charged track reconstruction is primarily due to pions, since muon pairs are constrained to $\Upsilon(1S)$ invariant mass.

The distribution of $M_{\text{rec}}(\gamma)$ has a long tail due to an underestimation of photon energy, causing an overestimation of $M_{\text{rec}}(\gamma)$. Effects contributing to the observed width of $M_{\text{rec}}(\gamma)$ include (1) intrinsic width of W_{bJ} , and (2) photon energy resolution. $M_{\text{rec}}(\gamma)$ resolution is dominated by photon energy resolution.

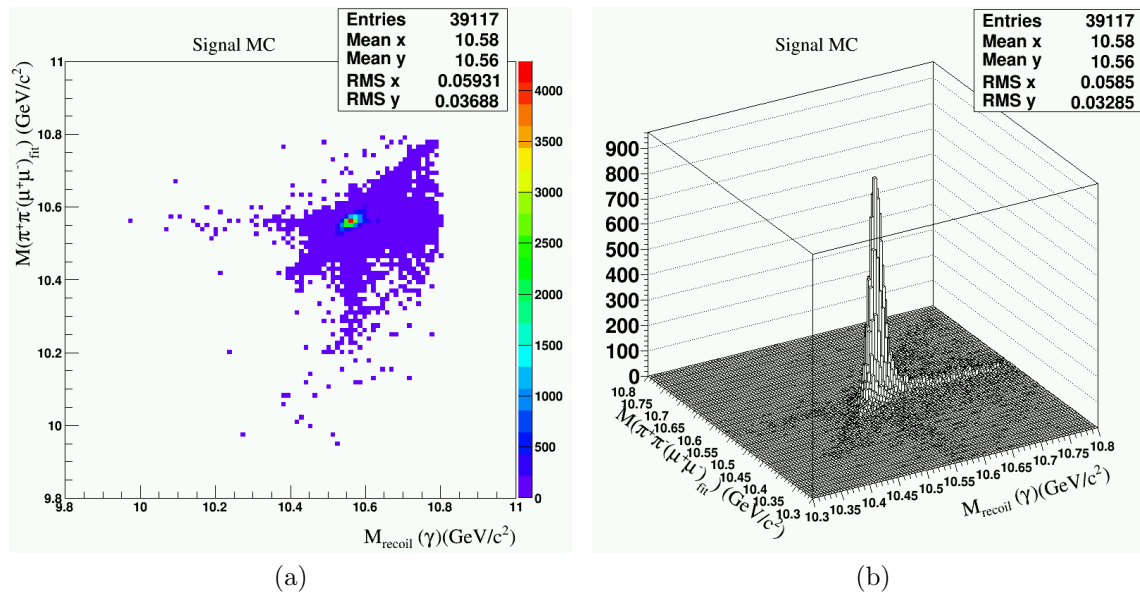
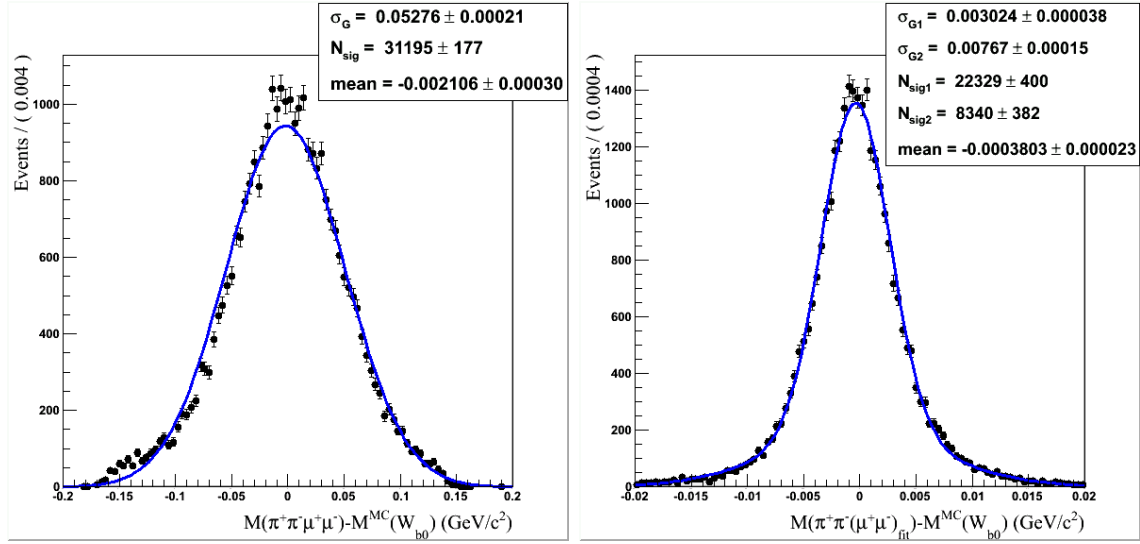


Figure 5: $M(\pi^+\pi^-(\mu^+\mu^-)_{\text{fit}})$ vs $M_{\text{rec}}(\gamma)$ distribution for W_{B0} signal MC events. We show the lego plot in Fig. 5b to emphasize that the tail of $M_{\text{rec}}(\gamma)$ is not as large as it appears in Fig. 5a. Note that Fig. 5b is plotted in a smaller range.

Quantity	Value
Intrinsic width of W_{bJ}	15 MeV/ c^2
Charged track resolution	4 MeV
Photon energy resolution	8 MeV
Beam energy resolution	6 MeV

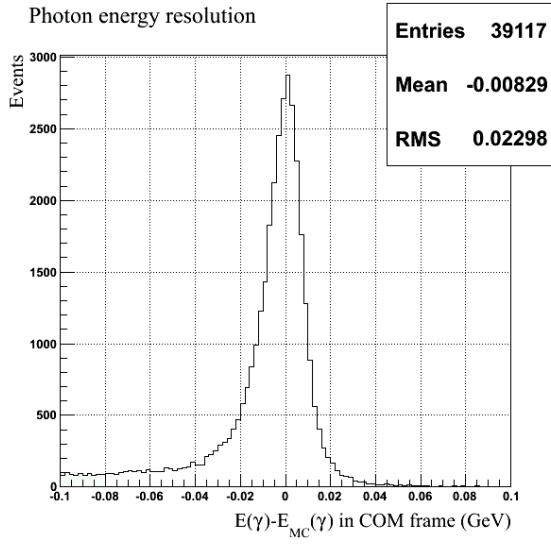
Table 4: Quantities contributing to widths of measured quantities

317 Effects contributing to the observed shape of ΔE include (1) photon energy resolution, (2)
 318 charged track resolution, (3) beam energy resolution, and (4) the intrinsic width of W_{bJ} . ΔE
 319 resolution is dominated by photon energy resolution as well. The values of relevant widths
 320 are listed in Table 4. In signal MC we observe $\sigma_{\Delta E} \approx 12$ MeV, so we take advantage of this
 321 excellent energy resolution to select fully reconstructed events. Because the distribution of
 322 ΔE is asymmetric (primarily due to leakage from the calorimeter and relatively soft non-
 323 signal photons in signal events), we use an asymmetric selection and require $-0.05 \text{ GeV} \leq$
 324 $\Delta E \leq 0.03 \text{ GeV}$. This selection cuts out the long tail in the distribution of $M_{\text{rec}}(\gamma)$ and
 325 reduces the efficiency by 20%. Note, however, that this selection primarily removes events
 326 where the signal photon is not reconstructed. After applying this selection on ΔE , signal
 327 reconstruction efficiency becomes approximately 31%. Fig. 7 displays ΔE resolution as well
 328 as quantities contributing to ΔE resolution.

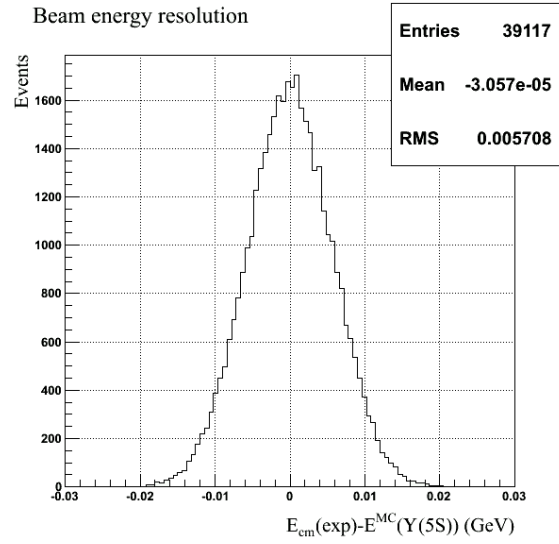


(a) $M(\pi^+\pi^+\mu^+\mu^-)$ resolution. Note that muons are not mass constrained. (b) $M(\pi^+\pi^-(\mu^+\mu^-)_{\text{fit}})$ resolution (muons are mass constrained).

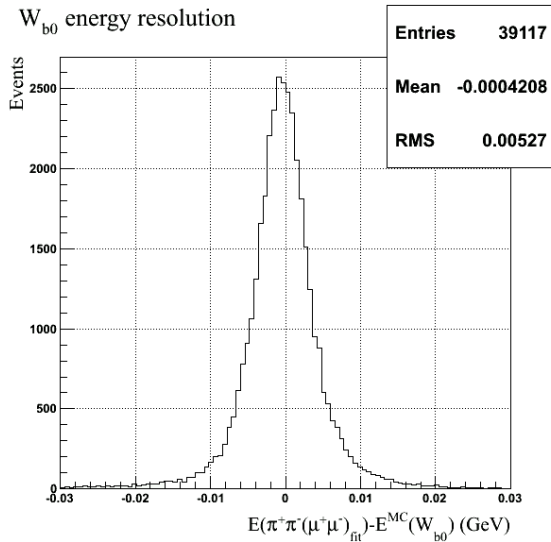
Figure 6: $M(\pi^+\pi^+\mu^+\mu^-)$ and $M(\pi^+\pi^-(\mu^+\mu^-)_{\text{fit}})$ resolutions for signal events within the signal region and sideband regions (defined in Section 4.2). Note that the horizontal scales are different.



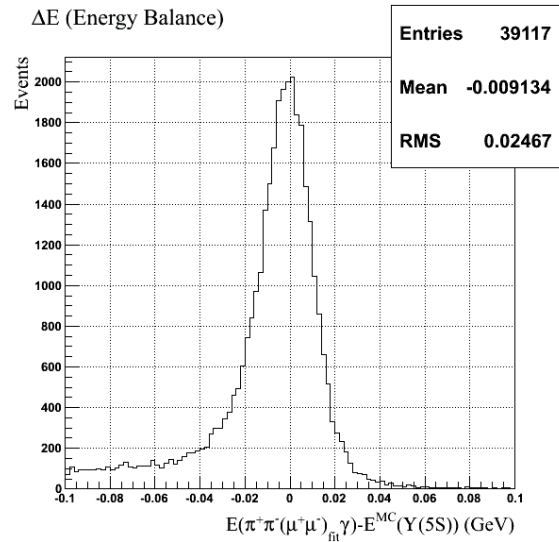
(a) Signal photon energy line shape in the COM reference frame.



(b) Beam energy resolution.



(c) $M(\pi^+\pi^-(\mu^+\mu^-)_{\text{fit}})$ energy line shape (includes the effect of intrinsic W_{bJ} width and charged track reconstruction).



(d) Signal candidate energy line shape. Includes the effects of W_{bJ} intrinsic width and resolution.

Figure 7: ΔE resolution and quantities contributing to ΔE resolution.

329 4.2 Description of the Signal Region

330 Table 5 contains the definitions of four important regions in this analysis. Before investigating
 331 data, we blind the region where we expect to find signal. We refer to this region as the
 332 blinded region. The invariant masses of W_{b0} , W_{b1} , and W'_{b0} and W_{b2} are expected to be at
 333 the $B\bar{B}$, $B^*\bar{B}$, and $B^*\bar{B}^*$ thresholds, respectively. The blinded region is defined as the region
 334 between the $B\bar{B}$ and $B^*\bar{B}^*$ thresholds plus an additional margin of 70 MeV on either side.
 335 This corresponds to $10.49 \text{ GeV}/c^2 \leq M(\pi^+\pi^-(\mu^+\mu^-)_{\text{fit}}) \leq 10.72 \text{ GeV}/c^2$. The boundary on

Region Name	Boundary Definitions
Blinded Region	$10.49 \text{ GeV}/c^2 \leq M(\pi^+\pi^-(\mu^+\mu^-)_{\text{fit}}) \leq 10.72 \text{ GeV}/c^2$ $M_{\text{rec}}(\gamma) \geq M(\pi^+\pi^-(\mu^+\mu^-)_{\text{fit}}) - 0.04 \text{ GeV}/c^2$ $M_{\text{rec}}(\gamma) \leq 10.8 \text{ GeV}/c^2$
Signal Region	$10.49 \text{ GeV}/c^2 \leq M(\pi^+\pi^-(\mu^+\mu^-)_{\text{fit}}) \leq 10.72 \text{ GeV}/c^2$ $-0.05 \text{ GeV} \leq \Delta E \leq 0.03 \text{ GeV}$
Sideband Region	$10.38 \text{ GeV}/c^2 \leq M(\pi^+\pi^-(\mu^+\mu^-)_{\text{fit}}) \leq 10.49 \text{ GeV}/c^2$ $10.72 \text{ GeV}/c^2 \leq M(\pi^+\pi^-(\mu^+\mu^-)_{\text{fit}}) \leq 10.80 \text{ GeV}/c^2$ $-0.05 \text{ GeV} \leq \Delta E \leq 0.03 \text{ GeV}$.
Grand Sideband Region	$10.38 \text{ GeV}/c^2 \leq M(\pi^+\pi^-(\mu^+\mu^-)_{\text{fit}}) \leq 10.80 \text{ GeV}/c^2$ $-0.20 \text{ GeV} \leq \Delta E \leq 0.20 \text{ GeV}$

Table 5: Definitions of the signal region and other important regions.

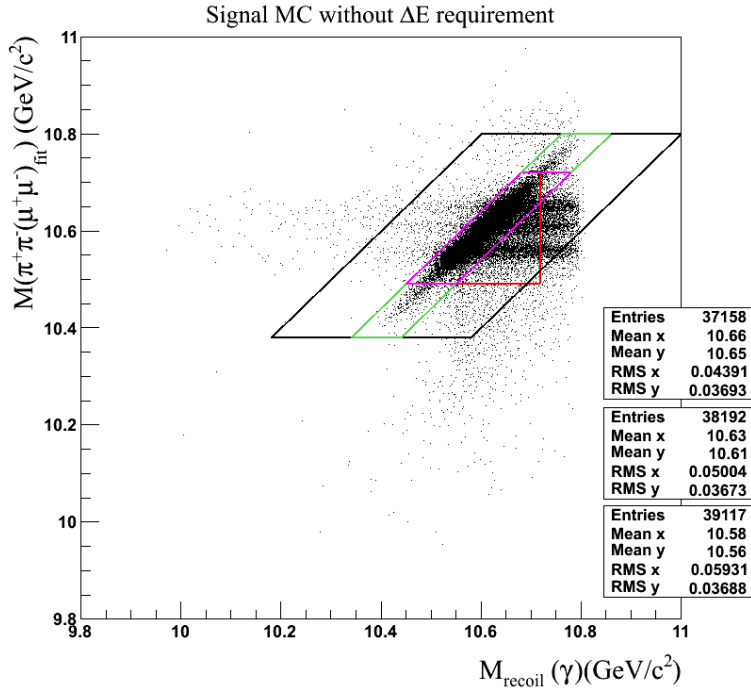
336 the left side of the region is defined by the sloped line $M_{\text{rec}}(\gamma) \geq M(\pi^+\pi^-(\mu^+\mu^-)_{\text{fit}}) - 0.04$
337 GeV/c^2 which lies parallel to the main diagonal. Approximately 20% of signal events are
338 located in the long right tail of the distribution of $M_{\text{rec}}(\gamma)$. A phase space boundary on
339 the right side of the plot at $M_{\text{rec}}(\gamma) \approx 10.75 \text{ GeV}/c^2$ forces this long tail of the $M_{\text{rec}}(\gamma)$
340 distribution into a smaller region for the higher mass W_{bJ} states. Hence, we do not define
341 a sloped boundary line as the right side of the signal region – a diagonal boundary would
342 exclude more signal events for the lower mass states because of the aforementioned phase
343 space boundary compressing the tail. Instead, we define the vertical line boundary $M_{\text{rec}}(\gamma) \leq$
344 $10.72 \text{ GeV}/c^2$ which assures that approximately equal percentages of signal would be blinded
345 for all masses of W_{bJ} states.

346 We define the signal region as the region contained within $10.49 \text{ GeV}/c^2 \leq M(\pi^+\pi^-(\mu^+\mu^-)_{\text{fit}}) \leq$
347 $10.72 \text{ GeV}/c^2$ satisfying $-0.05 \text{ (GeV)} \leq \Delta E \leq 0.03 \text{ GeV}$. The ΔE requirement selects only
348 fully-reconstructed signal events, where signal is peaking.

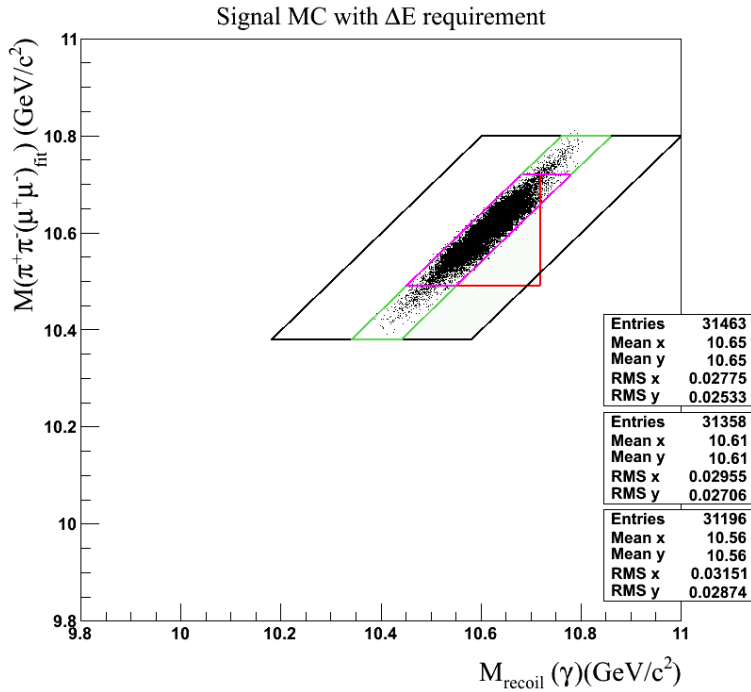
349 The sideband region is essentially an extension of the signal region, defined as the
350 regions within $10.38 \text{ GeV}/c^2 \leq M(\pi^+\pi^-(\mu^+\mu^-)_{\text{fit}}) \leq 10.49 \text{ GeV}/c^2$ and $10.72 \text{ GeV}/c^2 \leq$
351 $M(\pi^+\pi^-(\mu^+\mu^-)_{\text{fit}}) \leq 10.80 \text{ GeV}/c^2$ satisfying $-0.05 \text{ (GeV)} \leq \Delta E \leq 0.03 \text{ GeV}$.

352 We additionally define the grand sideband region as the region within $10.38 \text{ GeV}/c^2 \leq$
353 $M(\pi^+\pi^-(\mu^+\mu^-)_{\text{fit}}) \leq 10.80 \text{ GeV}/c^2$ satisfying $-0.20 \text{ GeV} \leq \Delta E \leq 0.20 \text{ GeV}$. This region is
354 used when studying background in data.

355 Fig. 8 displays these four regions with our three signal MC samples. It is important to
356 note that the blinded region is not completely contained within the grand sideband region
357 and the signal region is not completely contained within the blinded region. This is due to
358 historical reasons, as the blinded region was defined prior to the use of ΔE in this analysis.



(a) Does not include ΔE requirement.



(b) Includes ΔE requirement.

Figure 8: The blinded region (red), signal region (magenta), sideband region (green), and the grand sideband region (black). The plot in 8a includes the aforementioned ΔE requirement, while the plot in 8b does not. From top to bottom, the statistics boxes correspond to W'_{b0} , W_{b1} , and W_{b0} signal MC, respectively.

359 4.3 Trigger Simulation

360 Relatively low final state particle multiplicity of our signal events requires us to investigate
361 trigger efficiency. Trigger efficiency is simulated after full reconstruction. We find correlations
362 between trigger efficiency and kinematics. Fig. 9 shows various 2-dimensional distributions
363 of $\mu^+ \cos(\theta)$ vs $\mu^- \cos(\theta)$, and we see that events failing to satisfy trigger are more likely
364 to have one of the muons at a small angle with respect to the beam axis ($|\cos(\theta)| \geq 0.8$).
365 Fig. 10 shows additional distributions of $\mu^+ \cos(\theta)$ vs $\mu^+ \cos(\theta)$ which we use to determine
366 trigger efficiencies. When neither muon is at a small angle with respect to the beam axis,
367 trigger efficiency is 96%. When one of the muons is at a small angle with respect to the beam
368 axis, trigger efficiency drops to 89%. For all generated signal MC events, trigger efficiency is
369 approximately 94%. After accounting for trigger efficiency, our overall efficiency drops from
370 31% to 29%.

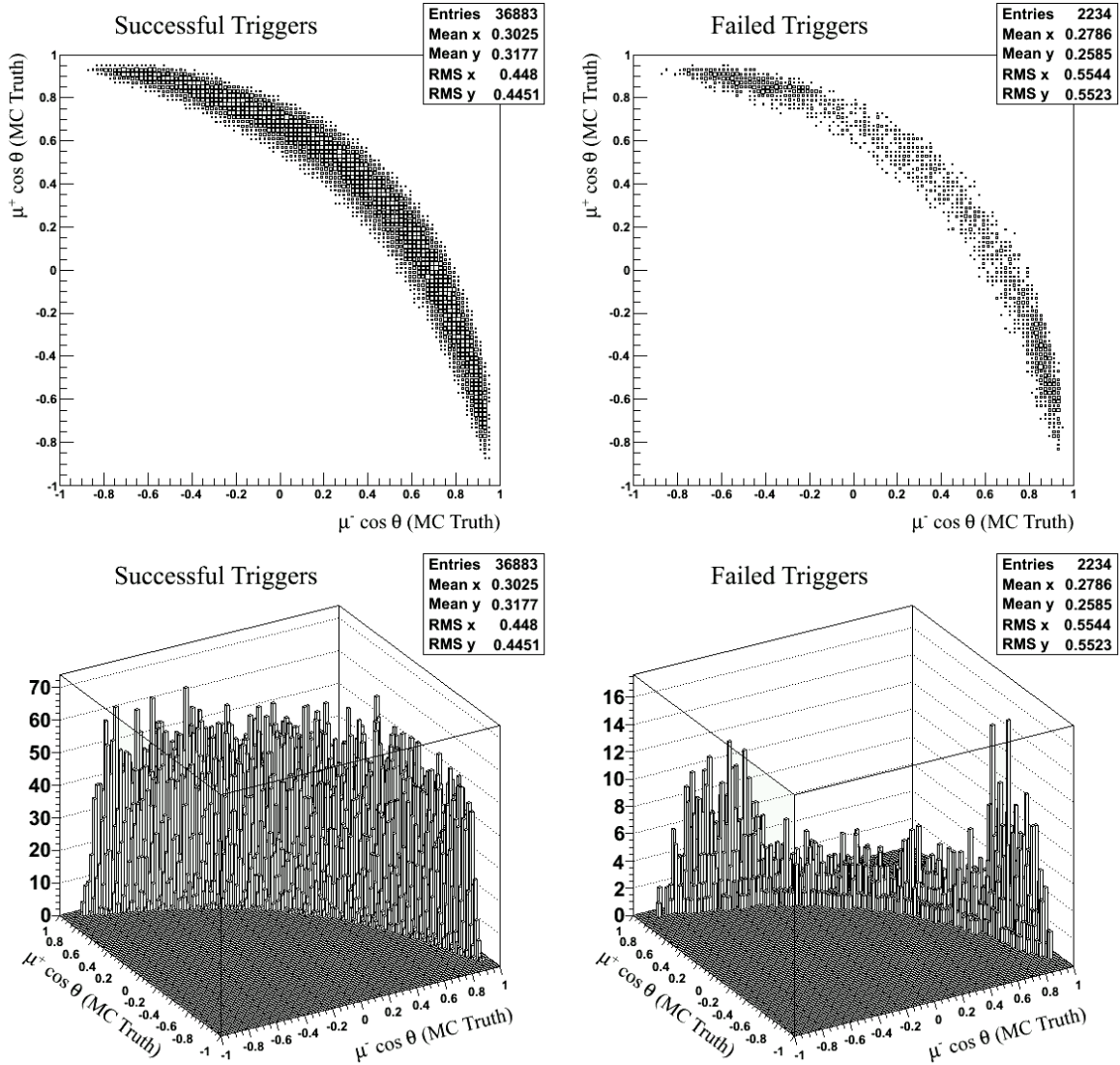


Figure 9: Reconstructed signal MC events that satisfy the offline trigger selection are plotted on the left, while events that fail the offline trigger selection are plotted on the right. We observe that events satisfying the trigger criteria are distributed more or less uniformly for kinematically allowed muons, but events failing to satisfy trigger are more likely to have one of the muons at a small angle with respect to the beam axis.

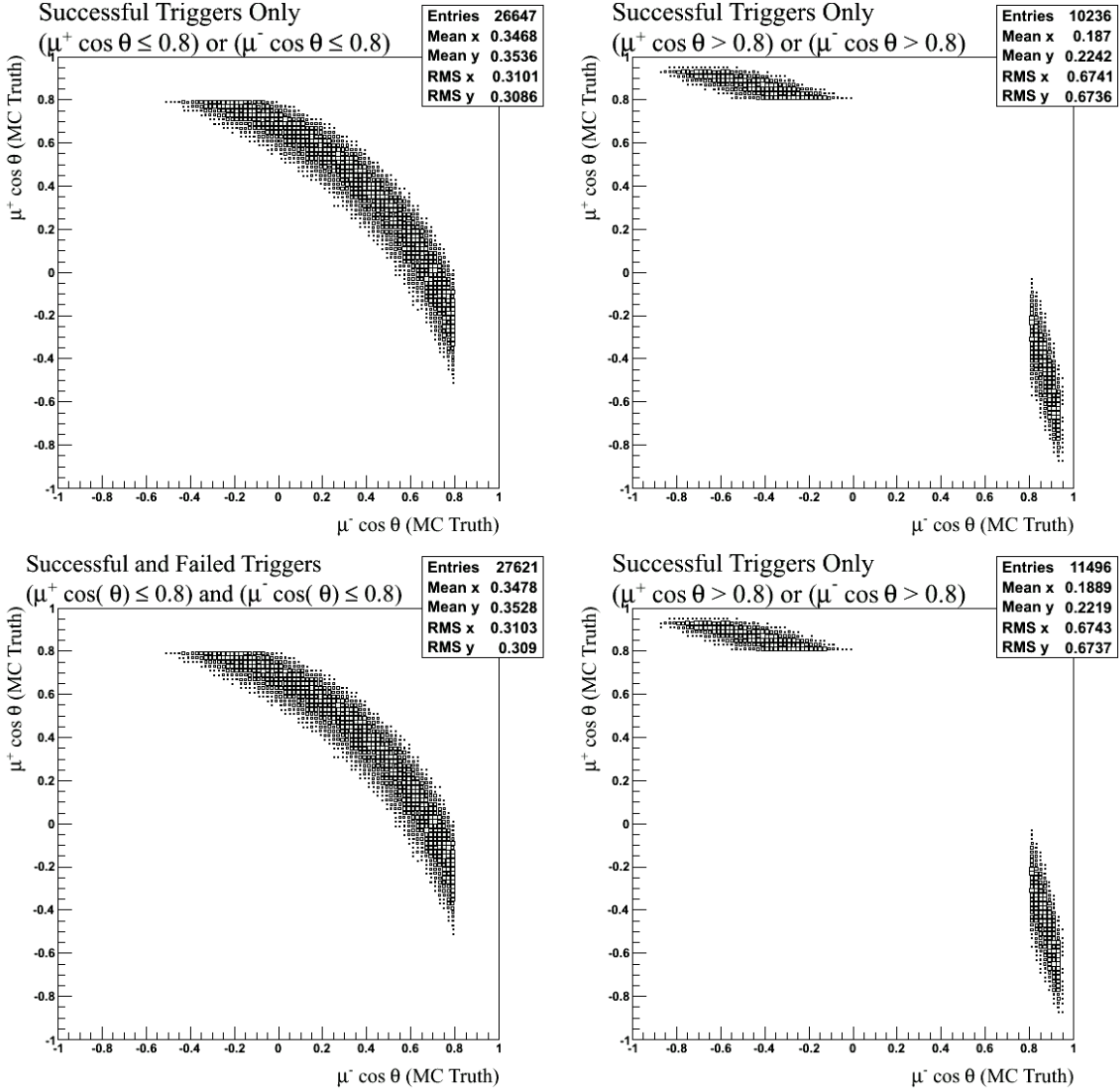


Figure 10: All reconstructed events in which both muons are generated with $|\cos(\theta)| < 0.8$ are plotted in the left two figures. Trigger efficiency for such events is approximately $(96 \pm 4)\%$. In the right two figures, we plot all reconstructed events where one of the muons is generated with $|\cos(\theta)| > 0.8$. Trigger efficiency for these events is reduced to about $(89 \pm 4)\%$.

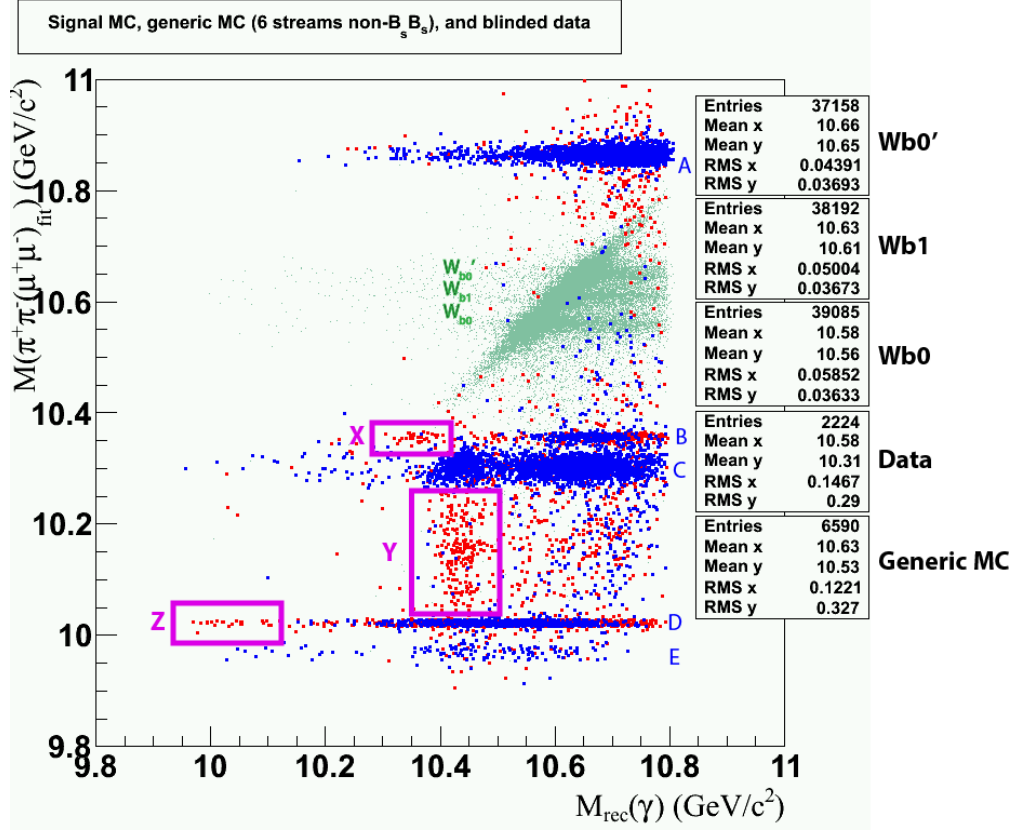


Figure 11: W_{b0} , W_{b1} , and W'_{b0} signal MC (light green), six streams of non- $B_s B_s$ generic MC (blue), and data with the signal region blinded (red).

371 5 Background Studies

372 5.1 Generic Monte Carlo and Blinded Data

373 Fig. 11 shows the distribution of $M(\pi^+\pi^-(\mu^+\mu^-)_{\text{fit}})$ vs $M_{\text{rec}}(\gamma)$ for generic MC and blinded
 374 data events. Using MC truth, we identify the background decays in generic MC and blinded
 375 data and group them into eight categories which are defined in Table 6. No uds , charm,
 376 or $B_s B_s$ generic MC events pass our selection criteria. A large number of non- $B_s B_s$ events
 377 do satisfy our selection criteria, though they fall primarily outside the signal region. The
 378 ΔE requirement excludes most of these background events. The most prominent non- $B_s B_s$
 379 background sources are (cascade) dipion transitions to $\Upsilon(1S)$. We observe an enhancement
 380 in generic MC within the blinded region due to the decay $\Upsilon(5S) \rightarrow \Upsilon(2S)\pi^+\pi^-$, $\Upsilon(2S) \rightarrow$
 381 $\Upsilon(1S)\pi^+\pi^-$ where the selected signal pion candidates did not come from the same parent.
 382 The enhancement is removed when the ΔE constraint is applied, as such background events
 383 are not fully reconstructed.

384 We observe several regions where data events are clustering but generic MC events are
 385 not, and we have identified the likely origins of these events. The regions labeled X and Z
 386 in Fig. 11 are populated by events which are due to radiative returns to a lower mass $\Upsilon(nS)$
 387 where the radiative photon is selected as our signal photon candidate. These events are

Label	Background
A	$\Upsilon(5S) \rightarrow \Upsilon(1S)\pi^+\pi^- \rightarrow \mu^+\mu^-\pi^+\pi^-$
B	$\Upsilon(5S) \rightarrow \Upsilon(3S)\pi^+\pi^- \rightarrow \Upsilon(1S)\pi^+\pi^-\pi^+\pi^- \rightarrow \mu^+\mu^-\pi^+\pi^-\pi^+\pi^-$ $\Upsilon(5S) \rightarrow \Upsilon(3S)\pi^0\pi^0 \rightarrow \Upsilon(1S)\pi^+\pi^-\pi^0\pi^0 \rightarrow \mu^+\mu^-\pi^+\pi^-\pi^0\pi^0$
C	$\Upsilon(5S) \rightarrow \Upsilon(2S)\pi^+\pi^- \rightarrow \Upsilon(1S)\pi^+\pi^-\pi^+\pi^- \rightarrow \mu^+\mu^-\pi^+\pi^-\pi^+\pi^-$ $\Upsilon(5S) \rightarrow \Upsilon(2S)\pi^+\pi^- \rightarrow \Upsilon(1S)\pi^0\pi^0\pi^+\pi^- \rightarrow \mu^+\mu^-\pi^0\pi^0\pi^+\pi^-$
D	$\Upsilon(5S) \rightarrow \Upsilon(2S)\pi^0\pi^0 \rightarrow \Upsilon(1S)\pi^+\pi^-\pi^0\pi^0 \rightarrow \mu^+\mu^-\pi^+\pi^-\pi^0\pi^0$
E	$\Upsilon(5S) \rightarrow \Upsilon(3S)\pi^+\pi^- \rightarrow \Upsilon(1S)\pi^0\pi^0\pi^+\pi^- \rightarrow \mu^+\mu^-\pi^0\pi^0\pi^+\pi^-$
X	$e^+e^- \rightarrow \Upsilon(3S)\gamma \rightarrow \Upsilon(1S)\pi^+\pi^-\gamma \rightarrow \mu^+\mu^-\pi^+\pi^-\gamma$
Y	Various processes involving $\chi_{bJ}(1P) \rightarrow \gamma\Upsilon(1S)$, <i>e.g.</i> $\Upsilon(5S) \rightarrow \Upsilon(1D)\pi^+\pi^-$, where $\Upsilon(1D) \rightarrow \gamma\chi_{bJ}(1P)$
Z	$e^+e^- \rightarrow \Upsilon(2S)\gamma \rightarrow \Upsilon(1S)\pi^+\pi^-\gamma \rightarrow \mu^+\mu^-\pi^+\pi^-\gamma$

Table 6: Backgrounds labeled in Fig. 11.

388 fully reconstructed, and thus fall along the main diagonal of the plot. The region labeled
389 Y includes processes involving radiative decays of $\chi_{bJ}(1P)$. These events have additional
390 final state particles that are not reconstructed, and hence they fall below the main diagonal
391 where $\Delta E < 0$. Events in categories X, Y, and Z are not of concern to us, since they are
392 located far from the signal region.

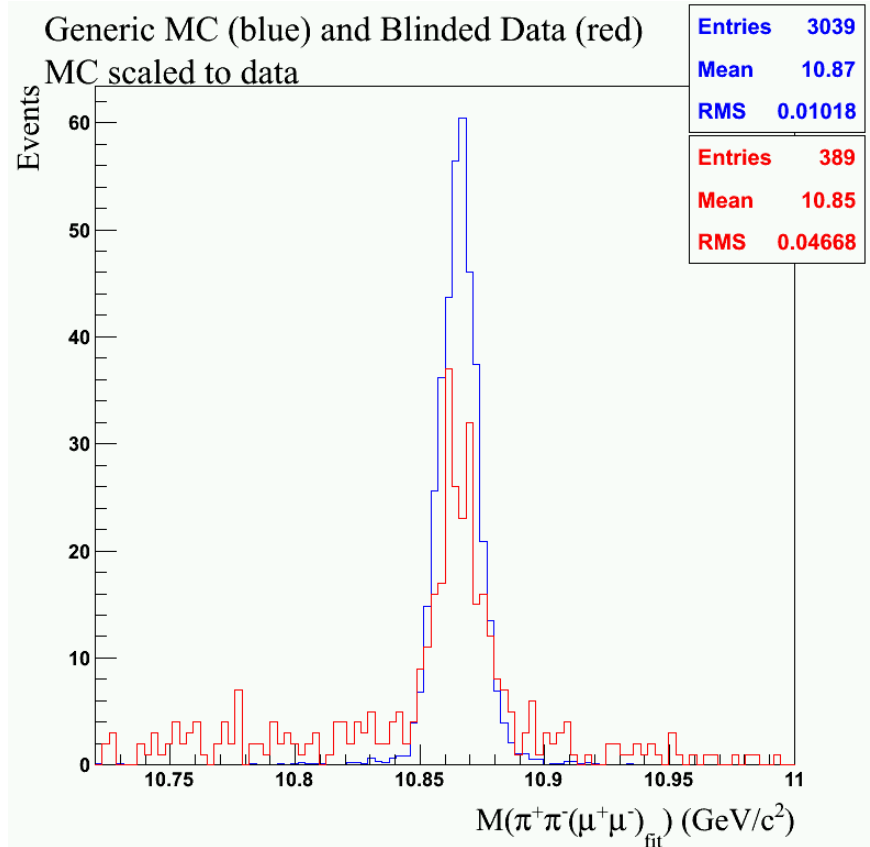


Figure 12: $M(\pi^+\pi^-(\mu^+\mu^-)_{\text{fit}})$ distributions for $\Upsilon(5S) \rightarrow \Upsilon(1S)\pi^+\pi^-$ events (label 'A' in Table 6). Distributions for generic MC and blinded data are shown in blue and red, respectively. Generic MC does not include ISR and is normalized to the number of data events shown in the plotted range. We choose $10.72 \text{ GeV}/c^2$ as the lower limit of the range plotted, since lower masses would include the blinded region.

393 6 Background from $\Upsilon(5S) \rightarrow \Upsilon(1S)\pi^+\pi^-$ with Initial 394 State Radiation (ISR)

395 We find that dipion transitions to $\Upsilon(1S)$ (labeled 'A' in Fig. 11) have a much longer tail
396 in data than in generic MC. This difference is shown in Fig. 12, and is due to initial state
397 radiation (ISR). This tail contaminates the signal region, so we generate additional MC
398 samples with ISR to study these backgrounds.

399 6.1 $\Upsilon(5S) \rightarrow \Upsilon(1S)\pi^+\pi^-$ ISR Monte Carlo Sample

400 The VectorISR model [18] is used to simulate ISR. We reweight the ISR photon energy
401 spectrum according to the correct radiator function up to order α^2 [21] using a Monte Carlo
402 method. After reweighting, there are approximately 110,000 events in our MC sample. A
403 distribution of the reweighted ISR spectrum is shown in Fig. 13.

404 Fig. 14 shows the $M(\pi^+\pi^-(\mu^+\mu^-)_{\text{fit}})$ vs $M_{\text{rec}}(\gamma)$ distribution for reweighted $\Upsilon(5S) \rightarrow$

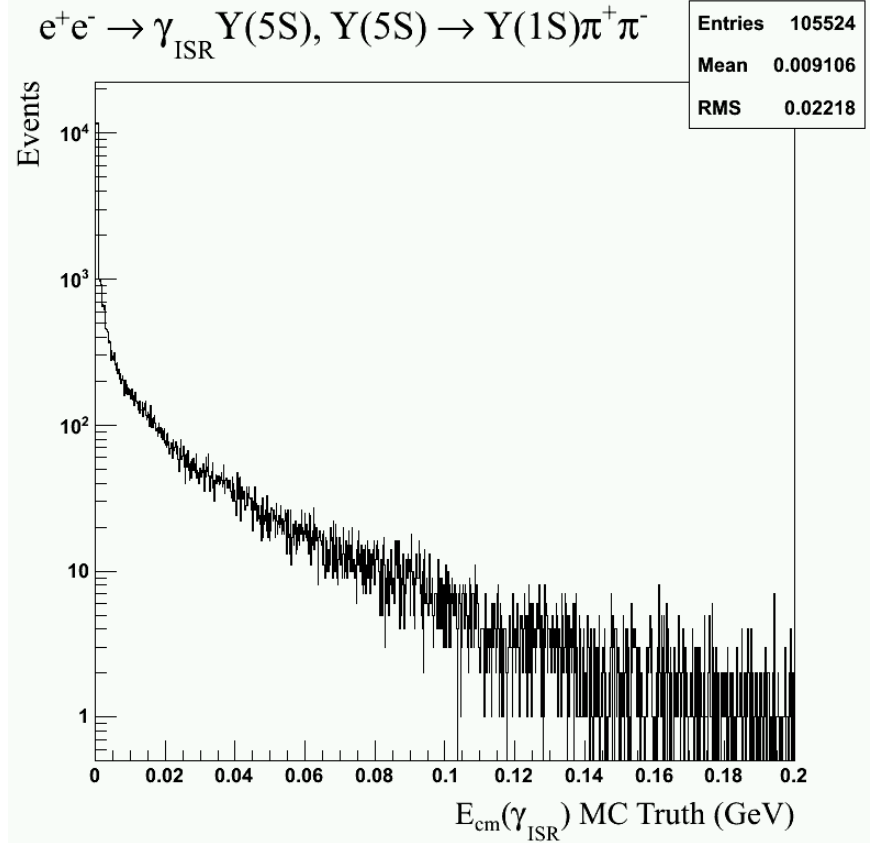


Figure 13: Reweighted ISR energy spectrum for $e^+e^- \rightarrow \gamma_{\text{ISR}} \Upsilon(5S), \Upsilon(5S) \rightarrow \Upsilon(1S)\pi^+\pi^-$. Note that a log scale is used for the vertical axis.

405 $\Upsilon(1S)\pi^+\pi^-$ events with ISR. Recall that the two plotted variables represent two independent
 406 ways to estimate the invariant mass of W_{bJ} , and therefore fully reconstructed events fall along
 407 the main diagonal of this plot. When the ISR photon of these backgrounds is selected as
 408 the signal photon candidate, these backgrounds are also fully reconstructed and fall along
 409 the main diagonal within the signal region. Approximately 3% of reconstructed events fall
 410 in the signal region. Fortunately, these backgrounds do not peak in the signal region in the
 411 distribution of $M(\pi^+\pi^-(\mu^+\mu^-)_{\text{fit}})$.

412 We simulate $\Upsilon(5S) \rightarrow \Upsilon(1S)\pi^+\pi^-$ with ISR using the models listed in Table 7. To
 413 determine if the choice of decay models affects the distribution shape of our signal variable
 414 $M(\pi^+\pi^-(\mu^+\mu^-)_{\text{fit}})$, we generate additional samples using the VVPIPI decay [18] model for
 415 $\Upsilon(5S) \rightarrow \Upsilon(1S)\pi^+\pi^-$ and the VLL decay model [18] for $\Upsilon(1S) \rightarrow \mu^+\mu^-$. Fig. 15 shows the
 416 distribution of $M(\pi^+\pi^-(\mu^+\mu^-)_{\text{fit}})$ for two different MC samples generated using different
 417 decay models.

418 We find that the choice of decay model has only a small effect on the shape of the
 419 $M(\pi^+\pi^-(\mu^+\mu^-)_{\text{fit}})$ distribution. Furthermore, we plot the $\cos\theta$ of μ^+ in Fig. 16 and find
 420 that the presence of ISR has only a small effect on the the angular distributions of muons. To
 421 determine if ISR affects the width of the $M(\pi^+\pi^-(\mu^+\mu^-)_{\text{fit}})$ distribution for signal processes
 422 $\Upsilon(5S) \rightarrow \gamma W_{bJ}$, we generate additional MC samples for the the signal process $\Upsilon(5S) \rightarrow \gamma W_{bJ}$

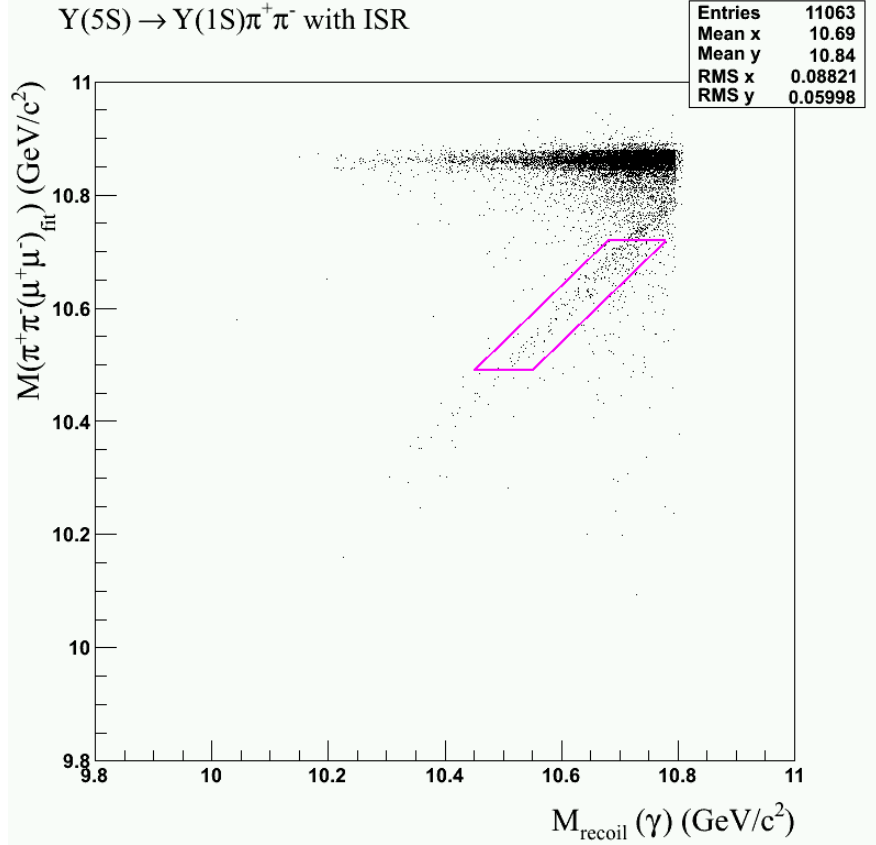


Figure 14: A 2-dimensional $M(\pi^+\pi^-(\mu^+\mu^-)_{\text{fit}})$ vs $M_{\text{rec}}(\gamma)$ distribution for $\Upsilon(5S) \rightarrow \Upsilon(1S)\pi^+\pi^-$ events with ISR (after reweighting). The signal region is outlined in magenta.

Decay Process	Decay Model used in Mote Carlo Simulation
$\Upsilon(5S) \rightarrow \Upsilon(1S)\pi^+\pi^-$	PHSP
$\Upsilon(1S) \rightarrow \mu^+\mu^-$	PHSP
Initial state radiation	VectorISR
Final state radiation	PHOTOS

Table 7: Decay models used in Mote Carlo simulation of $\Upsilon(5S) \rightarrow \Upsilon(1S)\pi^+\pi^-$ with ISR.

423 with ISR. We find that ISR has practically no effect on the width of the distribution of
 424 $M(\pi^+\pi^-(\mu^+\mu^-)_{\text{fit}})$.

425 6.2 Background Shape of $\Upsilon(5S) \rightarrow \Upsilon(1S)\pi^+\pi^-$ with ISR

426 It is likely that events due to $\Upsilon(5S) \rightarrow \Upsilon(1S)\pi^+\pi^-$ with ISR are a dominant source of
 427 backgrounds in the signal region. The rightmost plot in Fig. 17 shows the distribution of
 428 these events within the signal region for our reweighted MC. To see how the selection on
 429 ΔE affects the background shape, we loosen up the selection on ΔE in the left and middle

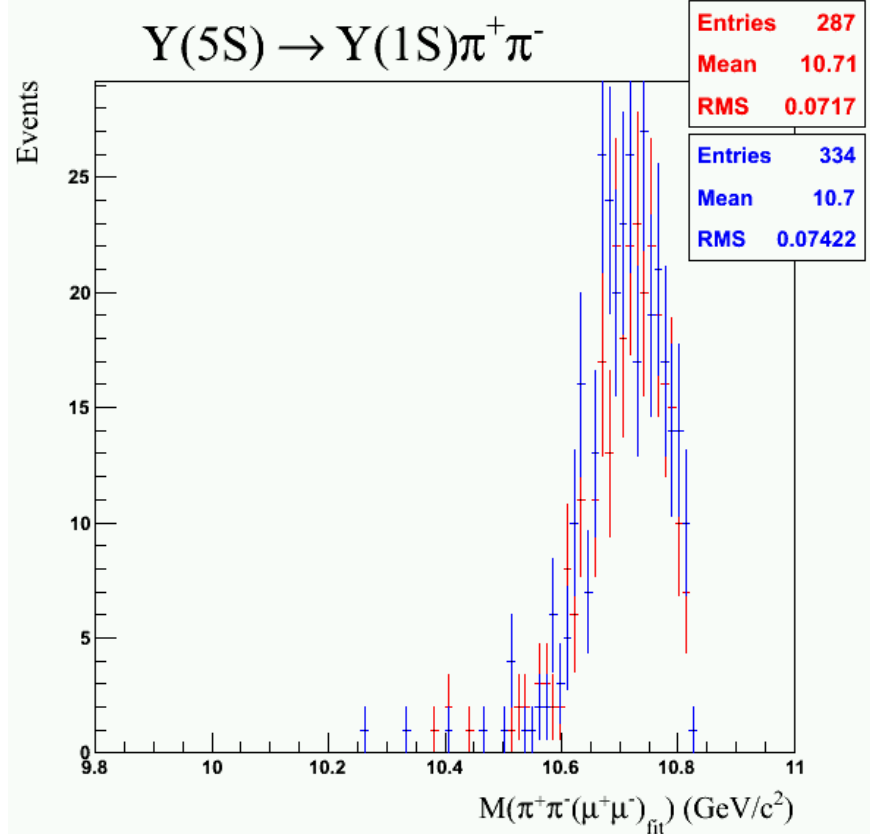


Figure 15: The distribution shown in blue is for events where $\Upsilon(5S) \rightarrow \Upsilon(1S)\pi^+\pi^-$ is generated using VVPIPI model [18] and $\Upsilon(1S) \rightarrow \mu^+\mu^-$ using VLL model [18]. The distribution shown in red is for events generated using PHSP model [18] for both processes. Neither samples contain ISR nor FSR, so they only differ by their decay models. The shapes of their $M(\pi^+\pi^-(\mu^+\mu^-)_{\text{fit}})$ distributions are very similar. Note that although there is a difference in efficiency between the two samples, this is unimportant for our analysis, because we are only interested in possible difference between the shapes of these distributions.

430 plots in Fig. 17. Imposing a selection on ΔE has only a small effect on the shape of these
 431 backgrounds in the signal region.

432 To determine if we can use this MC sample to estimate the number of background events
 433 in the signal region, we divide the grand sideband region shown in Fig. 18 into four smaller
 434 regions as defined in Table 8 and observe if the number of events in MC scales uniformly
 435 to data across all regions. Table 9 shows the number of ISR MC events and data events
 436 within the regions of interest. We see that ISR MC does not scale uniformly across all
 437 regions. While ISR studies improve the quality of our analysis and provide us with useful
 438 information about the shape of this background in the signal region, including ISR into our
 439 analysis does not sufficiently improve the scaling between data and MC in different regions
 440 of grand sideband.

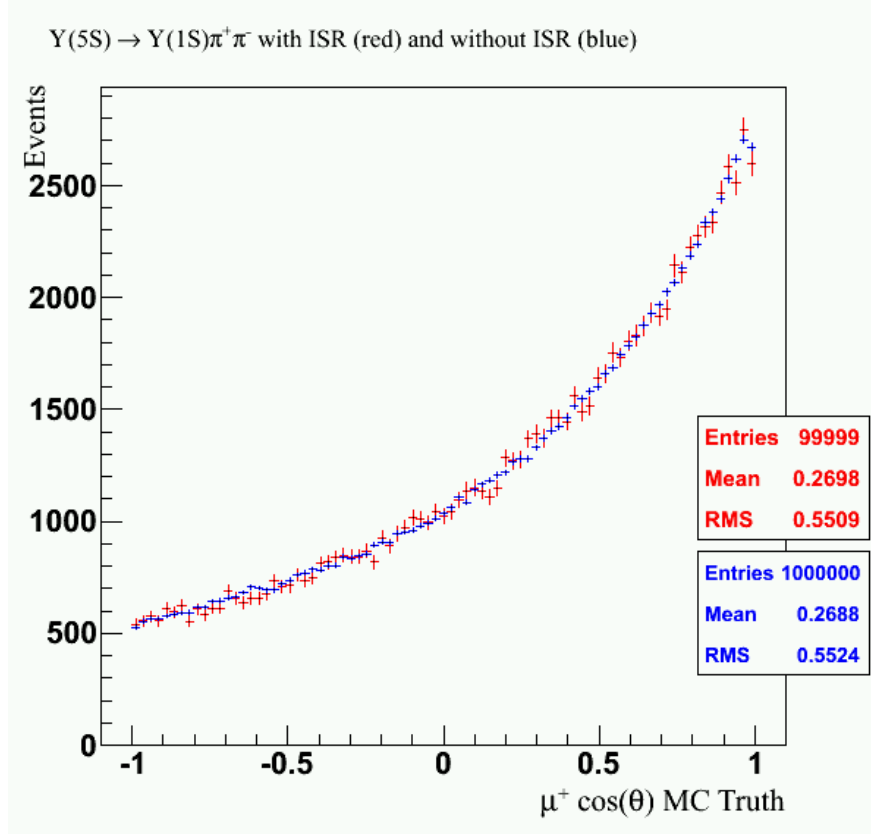


Figure 16: Distributions of $\cos \theta$ for μ^+ for $\Upsilon(5S) \rightarrow \Upsilon(1S)\pi^+\pi^-$ events. The distribution shown in red is for events generated with ISR while the distribution shown in blue is for events generated without ISR. Events in both distributions are generated using PHSP model for both $\Upsilon(5S) \rightarrow \Upsilon(1S)\pi^+\pi^-$ and $\Upsilon(1S) \rightarrow \mu^+\mu^-$. The blue distribution is normalized to the number of events in the red distribution.

Region Name	Boundary Definitions
Region 1	$10.72 \text{ GeV}/c^2 < M(\pi^+\pi^-(\mu^+\mu^-)_{\text{fit}}) < 10.80 \text{ GeV}/c^2$ $-0.2 \text{ GeV} < \Delta E < 0.2 \text{ GeV}$
Region 2	$10.49 \text{ GeV}/c^2 < M(\pi^+\pi^-(\mu^+\mu^-)_{\text{fit}}) < 10.72 \text{ GeV}/c^2$ $0.03 \text{ GeV} < \Delta E < 0.2 \text{ GeV}$
Region 3	$10.38 \text{ GeV}/c^2 < M(\pi^+\pi^-(\mu^+\mu^-)_{\text{fit}}) < 10.49 \text{ GeV}/c^2$ $-0.2 \text{ GeV} < \Delta E < 0.2 \text{ GeV}$
Excluded Region	$10.49 \text{ GeV}/c^2 < M(\pi^+\pi^-(\mu^+\mu^-)_{\text{fit}}) < 10.72 \text{ GeV}/c^2$ $-0.2 \text{ GeV} < \Delta E < 0.03 \text{ GeV}$

Table 8: Definitions of subdivisions of the grand sideband region. The Excluded Region is not considered in this analysis.

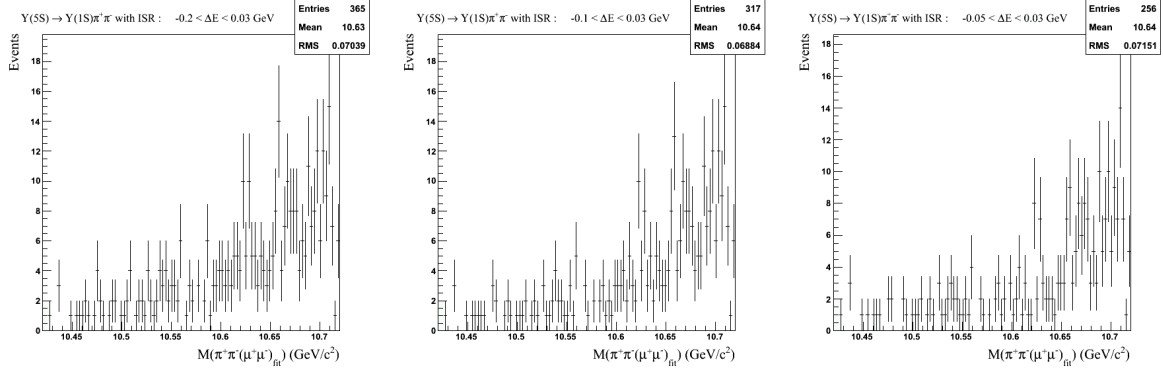


Figure 17: Distributions of $M(\pi^+\pi^-(\mu^+\mu^-)_{\text{fit}})$ for $\Upsilon(5S) \rightarrow \Upsilon(1S)\pi^+\pi^-$ with ISR in the signal region for different ΔE requirements. The leftmost distribution requires $-0.2 \text{ GeV} < \Delta E < 0.03 \text{ GeV}$, the middle distribution requires $-0.1 \text{ GeV} < \Delta E < 0.03 \text{ GeV}$, and the rightmost distribution requires $-0.05 \text{ GeV} < \Delta E < 0.03 \text{ GeV}$. The upper bound of ΔE is kept at 0.03 GeV for all distributions, since very few signal events fall beyond $\Delta E > 0.03 \text{ GeV}$.

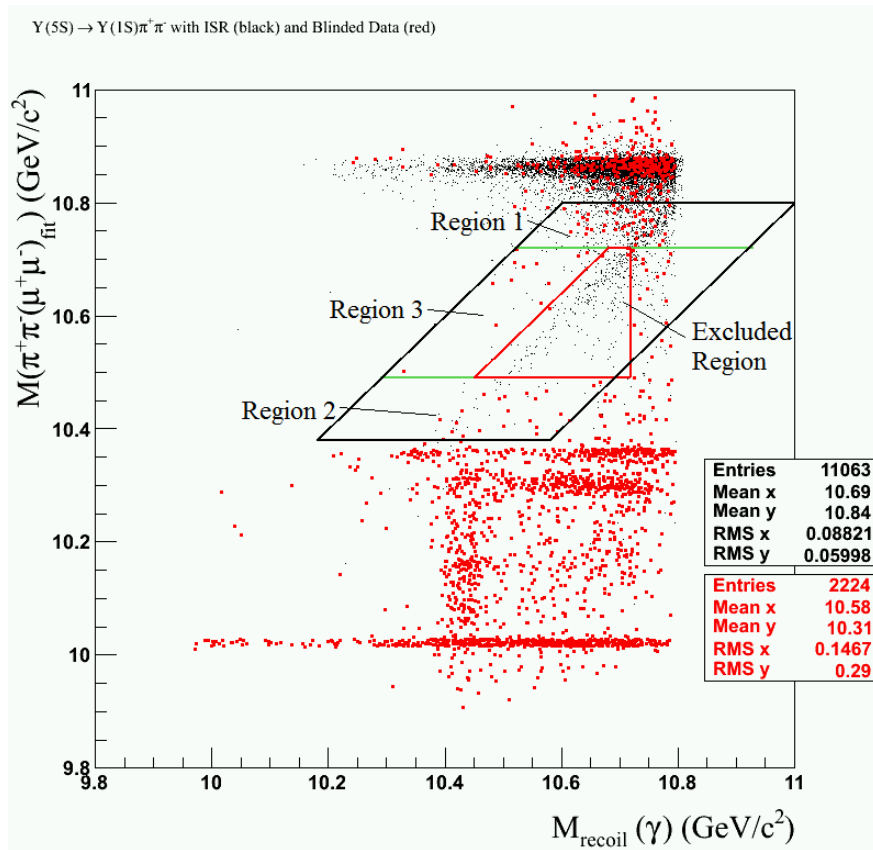


Figure 18: Subdivisions of the grand sideband region. The Excluded Region is not considered in this analysis.

Region	Number of events in ISR MC (N_{mc})	Number of events in blinded data (N_{data})	N_{mc}/N_{data}
Region 1	572	55	10.4
Region 2	28	23	1.2
Region 3	35	14	2.5

Table 9: Comparing the number of events in ISR MC and blinded data in the subdivided grand sideband region

7 Contribution from $\Upsilon(5S) \rightarrow Z_b^{(\prime)\pm} \pi^\mp$

Belle previously reported [15] that charged Z_b and Z_b' states comprise, respectively, approximately 2.54% and 1.04% of the 1819 $\Upsilon(1S)\pi^+\pi^-$ (followed by $\Upsilon(1S) \rightarrow \mu^+\mu^-$) events observed with the full data sample. The overall reconstruction efficiency in Z_b analysis was estimated to be around 46%. This allows us to estimate that, with an ideal, *i.e.* 100% efficient detector, we would expect to detect, approximately, 100 Z_b and 41 Z_b' events.

To estimate cross-feed between Z_b and W_{bj} analyses, we generated approximately 50,000 events for $\Upsilon(5S) \rightarrow Z_b^\pm \pi^\mp$ followed by $Z_b^\pm \rightarrow \Upsilon(1S)\pi^\mp$, $\Upsilon(1S) \rightarrow \mu^+\mu^-$. We also generated an additional 50,000 events for $\Upsilon(5S) \rightarrow Z_b'^\pm \pi^\mp$. These samples are 500 and 1000 larger than the numbers of such events which would be observed in data with an ideal detector.

The distribution of $M(\pi^+\pi^-(\mu^+\mu^-)_{\text{fit}})$ vs $M_{\text{rec}}(\gamma)$ is shown in Fig. 19 for both samples after applying our selection criteria for the W_{bj} analysis. Fig. 20 shows the distribution of $M(\pi^+\pi^-(\mu^+\mu^-)_{\text{fit}})$ for events inside the signal and sideband region. It is important to note that, approximately, only 2% of events fall in the signal region for each of the two samples. Therefore, we expect less than 100 events from each of the two Z_b samples to be found in the signal region for the W_{bj} analysis. As explained earlier in this section, to predict the ‘‘contamination’’ of our signal region by Z_b events, this number has to be scaled down by the factors of 500 and 1000 for contributions from Z_b and Z_b' , respectively. Therefore the process $\Upsilon(5S) \rightarrow Z_b^{(\prime)\pm} \pi^\mp$ in total, has negligible cross-feed contribution in the signal region and can be safely ignored.

8 Fitting

8.1 Signal and Background PDFs

To extract signal yield, we perform a one-dimensional extended unbinned ML fit to the variable $M(\pi^+\pi^-(\mu^+\mu^-)_{\text{fit}})$ using RooFit [22]. We model the signal distribution of $M(\pi^+\pi^-(\mu^+\mu^-)_{\text{fit}})$ as a Breit-Wigner convolved with the sum of two Gaussians (to simulate effects of detector resolution as shown in Fig. 6). The observed width and shape of $M(\pi^+\pi^-(\mu^+\mu^-)_{\text{fit}})$ distribution in signal MC remains practically the same after applying our ΔE requirement and after including ISR. Therefore, we fix the width of our signal PDF. We set the width of the Breit-Wigner to be $\sigma_{BW} = 15 \text{ MeV}/c^2$ to match the intrinsic width of Z_b and Z_b' . The

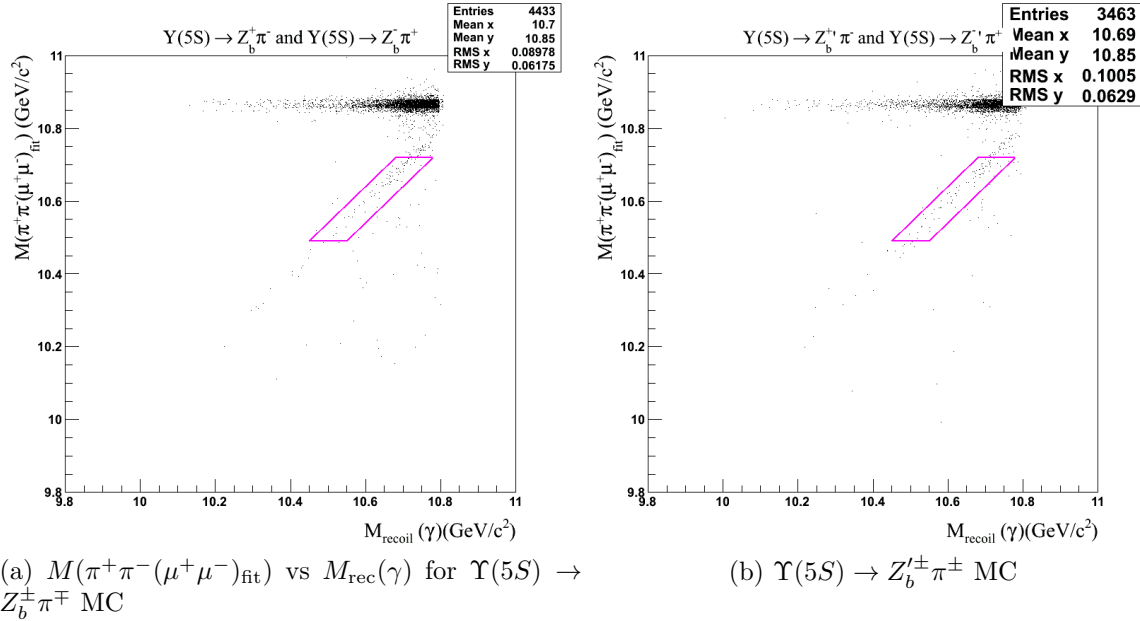
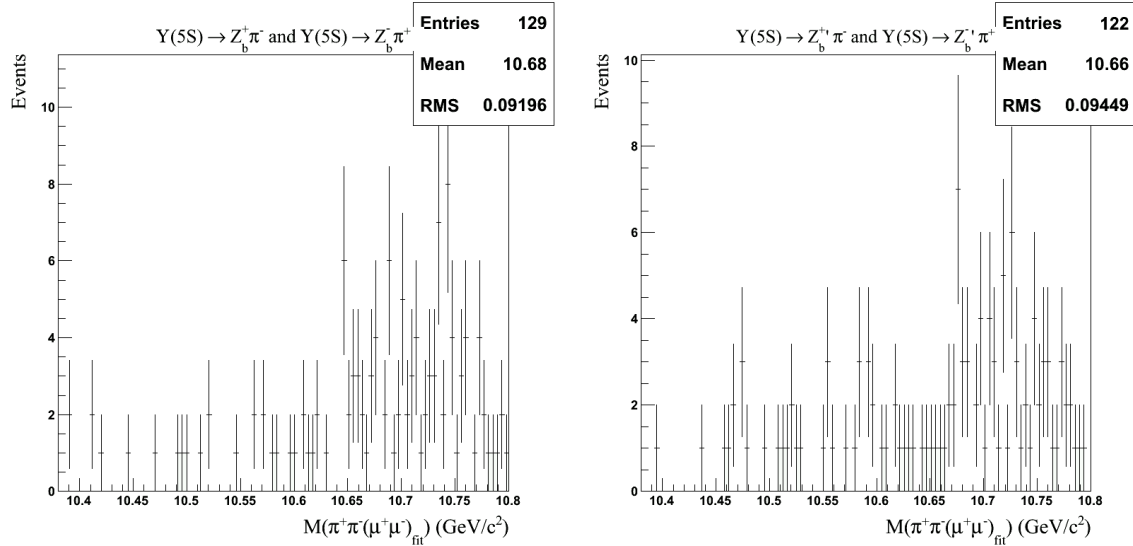


Figure 19: The distribution of $M(\pi^+\pi^-(\mu^+\mu^-)_{\text{fit}})$ vs $M_{\text{recoil}}(\gamma)$ for $\Upsilon(5S) \rightarrow Z_b^{(\prime)\pm}\pi^\mp$ MC.



(a) $M(\pi^+\pi^-(\mu^+\mu^-)_{\text{fit}})$ for $\Upsilon(5S) \rightarrow Z_b^\pm\pi^\mp$ MC. (b) $M(\pi^+\pi^-(\mu^+\mu^-)_{\text{fit}})$ for $\Upsilon(5S) \rightarrow Z_b^{\prime\pm}\pi^\mp$ MC.

Figure 20: The distribution of $M(\pi^+\pi^-(\mu^+\mu^-)_{\text{fit}})$ for $\Upsilon(5S) \rightarrow Z_b^{(\prime)\pm}\pi^\mp$ MC for events inside the signal and sideband region.

470 widths of the Gaussians used in convolution are $\sigma_{G_1} \approx 3 \text{ MeV}/c^2$ and $\sigma_{G_2} \approx 7.7 \text{ MeV}/c^2$ to
 471 match the widths obtained from the fit to $M(\pi^+\pi^-(\mu^+\mu^-)_{\text{fit}})$ resolution. We let the mean
 472 of Breit-Wigner float within the fit, as W_{bJ} could be observed at different invariant masses
 473 for different spins J . Table 10 lists the values of parameters used in our signal PDF model.
 474 We use an exponential $e^{\lambda x}$ to model background contributions due to ISR as well as

Quantity	Value Used in Signal PDF (MeV/c ²)
σ_{BW}	15
Mean of BW	floats between 10.38 and 10.80 GeV/c ²
σ_{G_1}	3.0 ± 0.1
σ_{G_2}	7.7 ± 0.2
Fraction of Gaussian 1	0.73 ± 0.01
Fraction of Gaussian 2	0.27 ± 0.01
Mean of both Gaussians	$(-3.8 \pm 0.2) \cdot 10^{-4}$

Table 10: Values of fixed quantities in the signal PDF model.

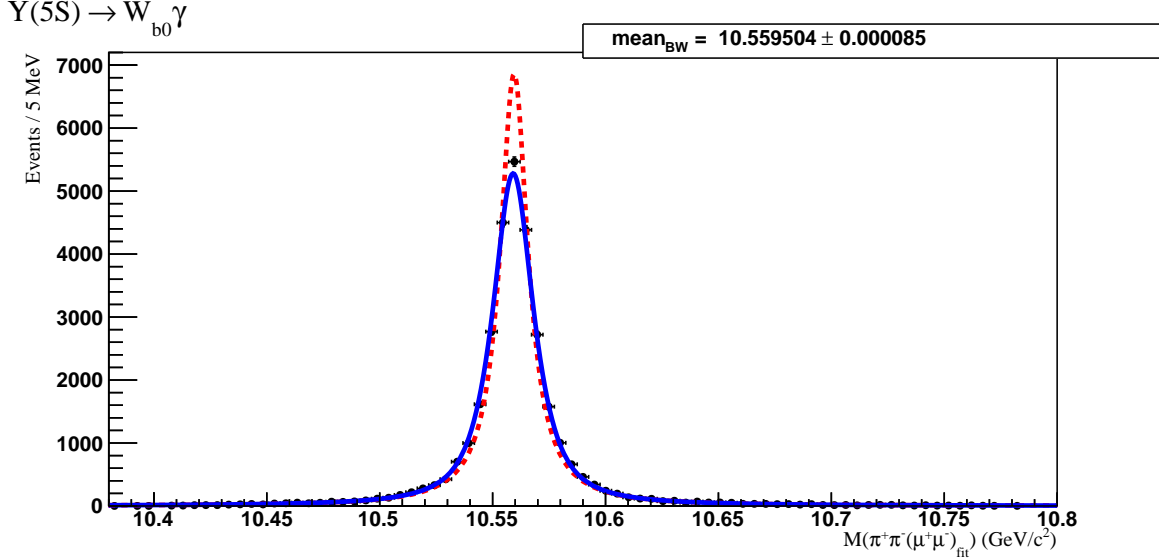
475 possible non-resonant contribution from dimuon continuum events. Strictly speaking, the
476 background distribution deviates from an exponential at $M(\pi^+\pi^-(\mu^+\mu^-)_{\text{fit}}) \approx 10.75$ GeV/c².
477 because of the phase space boundary at $M_{\text{rec}}(\gamma) \approx 10.75$ GeV/c² seen in Fig. 5. This
478 ever-present effect can be seen in figures showing the distribution of $M(\pi^+\pi^-(\mu^+\mu^-)_{\text{fit}})$ for
479 background events with our ΔE requirement (*e.g.* see Fig. 15, Fig. 21b, Fig. 21c). This
480 shortcoming of our analysis will be taken care of in the next version of this Note. We would
481 like to remark that the observed fall-off effect is easy to understand and describe in the
482 model used for fitting, as it is exclusively due to the boundary of phase space.

483 To estimate the number of background events we expect in the signal region, we per-
484 form an extended unbinned maximum likelihood fit to data only in the sideband regions.
485 To account for uncertainty in the number of data events in the sideband region, we fit
486 $M(\pi^+\pi^-(\mu^+\mu^-)_{\text{fit}})$ within the range of 10.38 GeV/c² and 10.80 GeV/c² when extracting
487 signal yield. This range corresponds to the signal region and sideband regions combined.
488 From the fit, we obtain $\lambda = 3.7951$. We extract 59 ± 11 background events in the signal
489 region and sideband regions combined. We expect 27 ± 5 of these background events to be
490 in the signal region alone. Fits to W_{b0} signal MC, $\Upsilon(5S) \rightarrow \Upsilon(1S)\pi^+\pi^-$ MC with ISR MC,
491 and data in the sidebands are shown in Fig. 21.

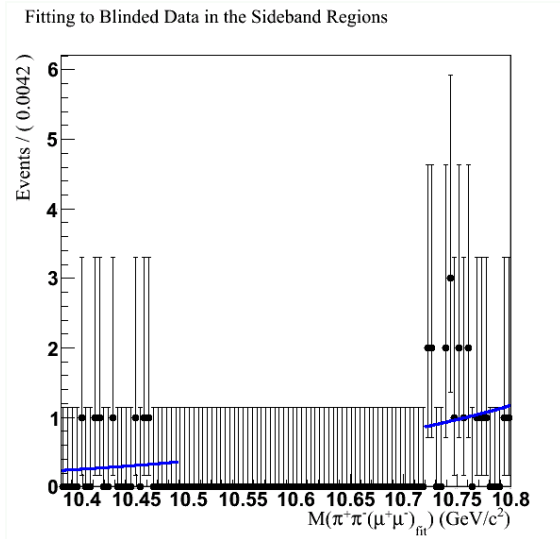
492 8.2 Confidence Belts

493 To construct a 90% confidence belt (with 5% on each side of the belt), we perform ensemble
494 tests. Each ensemble test consists of 1000 toy MC experiments. In each toy MC experiment,
495 we generate N_{sig} signal events and N_{bkg} background events according to their respective
496 PDF lineshapes used for fitting signal and background. We then fit the generated events in
497 the range $10.38 \text{ GeV}/c^2 < M(\pi^+\pi^-(\mu^+\mu^-)_{\text{fit}}) < 10.80 \text{ GeV}/c^2$ to our combined signal and
498 background PDF to extract the fitted number of signal events $N_{\text{sig}}^{\text{fit}}$.

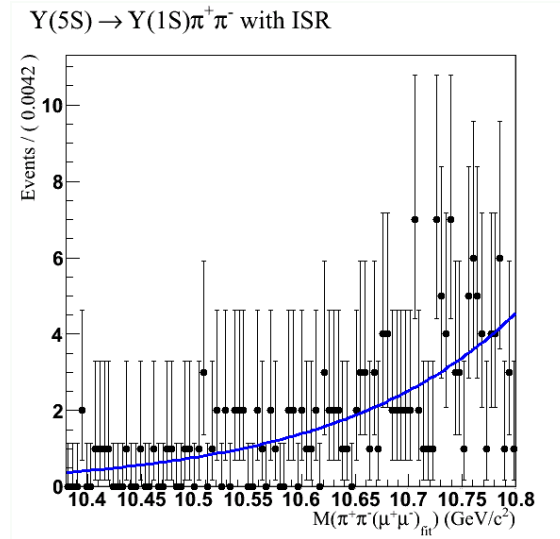
499 We construct our 90% confidence belt by performing ensemble tests with $N_{\text{bkg}}^{\text{gen}} = 59$ for
500 values of $N_{\text{sig}}^{\text{gen}}$ from 0 to 70. We additionally construct a 90% confidence belt where we allow
501 Poisson fluctuation in $N_{\text{bkg}}^{\text{gen}}$. These confidence belts are shown in Fig. 22.



(a) Fit result for the distribution of $M(\pi^+\pi^-(\mu^+\mu^-)_{\text{fit}})$ for signal MC in the signal and sideband region. The Breit-Wigner shape is shown in red. The blue distribution is the Breit-Wigner convolved with the sum of two Gaussians.



(b) Fit result for the distribution of $M(\pi^+\pi^-(\mu^+\mu^-)_{\text{fit}})$ for data in the sideband region.

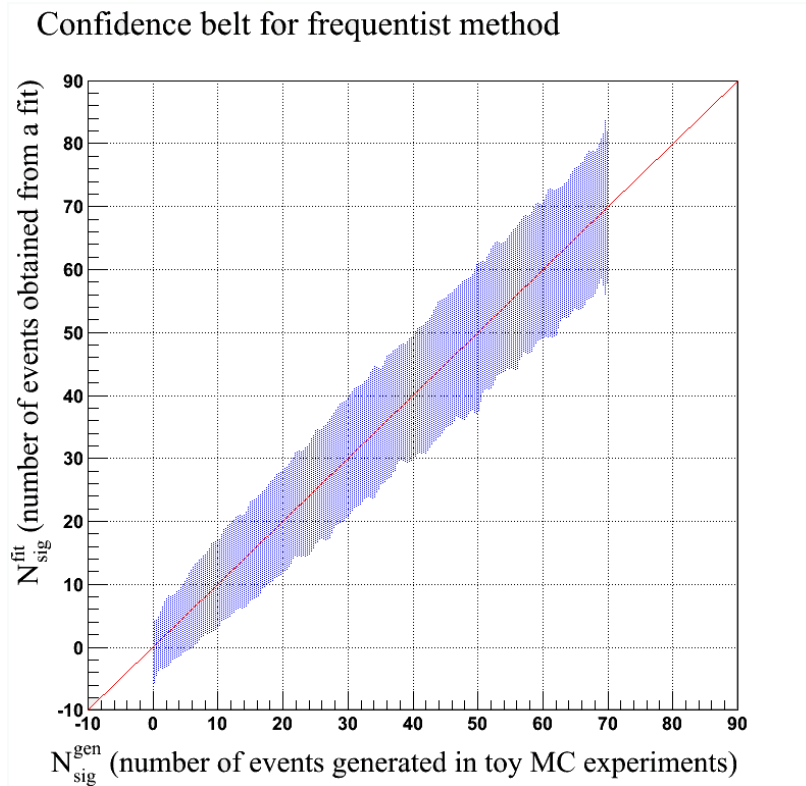


(c) Fit result for the distribution of $M(\pi^+\pi^-(\mu^+\mu^-)_{\text{fit}})$ for $\Upsilon(5S) \rightarrow \Upsilon(1S)\pi^+\pi^-$ with ISR for events in the signal region.

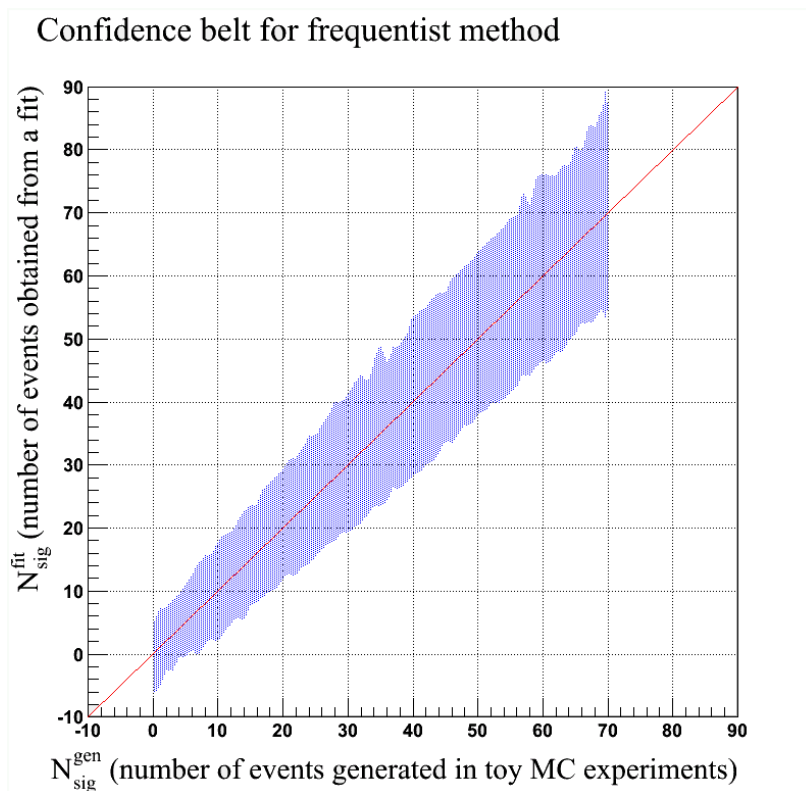
Figure 21: Fitting background MC and data

502 8.3 Linearity Study

503 To validate our fitting procedures, we perform a linearity study using ensemble tests. En-
 504 semble tests are generated as described in Section 8.2. For each ensemble test of 1000 toy
 505 MC experiments, we calculate the average number of signal events from the fit and the error
 506 associated with the average. We vary $N_{\text{sig}}^{\text{gen}}$ from 0 to 10 in steps of 1 and from 10 to 50 in
 507 steps of 5 while fixing $N_{\text{bkg}} = 59$.



(a) Does not include Poisson fluctuations in $N_{\text{bkg}}^{\text{gen}}$



(b) Includes Poisson fluctuations in $N_{\text{bkg}}^{\text{gen}}$.

Figure 22: 90% confidence belts for frequentist method.

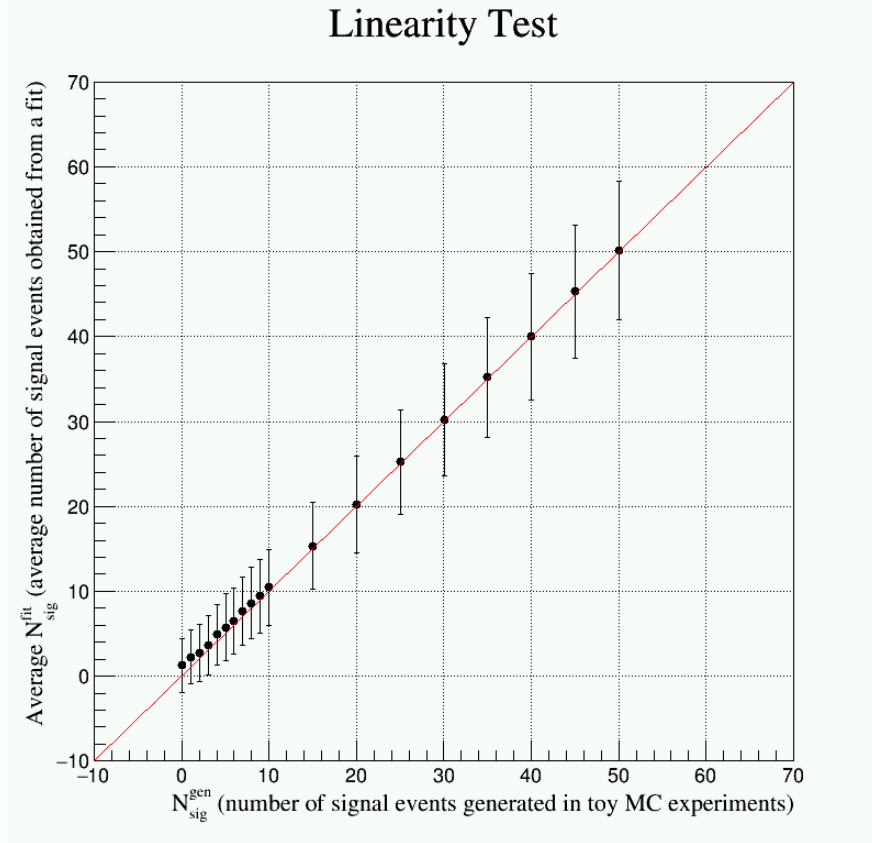
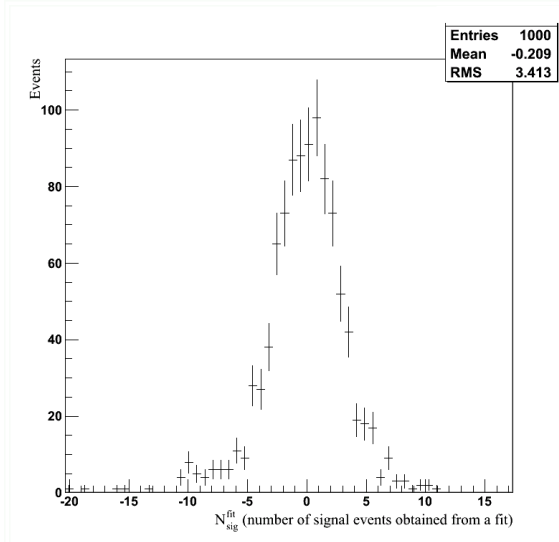


Figure 23: Average $N_{\text{sig}}^{\text{fit}}$ for varying values of $N_{\text{sig}}^{\text{gen}}$. The solid black line is the result of fitting these points to the linear function $f(x) = p_0 + p_1x$. The resulting fit parameters are shown in the box on the top right.

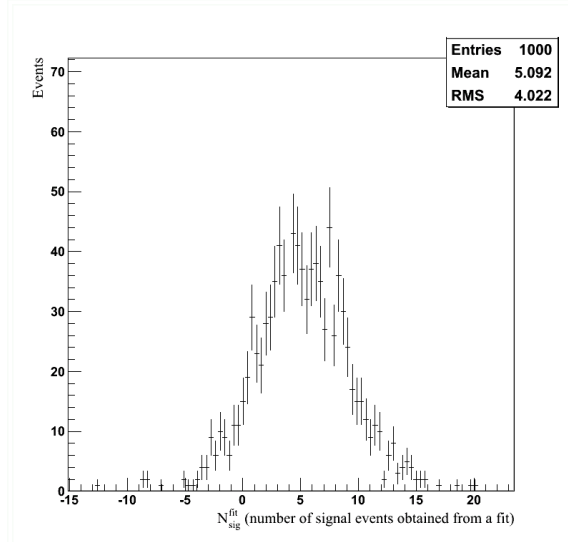
508 We plot the average number of signal events from the fit against $N_{\text{sig}}^{\text{gen}}$ and perform a fit
509 to a linear function $f(x) = p_0 + p_1x$. This plot and the results of the linear fit are shown
510 in Fig. 23. Fig. 24 displays distributions of $N_{\text{sig}}^{\text{fit}}$ for certain values of $N_{\text{sig}}^{\text{gen}}$. When $N_{\text{sig}}^{\text{gen}}$ is
511 large, the distribution of $N_{\text{sig}}^{\text{fit}}$ is unbiased. However, for small $N_{\text{sig}}^{\text{gen}}$, we see an asymmetry
512 in the distribution of $N_{\text{sig}}^{\text{fit}}$, indicating some bias. This effect is often observed for small
513 statistics and is not unexpected.

514 8.4 Sensitivity Estimation

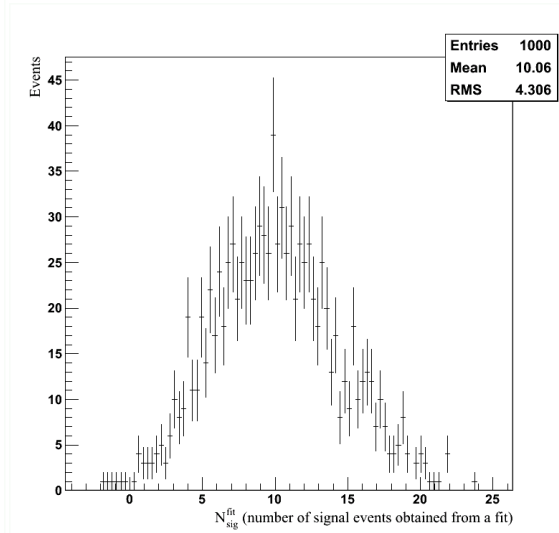
515 We estimate the upper limit on the branching fraction and visible cross section of $\Upsilon(5S) \rightarrow$
516 γW_{bJ} in the absence of signal by performing an extended unbinned maximum likelihood fit
517 on toy MC generated according to the fit to the data sidebands. We generate 1000 toy MC
518 samples with 59 background events, fit our combined signal and background shape to each
519 sample, and then average the resulting signal yields. There is an average signal yield of
520 -0.2 ± 3.2 events. Note that in Fig. 23, this average signal yield corresponds to the value
521 plotted at $N_{\text{sig}}^{\text{gen}} = 0$. Using the confidence belt in Fig. 22, we determine the 95% confidence
522 level upper limit on the number of signal events to be 10 events. We calculate the upper



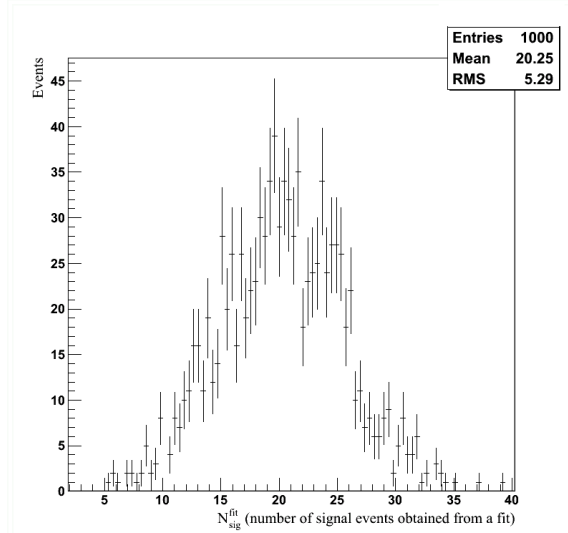
(a) Distribution of $N_{\text{sig}}^{\text{fit}}$ for an ensemble test with $N_{\text{sig}}^{\text{gen}} = 0$ and $N_{\text{bkg}}^{\text{gen}} = 59$.



(b) Distribution of $N_{\text{sig}}^{\text{fit}}$ for an ensemble test with $N_{\text{sig}}^{\text{gen}} = 5$ and $N_{\text{bkg}}^{\text{gen}} = 59$.



(c) Distribution of $N_{\text{sig}}^{\text{fit}}$ for an ensemble test with $N_{\text{sig}}^{\text{gen}} = 10$ and $N_{\text{bkg}}^{\text{gen}} = 59$.



(d) Distribution of $N_{\text{sig}}^{\text{fit}}$ for an ensemble test with $N_{\text{sig}}^{\text{gen}} = 20$ and $N_{\text{bkg}}^{\text{gen}} = 59$.

Figure 24: $N_{\text{sig}}^{\text{fit}}$ Distributions for ensemble tests with different $N_{\text{sig}}^{\text{gen}}$.

523 limit on the branching fraction in the absence of signal as follows:

$$\mathcal{B}(\Upsilon(5S) \rightarrow \gamma W_{bJ}) \cdot \mathcal{B}(W_{bJ} \rightarrow \Upsilon(1S)\rho^0) = \frac{N_{\text{sig}}}{\epsilon \cdot N_{\Upsilon(5S)} \cdot \mathcal{B}(\Upsilon(1S) \rightarrow \mu^+\mu^-) \cdot \mathcal{B}(\rho^0 \rightarrow \pi^+\pi^-)} \quad (4)$$

524 where $N_{\Upsilon(5S)}$ is the number of $\Upsilon(5S)$ and ϵ is our reconstruction efficiency. Using Eq. 4, we
 525 determine the upper limit on the branching fraction in the absence of signal to be 2.4×10^{-5} .

526 We calculate the visible cross section using

Quantity	Value
N_{sig}	10
ϵ	$(29 \pm 0.17)\%$
$N_{\Upsilon(5S)}$	$(6.53 \pm 0.66) \cdot 10^6$
$\mathcal{B}(\Upsilon(1S) \rightarrow \mu^+\mu^-)$	$(2.48 \pm 0.05)\%$
$\mathcal{B}(\rho^0 \rightarrow \pi^+\pi^-)$	99.8%
\mathcal{L}	121.4 fb^{-1}

Table 11: Values of quantities used to calculate upper limits on visible cross section and the branching fraction. Uncertainty in $\mathcal{B}(\rho^0 \rightarrow \pi^+\pi^-)$ is negligible. Note that, for purposes of estimating upper limits, we use $N_{\text{sig}} = 10$, which is the 95% CL boundary of the 90% CL frequentist belt shown in Fig. 22 for $N_{\text{sig}}^{\text{fit}} = 3$, according to the result of the fit $N_{\text{sig}}^{\text{fit}} = -0.2 \pm 3.2$.

$$\sigma_{\text{vis}} = \frac{N_{\text{sig}}}{\epsilon \mathcal{B}(\Upsilon(1S) \rightarrow \mu^+\mu^-) \mathcal{B}(\rho^0 \rightarrow \pi^+\pi^-) \mathcal{L}} \quad (5)$$

where \mathcal{L} is the integrated luminosity. We find $\sigma_{\text{vis}} = (0.115 \pm 0.006) \text{ fb}$. All values used to calculate the branching fraction and visible cross section are shown in Table 11.

9 Search Strategy Summary

In this analysis, we describe a search for a new molecular state W_{bJ} which could be produced in the radiative transition $\Upsilon(5S) \rightarrow \gamma W_{bJ}$ followed by the decays $W_{bJ} \rightarrow \Upsilon(1S)\rho^0$, $\Upsilon(1S) \rightarrow \mu^+\mu^-$, $\rho^0 \rightarrow \pi^+\pi^-$. We fully reconstruct the signal final state consisting of two muons, two pions, and a photon. We perform a blind analysis by optimizing our selection criteria and analysis techniques using only MC samples before applying them to data.

To search for the presence of W_{bJ} in Belle data, we propose to "unblind" the data in the signal region and then fit a one-dimensional distribution of $M(\pi^+\pi^-(\mu^+\mu^-)_{\text{fit}})$ using the aforementioned models for signal and background shapes. In the fit, we fix the width of W_{bJ} to that of Z_b . Because we expect only one signal in our signal region, we plan to scan the range of invariant masses of $M(\pi^+\pi^-(\mu^+\mu^-)_{\text{fit}})$ and, for each assumed value of the invariant mass, we perform a fit to data, where the background parameter λ is allowed to float. If the fit returns a statistically significant result, we claim a discovery. We will then produce a plot of the upper limit versus mass of W_{bJ} . This plot will be produced regardless of whether or not the fit yields a significant result. Our confidence belt (Fig. 22) will be used to either claim a discovery of W_{bJ} or establish an upper limit on the signal production rate (branching fraction) for the radiative decay $\Upsilon(5S) \rightarrow \gamma W_{bJ}$. The following sources of systematic uncertainties will be considered in our final estimate of the upper limit of the branching fraction of $\Upsilon(5S) \rightarrow \gamma W_{bJ}$:

- Number of $\Upsilon(5S)$

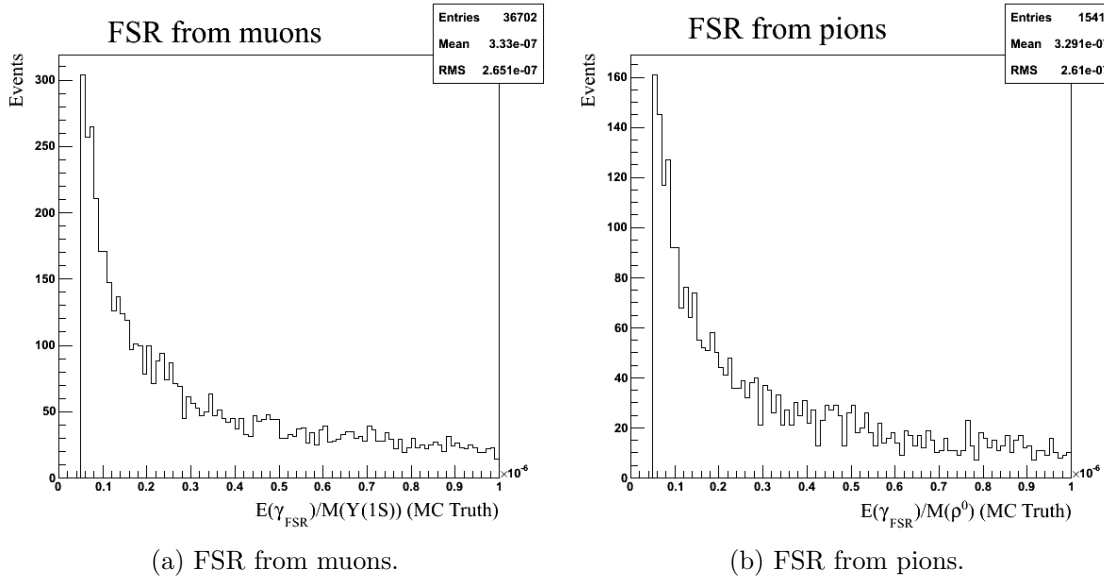


Figure 25: Final state radiation from charged tracks

- 549 • Signal Reconstruction Efficiency
- 550 • Daughter Branching Fractions
- 551 • MC statistics
- 552 • PDF parameterization
- 553 • Fit bias
- 554 • Trigger efficiency

555 10 Appendix

556 10.1 Final State Radiation

557 In the version of package PHOTOS used by Belle, the minimum FSR photon energy (eval-
558 uated in the center of mass frame of charged particle's parent) is calculated as follows:

$$E(\gamma_{FSR}) = (\text{XPHCUT}) \cdot 0.5 \cdot M(\text{parent}) \quad (6)$$

559 where XPHCUT is a hardcoded constant set to 0.01. Hence, the minimum FSR energy is
560 approximately 4 MeV for pions ($M(\rho^0) = 770$ MeV) and 50 MeV for muons ($M(\Upsilon(1S)) =$
561 9.46 GeV). The lower limit on FSR energy for muons is too high, so we lowered the
562 value of XPHCUT to 10^{-7} . To accomplish this, we changed XPHCUT=0.01D0 to XPH-
563 CUT=0.0000001D0, recompiled the phocin.F source code and then rebuilt EvtGen with an
564 updated PHOTOS library.

565 To verify that XPHCUT was successfully lowered to 10^{-7} , we plot the ratios $\frac{E(\gamma_{FSR})}{M(\Upsilon(1S))}$
566 and $\frac{E(\gamma_{FSR}^{\rho})}{M(\rho)}$ as generated in Fig. 25. Because these quantities are bounded from below by
567 $XPHCUT \cdot 0.5$, we prove that XPHCUT was successfully lowered.

568 10.2 Changes in the Analysis between Note v1.5 and v2.0

569 In this section we describe and explain the reasons for important changes we made in the
570 analysis after Note v1.0 was released. These changes have not yet been applied to the main
571 body of the text. All plots – except those in this and the next sections of this Note (v1.5)
572 – have been made using the selection developed in the original analysis. The next version
573 of this Note (v2.0) will have some of the critical plots and tables in the main section of the
574 note updated to reflect for the changes described below.

575 Overall, there are four changes in the analysis related to (1) photon energy selection
576 (extended), (2) the region blinded in data (increased), (3) selection criteria on dr and dz
577 (relaxed) and (4) PID requirements for charged pions (removed).

578 The main improvement (extending signal photon energy spectrum) helps us to develop
579 a robust and reliable approach to fitting the signal invariant mass spectrum (to be applied
580 to data when the permission to open the signal region is secured). Extending the blinded
581 region in data was done to avoid an annoying “undercoverage” demonstrated in Fig. 7 of
582 Note v1.1, *i.e.* our decision to impose a requirement on ΔE was made after we had defined
583 the blinded region, and hence, the top right corner of the signal region was not blinded
584 originally. While no signal is expected in that corner, we would prefer to blind the entire
585 signal region to simplify fitting. We deemed the changes in the selection applied to track
586 impact parameters to be “right”, so no additional systematics needs to be included in the
587 result of the analysis. For the same reason we decided to remove PID cuts for charged pion
588 candidates: any such selection criterion costs us some (even if very small) efficiency loss,
589 and, more importantly, has some systematic uncertainty associated with it. We made the
590 changes in PID and impact parameters selection just because we had to reskim the data and
591 generic MC anyway.

592 The four changes are itemized (and elaborated more on) below, starting with the most
593 important improvement in the analysis:

594 • Signal Photon Energy

595 In the first version of this Note, as shown in Table 3, signal photon candidates were
596 selected in the range between 100 and 600 MeV. As you can see in Fig. 4a of this
597 version of the Note, this energy range is sufficient for signal photon selection, how-
598 ever, we found it to be very restrictive for purposes of fitting the signal invariant
599 mass $M(\pi^+\pi^-(\mu^+\mu^-)_{\text{fit}})$ including the sidebands. This effect is explained better in a
600 dedicated subsection below.

601 • Blinded Region in Data

602 As we already explained, our original blinding (which we decided about before we
603 developed the fitting procedure) inadvertently exposed one corner of the signal region in
604 data to possible inspection. This possibly introduces some bias, but more importantly

Region Name	Boundary Definitions
The New Blinded Region	$10.49 \text{ GeV}/c^2 \leq M(\pi^+\pi^-(\mu^+\mu^-)_{\text{fit}}) \leq 10.72 \text{ GeV}/c^2$ $M_{\text{rec}}(\gamma) \geq M(\pi^+\pi^-(\mu^+\mu^-)_{\text{fit}}) - 0.04 \text{ GeV}/c^2$ $M_{\text{rec}}(\gamma) \leq 11.0 \text{ GeV}/c^2$

Table 12: The new (wider) blinded region in data. The important change is shown in red color. However, it is redundant and adds nothing new as compared to the second line in this table.

605 makes the fitting of the $M(\pi^+\pi^-(\mu^+\mu^-)_{\text{fit}})$ distribution slightly more difficult. As
606 we had to reskim the data and repeat all analysis steps, we decided to extend the
607 blinded region as shown in Table 12. Please compare this with Table 5 in the original
608 version of the note. In one sentence, we blinded the entire right-side tail of the $M_{\text{rec}}(\gamma)$
609 distribution. Note that the change shown in red color in this table is not even necessary:
610 the second line of the boundary described in the table is sufficient to achieve our goal.
611 We show the third line in the table only so the comparison with the previous version
612 of this Note is easier to make.

613 • **Impact Parameters for Charged Tracks**

614 The dz and dr selection criteria have been loosened to ≤ 4 cm and ≤ 0.5 cm, respec-
615 tively.

616 • **PID Requirements for Charged Pion Candidates**

617 These requirements have been eliminated.

618 As we already mentioned, these four changes in the selection criteria required us to reskim
619 generic MC and data. That was easy.

620 **10.2.1 Signal Photon Energy Conundrum**

621 Well, retrospectively, extending signal photon energy selection was not really a very difficult
622 decision, but it requires a thorough explanation. Below we try our best to walk the reader
623 through the logic of our decision.

624 In our analysis we extract the signal yield by fitting the distribution of the signal invariant
625 mass $M(\pi^+\pi^-(\mu^+\mu^-)_{\text{fit}})$. We are confident (because we proved this) that we observe the ISR
626 background (*i.e.* events where the production of $\Upsilon(5S)$ is accompanied by some initial state
627 radiation). However, we suspect that there are other sources of non-peaking background,
628 such as, *e.g.* poorly reconstructed events of all possible types, cosmic events overlapping
629 with incompletely reconstructed collision events – you name it – present in data. The key
630 part of our approach to fitting is that, on basis of our extensive and thorough studies of
631 non-signal data and generic MC, we expect no peaking backgrounds to be present in the
632 signal region.

633 For as long as no bias is present in selecting signal event candidates, background events
634 of ISR origin are relatively well described (as you will see for yourself very soon) by the sum

635 of an exponential and a straight line of non-negative slope. Small non-peaking background is
 636 likely to be sufficiently-well approximated also by the same straight line (of zero or positive
 637 slope). However, our original selection criteria strongly suppressed ISR background at large
 638 values of the signal invariant mass $M(\pi^+\pi^-(\mu^+\mu^-)_{\text{fit}})$, making it very difficult to reliably
 639 obtain the shape of such biased background distribution using sidebands in data. We realized
 640 that, in order to significantly reduce such possible bias, we have to avoid suppressing ISR
 641 background in the sideband region.

642 To demonstrate the effect we are trying to explain in this section, we generated a some-
 643 what ridiculous MC sample, where an incredibly broad “structure” (an almost flat distribu-
 644 tion of the invariant mass called, for purposes of MC production, “ $\Upsilon(5S)$ ” (which it is most
 645 definitely not!)) was generated along with ISR in the e^+e^- annihilation followed by this
 646 structure’s “decay” to $\Upsilon(1S)\pi^+\pi^-$. Applying our selection criteria to such MC sample after
 647 detector simulation and reconstruction allows us to investigate the phase space of relevant
 648 kinematic parameters at sufficient level of precision to make meaningful conclusions. Note
 649 that we do not even try to reweight the ISR energy spectrum in this exercise, because all we
 650 need for our studies is a good coverage of phase space (which is already a good enough of a
 651 reason NOT to reweight such MC!).

652 We start by demonstrating, in Fig. 26, that, with the original signal photon energy
 653 selection, the reconstructed ISR background does not resemble an exponent in the signal
 654 plus sideband region of the invariant mass $M(\pi^+\pi^-(\mu^+\mu^-)_{\text{fit}})$ (indicated by vertical lines
 655 in this figure). The explanation for the observed shape lies in the cut on signal photon
 656 energy requiring at least 100 MeV. Further, Fig. 27, where we show the 2D distribution
 657 of the reconstructed signal photon energy (in the lab) vs $M(\pi^+\pi^-(\mu^+\mu^-)_{\text{fit}})$, demonstrates
 658 that the range of the invariant mass $M(\pi^+\pi^-(\mu^+\mu^-)_{\text{fit}})$ is actually biased on both ends of
 659 the spectrum – at higher masses because of the 100 MeV cut, at smaller masses because
 660 of the 600 MeV cut. Note that the relevant value of the invariant mass, where the ISR
 661 background is suppressed by the 100 MeV cut, is located at the intersection of the left-side
 662 of the “opening cone” of phase space with the horizontal line of the 100 MeV cut on the
 663 photon energy. Note that the opening angle of the cone describing the phase space is due to
 664 the ΔE selection, which we keep to be $-0.05 \text{ GeV} \leq \Delta E \leq 0.03 \text{ GeV}$.

665 In order to avoid the described bias in background photon energy spectrum and to be
 666 able to use the higher-mass sideband to perform a robust fit to such background, we release
 667 the cut on signal photon energy to the lowest possible value of 20 MeV (standard Belle
 668 reconstruction and MDST production do not go lower than that). Note that in our analysis
 669 we do not really care about possible energy dependence of photon reconstruction efficiency
 670 systematic uncertainty, because our signal is associated with photons of higher energy, but
 671 we need (even if smoothly suppressed) an exponential-like energy distribution of background
 672 photons to make extracting the signal from data reliable. In our approach we obtain the
 673 shape of background distribution from data also.

674 Interestingly, to improve our understanding of backgrounds, we also have to raise the
 675 cut on the other end of the photon energy region, though, in this case, for a different
 676 reason. As is explained in Table 6 and Fig. 10 of the original version of the note, there is
 677 a particular peaking background, namely, radiative (*i.e.* ISR) production of $\Upsilon(3S)$ followed
 678 by its dipion transition to $\Upsilon(1S)$, which is uncomfortably too close to the left side of our
 679 signal plus sideband region of $M(\pi^+\pi^-(\mu^+\mu^-)_{\text{fit}})$. When both charged pions and the photon

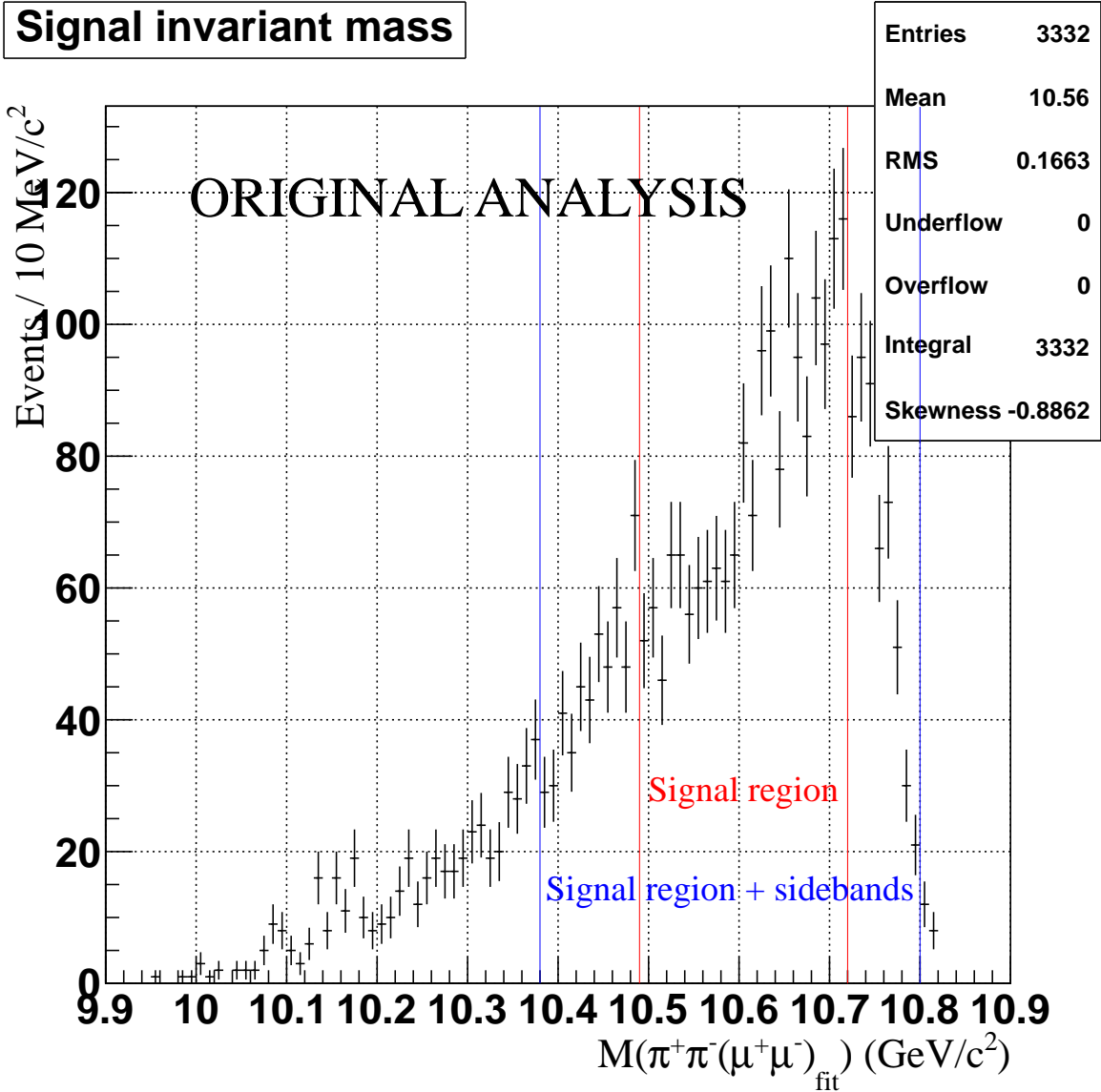


Figure 26: The reconstructed invariant mass $M(\pi^+\pi^-(\mu^+\mu^-)_{\text{fit}})$ for a special ISR MC sample with the original selection criteria. Only best candidates are shown.

680 are misreconstructed, sometimes this unfortunate happenstance might shift some of such
 681 these events into the signal region. Therefore, it would be best to investigate this possible
 682 background using the data. This goal requires us to release the signal photon energy cut.
 683 For practical purposes, in the improved version of the analysis, we limit signal photon energy
 684 to 5 GeV. Note that our approach also facilitates possible measurement of ISR production
 685 of $\Upsilon(3S)$ and $\Upsilon(2S)$, which could be used to calibrate ISR MC.

686 After widening the signal photon candidate energy selection as described and explained,
 687 we plot the distributions of photon energy spectrum vs $M(\pi^+\pi^-(\mu^+\mu^-)_{\text{fit}})$ in Fig. 28 and
 688 $M(\pi^+\pi^-(\mu^+\mu^-)_{\text{fit}})$ in Fig. 29 (as always, for best candidates only) for MC events from our
 689 “ridiculous” background MC sample. We conclude that the current (*i.e.* new, relaxed) se-
 690 lection criteria allow us to perform a robust fit to the background using the sidebands of

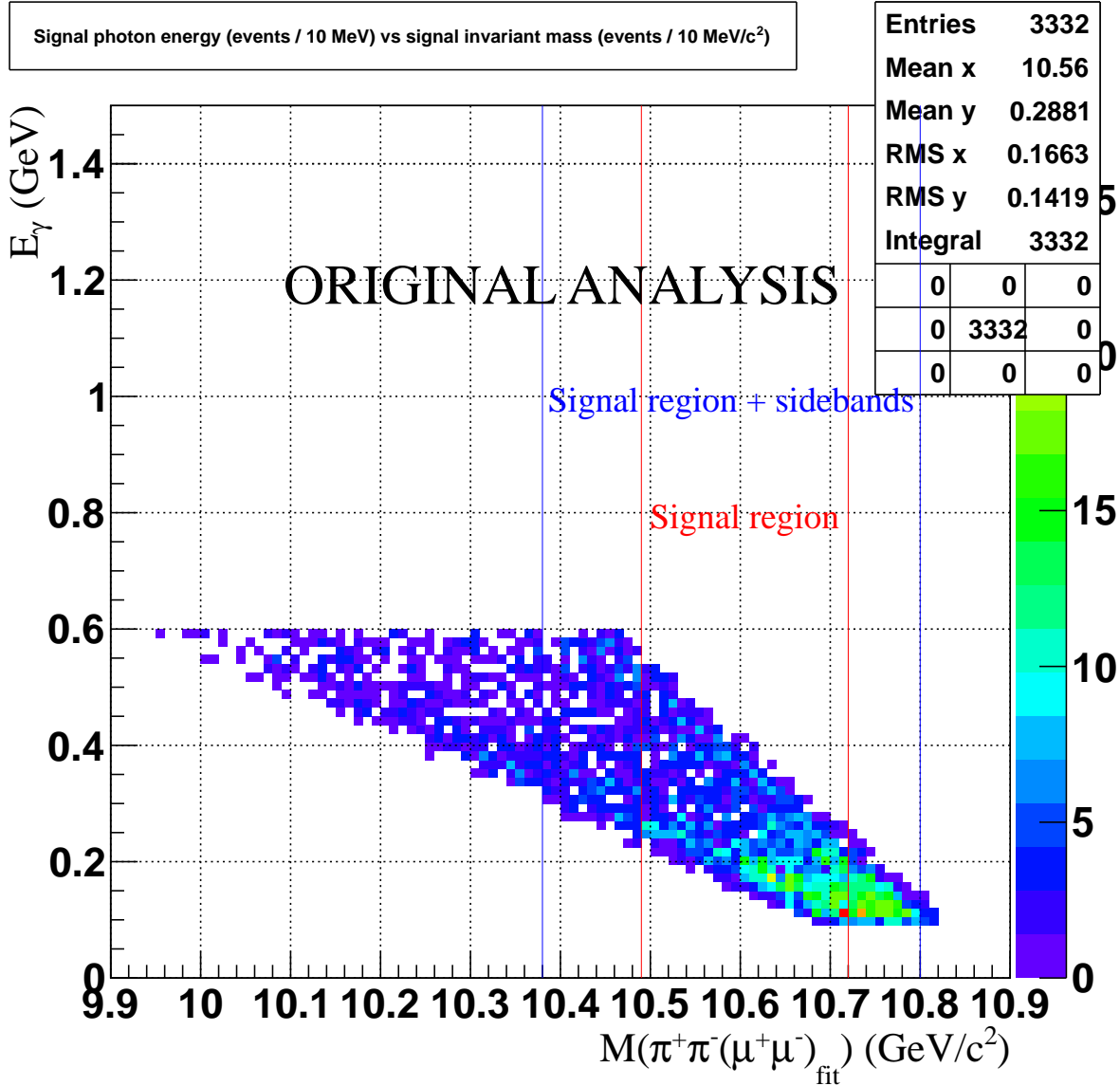


Figure 27: The reconstructed signal photon energy versus the invariant mass $wbjm$ for a special ISR MC sample with the original selection criteria. Only best candidates are shown.

691 $M(\pi^+\pi^-(\mu^+\mu^-)_{\text{fit}})$ for the values of this variable up to 10.78 GeV/c². To further investi-
 692 gate the shape of $M(\pi^+\pi^-(\mu^+\mu^-)_{\text{fit}})$ in this special MC sample, we plot the distribution of
 693 $M(\pi^+\pi^-(\mu^+\mu^-)_{\text{fit}})$ using the logarithmic scale in Fig. 30. We observe that the distribution
 694 shown in the figure does not follow a simple exponential dependence on $M(\pi^+\pi^-(\mu^+\mu^-)_{\text{fit}})$
 695 in part because, as explained previously, the ISR spectrum in this MC sample is completely
 696 unreasonable.

697 We reskim the data and generic background MC, blind the signal region and present
 698 the data distributions of photon energy spectrum vs $M(\pi^+\pi^-(\mu^+\mu^-)_{\text{fit}})$ in Fig. 31 and
 699 $M(\pi^+\pi^-(\mu^+\mu^-)_{\text{fit}})$ in Fig. 32. We observe unambiguous signatures of $\Upsilon(2S)$ and $\Upsilon(3S)$
 700 ISR production. We also show the distribution of $M(\pi^+\pi^-(\mu^+\mu^-)_{\text{fit}})$ for blinded data in
 701 Figures 33 and 34 using the logarithmic scale. Note that the last figure is plotted using

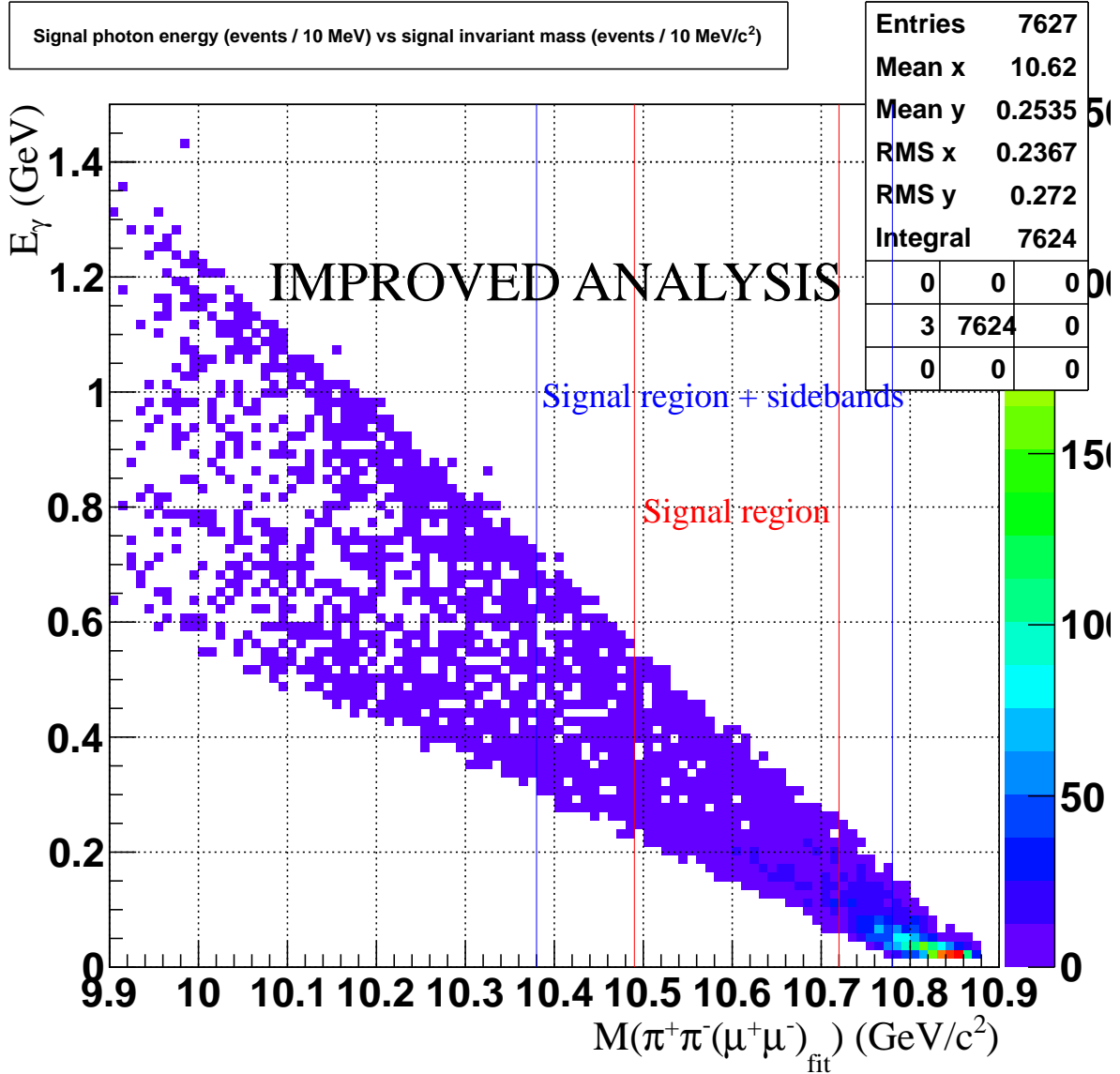


Figure 28: The reconstructed signal photon energy versus the invariant mass $M(\pi^+\pi^-(\mu^+\mu^-)_{\text{fit}})$ for a special ISR MC sample with relaxed selection criteria. Only best candidates are shown.

702 a finer bin width of $2 \text{ MeV}/c^2$ in a narrower range of the invariant mass. Using the data,
 703 we perform a rough estimate of the width of the peak seen at the nominal mass of $\Upsilon(3S)$,
 704 $10.355 \text{ GeV}/c^2$, corresponding to events originating from radiative return to $\Upsilon(3S)$. Using
 705 our estimate of $5 \text{ MeV}/c^2$ (consistent with our MC-based understanding of resolution), we
 706 conclude that events in the left sideband of Fig. 34 are at least 5 width units away from
 707 this peak. Hence, it is unlikely that events in our left sideband are from radiative return to
 708 $\Upsilon(3S)$.

709 In the next section we explain our fitting strategy for extracting the signal from data
 710 (when the permission to unblind is granted). We fit the data in the range of signal invariant
 711 mass $M(\pi^+\pi^-(\mu^+\mu^-)_{\text{fit}})$ between the two blue vertical lines shown in Figures 27–34, *i.e.*

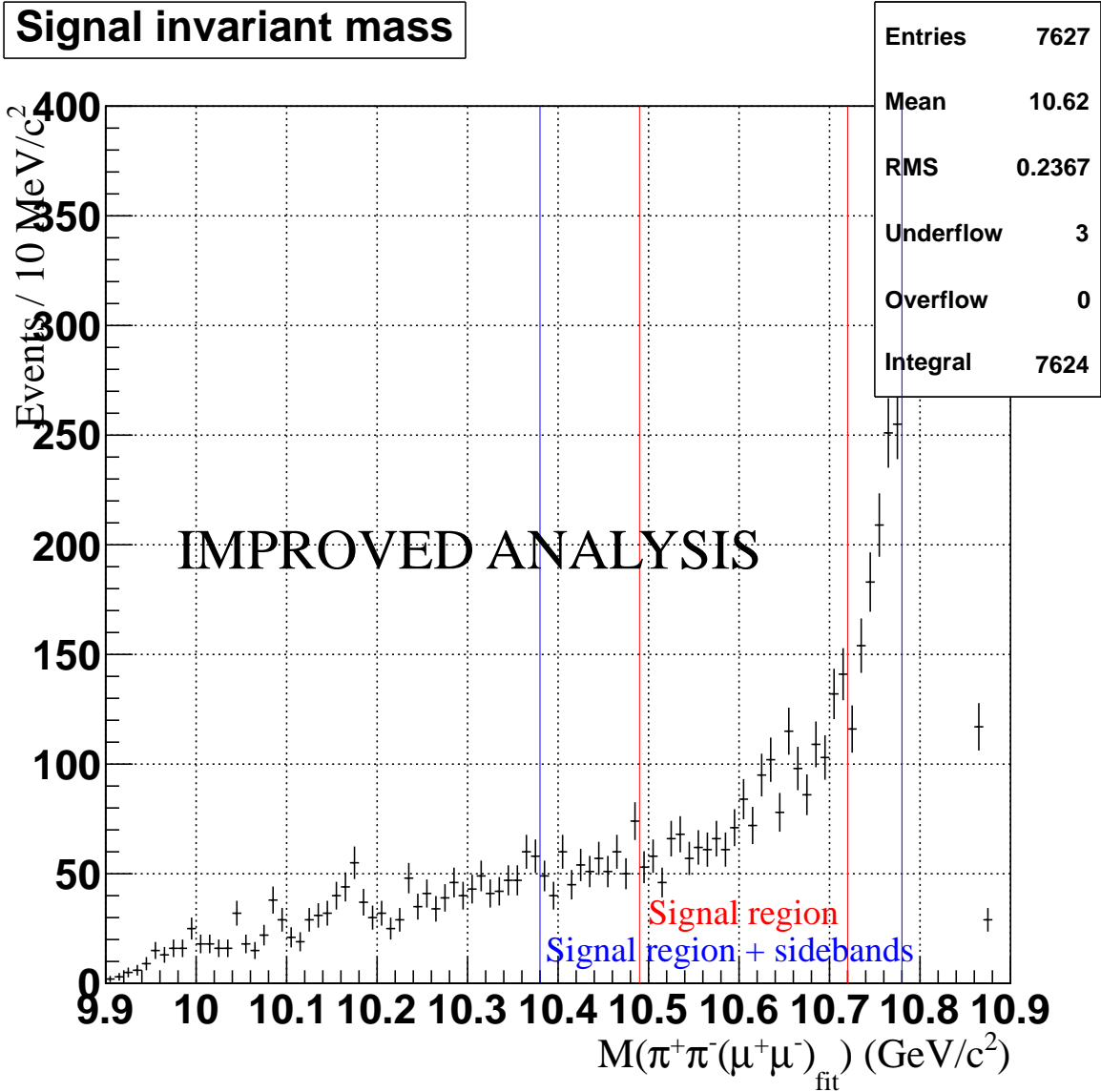


Figure 29: The reconstructed invariant mass $M(\pi^+\pi^-(\mu^+\mu^-)_{\text{fit}})$ for a special ISR MC sample with relaxed selection criteria. Only best candidates are shown.

712 in the range $10.38 \text{ GeV}/c^2 \leq M(\pi^+\pi^-(\mu^+\mu^-)_{\text{fit}}) \leq 10.78 \text{ GeV}/c^2$. This region of the
 713 invariant mass in blinded data is shown in Fig. 35.

714 Finally, to conclude this section, we present Figures 36–39, where we show the distri-
 715 butions of the energy of the signal photon candidate versus $M(\pi^+\pi^-(\mu^+\mu^-)_{\text{fit}})$ and the
 716 projections onto the $M(\pi^+\pi^-(\mu^+\mu^-)_{\text{fit}})$ invariant mass for our correctly reweighted ISR MC
 717 sample (described in section 6) for the decay $\Upsilon(5S) \rightarrow \Upsilon(1S)\pi^+\pi^-$.

718 10.3 Fitting Strategy

719 To extract the $W_{b,J}$ signal from the data or to estimate the upper limit on its production, we
 720 (plan to) fit the invariant mass distribution $M(\pi^+\pi^-(\mu^+\mu^-)_{\text{fit}})$ in data with the sum of an

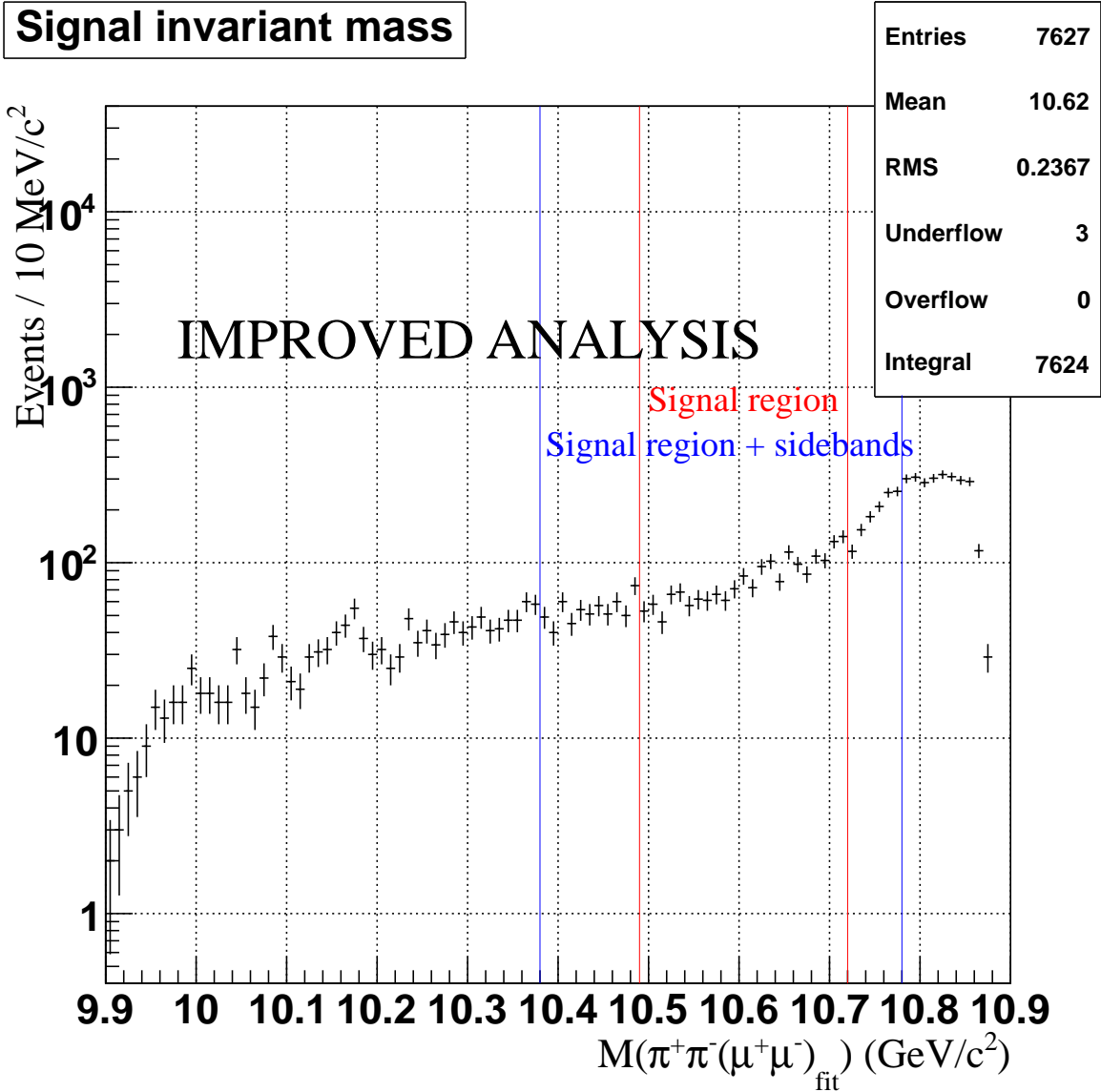


Figure 30: The reconstructed invariant mass $M(\pi^+\pi^-(\mu^+\mu^-)_{\text{fit}})$ for a special ISR MC sample with relaxed selection criteria shown using the logarithmic scale. The ISR spectrum in this special MC sample has an unreasonable shape and could not be described by an exponential. Only best candidates are shown.

721 exponential, a straight line of zero or positive slope and the model for the signal shown in
 722 Fig. 21a. We plan to perform such fits for the values of (fixed) nominal mass of W_{bJ} between
 723 10.5 and 10.7 GeV/c² in steps of a few MeV/c². Important reference points here are provided
 724 by the invariant masses of Z_B and Z'_b which are, respectively, 10.610 and 10.650 GeV/c². We
 725 expect (or, rather, M. Voloshin expects) W_{bJ} to be roughly as wide (or narrow) as $Z_b^{(l)}$. This
 726 makes our life easier. Each fit will be performed independently. The shape of background
 727 distribution will be obtained from the data including the signal region. In our opinion, we
 728 can not obtain the shape of background exclusively from the sidebands because our sidebands

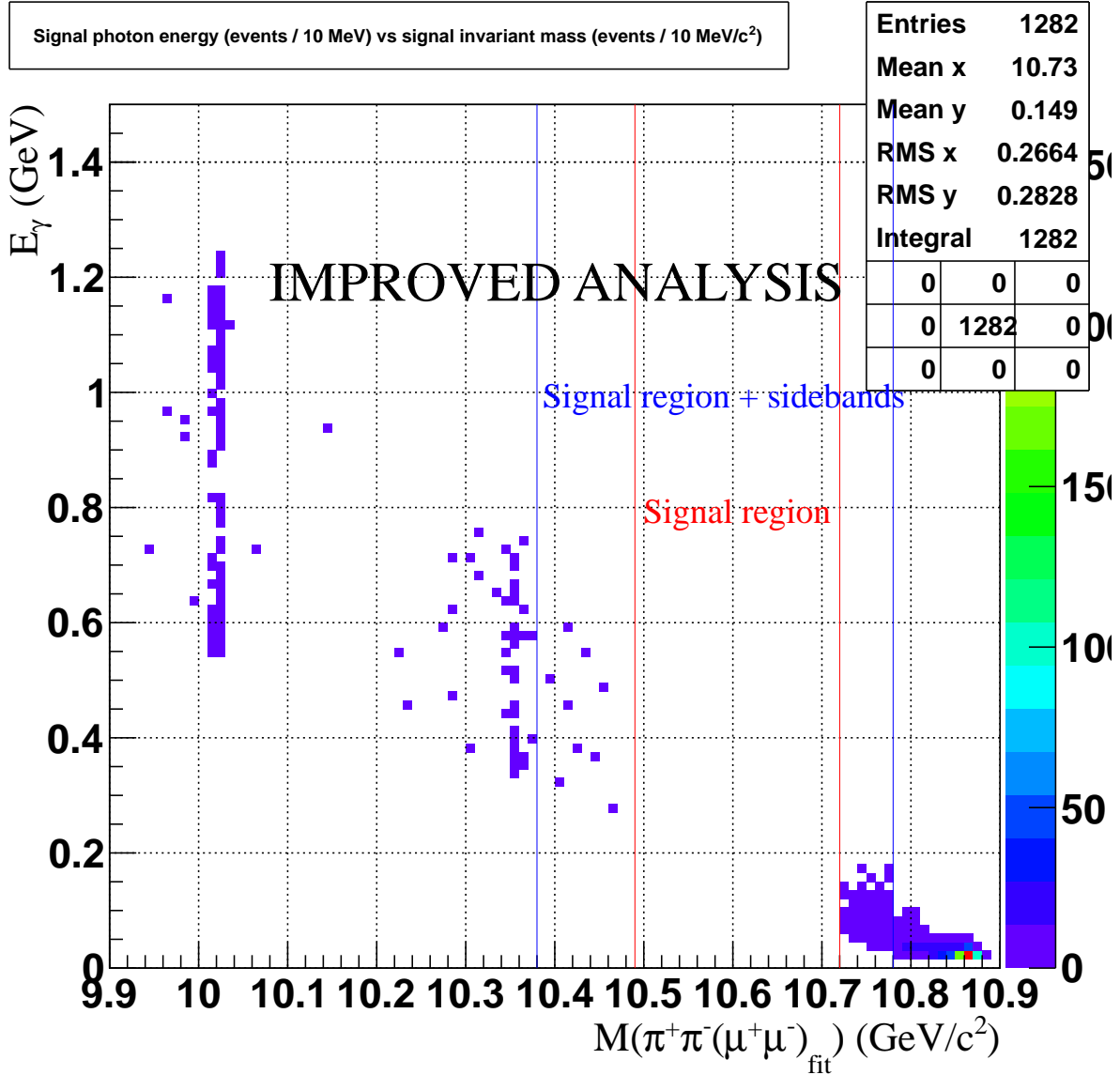


Figure 31: The reconstructed signal photon energy versus the invariant mass $M(\pi^+\pi^-(\mu^+\mu^-)_{\text{fit}})$ for blinded data with relaxed selection criteria. Only best candidates are shown.

729 are relatively narrow and, also, if the shape of the background function is fixed using our
 730 sidebands, fitting with the model described in this section could easily introduce a significant
 731 bias in the results of the fit. Another limitation comes from the wide range of the invariant
 732 mass region where we are searching for the W_{bJ} . For each individual fit (with a particular
 733 hypothesis for W_{bJ} mass), the effective sideband region is going to be significantly wider than
 734 in our exercises discussed in this section. The key assumptions are: 1) there are no peaking
 735 backgrounds in the entire signal region, and 2) backgrounds can be modeled by the sum of
 736 an exponential and a straight line. Our confidence is based on MC studies using, first of all,
 737 our ISR MC samples.

738 We fit the invariant mass $M(\pi^+\pi^-(\mu^+\mu^-)_{\text{fit}})$ in the range between $10.38 \text{ GeV}/c^2 \leq$

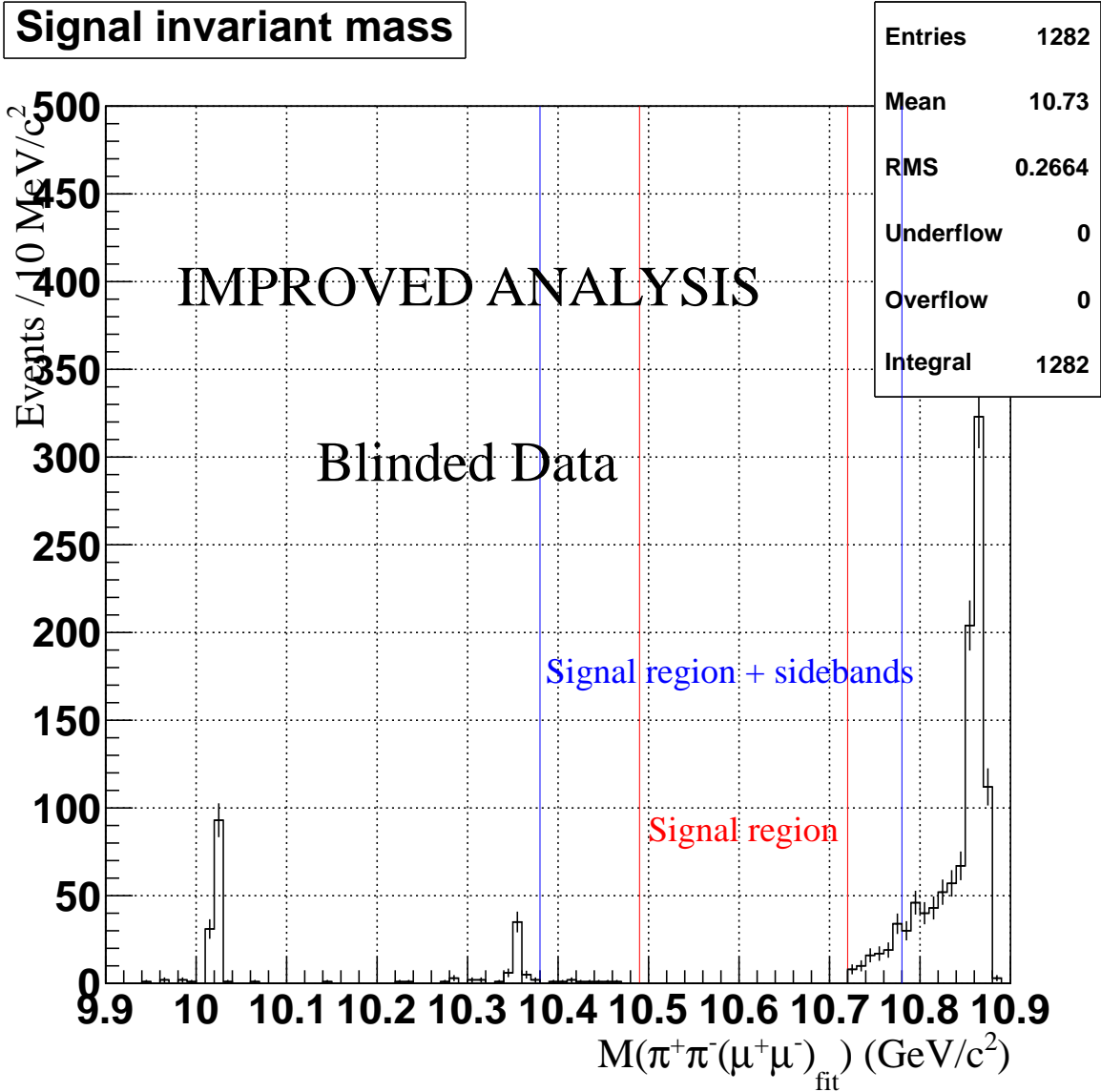


Figure 32: The reconstructed invariant mass $M(\pi^+\pi^-(\mu^+\mu^-)_{\text{fit}})$ for blinded data with relaxed selection criteria. Only best candidates are shown.

739 $M(\pi^+\pi^-(\mu^+\mu^-)_{\text{fit}}) \leq 10.78 \text{ GeV}/c^2$. In principle, we can (significantly) extend the invariant
 740 mass included in the fit toward smaller values (therefore including the radiative production
 741 of $\Upsilon(3S)$ or even $\Upsilon(2S)$ in our fits), however, it is not clear to us if this would necessarily
 742 help us understand the shape of the background and to reduce the uncertainty in our model
 743 description of the data in the signal region.

744 In this section we show some of the results of our unbinned extended maximum likelihood
 745 fits to $M(\pi^+\pi^-(\mu^+\mu^-)_{\text{fit}})$ using a model implemented using RooFit for various MC samples
 746 under different conditions.

747 We start our adventure by fitting the distribution of properly reweighted ISR MC sample
 748 for the decay $\Upsilon(5S) \rightarrow \Upsilon(1S)\pi^+\pi^-$ shown in Fig. 39. We fit this distribution using the
 749 unbinned extended maximum likelihood technique implemented in RooFit with the sum of

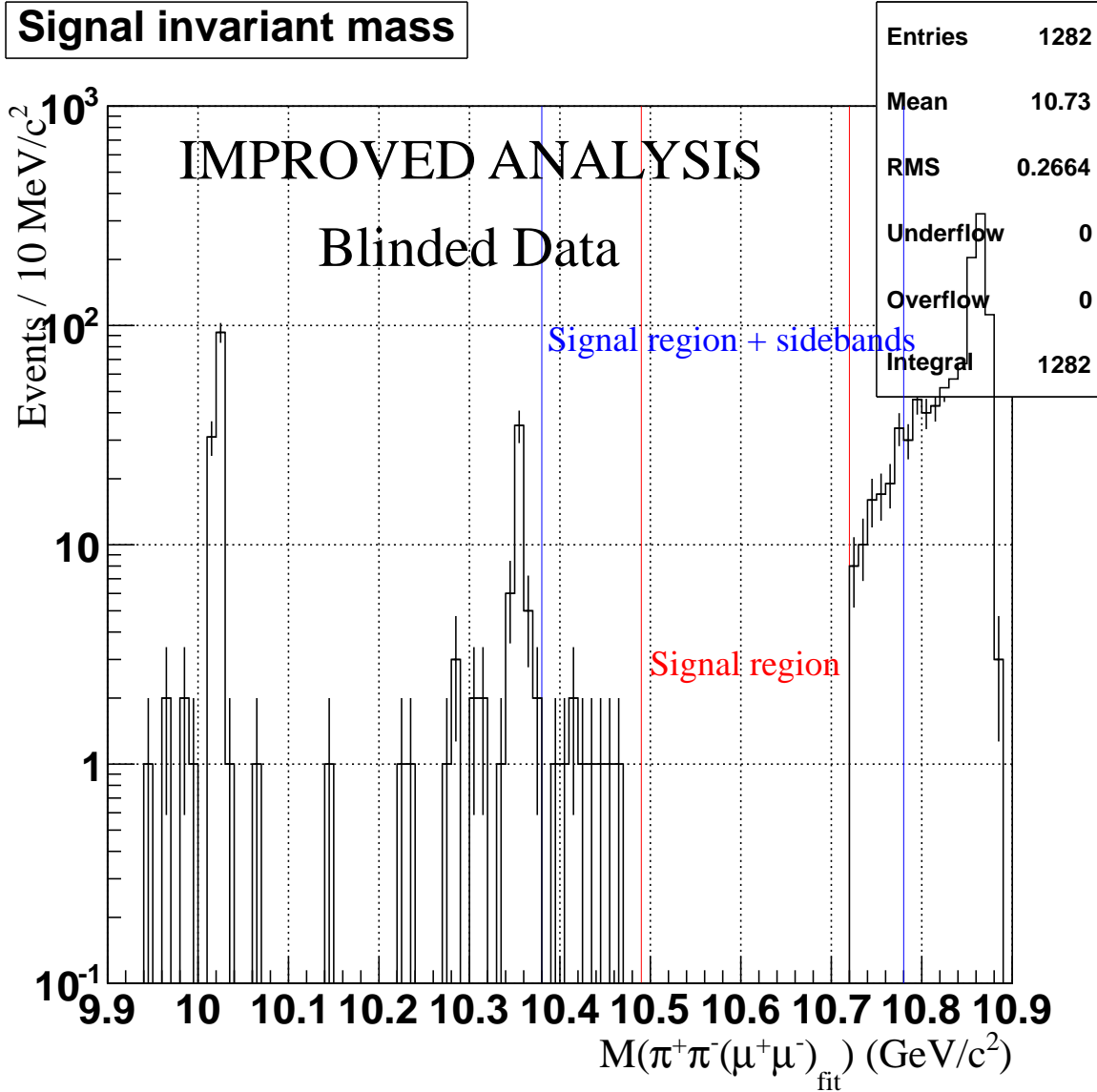


Figure 33: The reconstructed invariant mass $M(\pi^+\pi^-(\mu^+\mu^-)_{\text{fit}})$ for blinded data with relaxed selection criteria plotted using the logarithmic scale. This is the same distribution as shown in Fig. 32. Only best candidates are shown.

750 an exponential and a straight line of zero or positive slope (if the curious reader really wants
 751 to know, we use `RooChebychev` for the latter). The results of this fit are shown in Fig. 40.
 752 We show the results of the fit using both the linear and the logarithmic scales because while
 753 one PDF is linear when plotted on log scale, the other PDF is, surprise, linear when plotted
 754 on linear scale because it is a line! Note that the fit has four parameters: α is the parameter
 755 of the exponent, `slope` is the slope of the straight line, $N1$ and $N2$ are the numbers of
 756 events obtained from the fit for background contributions parameterized by the exponent
 757 and the straight line, respectively. Note that we can not replace these two parameters by
 758 a single fraction parameter in an **extended** ML fit. When we fit real data, we plan to let
 759 the relative contributions from the two PDFs to be independently varying parameters in

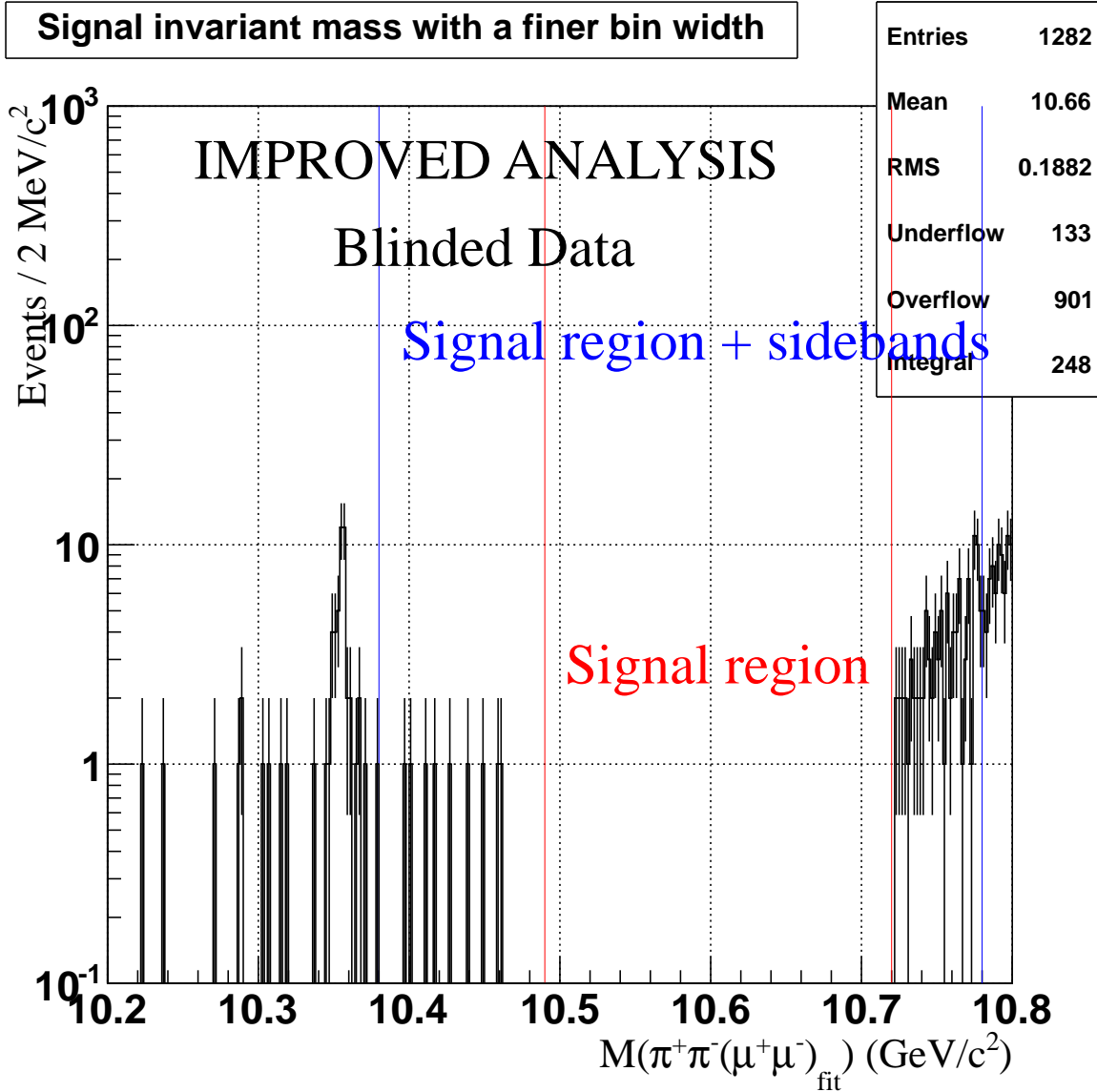


Figure 34: The reconstructed invariant mass $M(\pi^+\pi^-(\mu^+\mu^-)_{\text{fit}})$ for blinded data with relaxed selection criteria plotted using the logarithmic scale for a narrower region of the invariant mass using a finer bin width than used for plots shown in Figures 32 and 33. Only best candidates are shown.

760 the fit, same way it is the case in fits described here. This degree of freedom could be used
 761 to approximate (a small contribution, as we conclude from studying the sidebands) from
 762 non-peaking background possibly present in data in the signal region.

763 In the next step we exclude events in the signal region from the fit and repeat the
 764 described exercise for the same ISR MC sample. The results are shown in Fig. 41. One can
 765 easily notice that our sidebands are not sufficiently wide to use these to obtain the shape of
 766 background in the **entire** signal region. This is the reason why, when fitting the data, these
 767 two PDFs, an exponential and a straight line, will be combined with a signal PDF. In either
 768 case, one can see that presence of ISR definitely introduces a large systematic uncertainty in

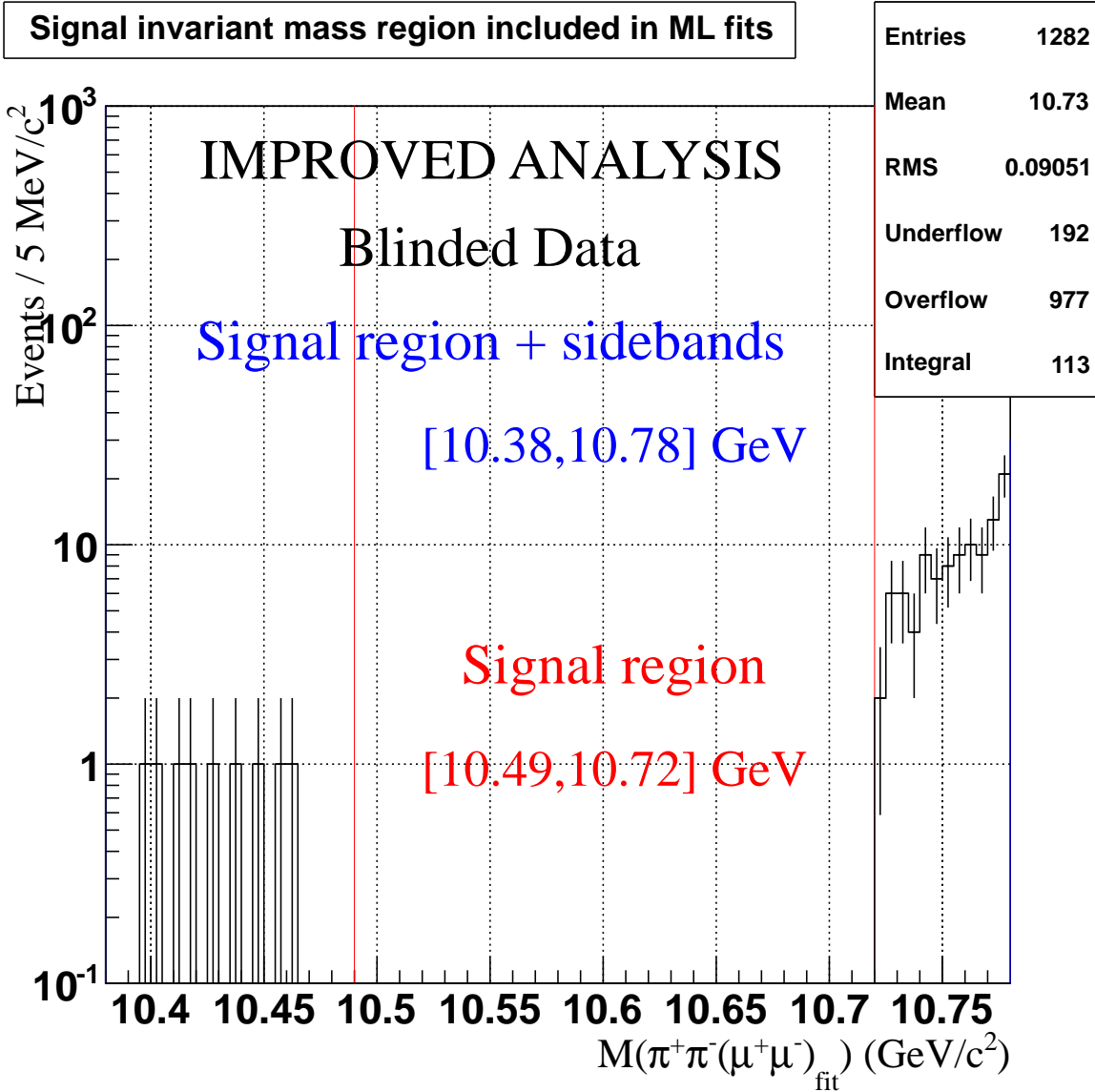


Figure 35: The reconstructed invariant mass $M(\pi^+\pi^-(\mu^+\mu^-)_{\text{fit}})$ for blinded data with relaxed selection criteria plotted using the logarithmic scale for the region of the invariant mass included in the fits. Same events are shown as in Figures 32–34 but using a different bin width. Only best candidates are shown.

769 our results for (relatively) larger invariant masses of W_{bJ} , in the region where the exponential
 770 contribution is rapidly increasing.

771 Now we try to fit the blinded data (just to see if the fit is going to converge at all).
 772 The results of the fit are shown in Fig. 42. Again, we observe that it would be unrealistic
 773 to expect our sidebands to predict the background in the entire, 400 MeV/c²-wide signal
 774 region.

775 Now we try to fit our precious ISR MC sample using three PDFs: the exponential
 776 and the straight line approximating background and the signal line shape shown in Fig. 21a
 777 (convolution of the signal Breit-Wigner with two Gaussians prepared using FFT plug-in in

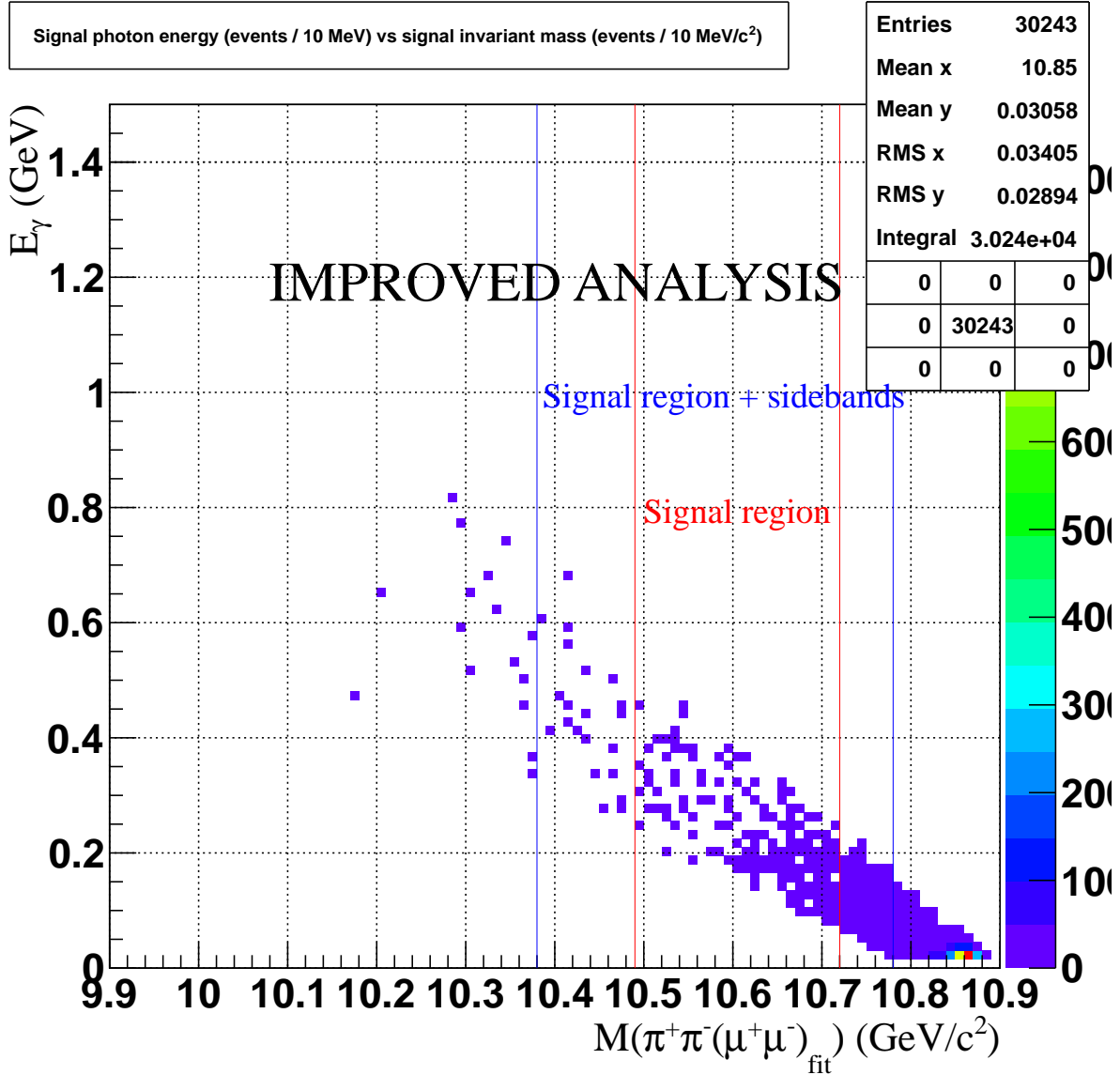


Figure 36: The reconstructed signal photon energy versus the invariant mass $M(\pi^+\pi^-(\mu^+\mu^-)_{\text{fit}})$ for ISR MC sample described in section 6 with relaxed selection criteria. Only best candidates are shown.

778 ROOT). Note that no signal MC events have been added to the pure ISR MC sample yet.
 779 The number of signal events (NS) is an additional parameter in the fit, but the shape of
 780 the signal and its location (*i.e.* the invariant mass of W_{bJ} set at $10.6 \text{ GeV}/c^2$) are fixed
 781 in this fit. As you can see in Fig. 43 the fit finds no statistically significant signal. Note
 782 that the solid green curve superimposed on the results of the fit shows how 50 signal events
 783 would look on average according to signal PDF description. The result of the fit for NS is
 784 a negative fluctuation.

785 Inspired by our success, we now ask the fitter to search for the signal (where there is
 786 none) in ISR MC sample. To do so we let the nominal mass of the W_{bJ} float in the range
 787 between 10.5 and $10.7 \text{ GeV}/c^2$. Note that in our future fits to data we plan to **scan** through

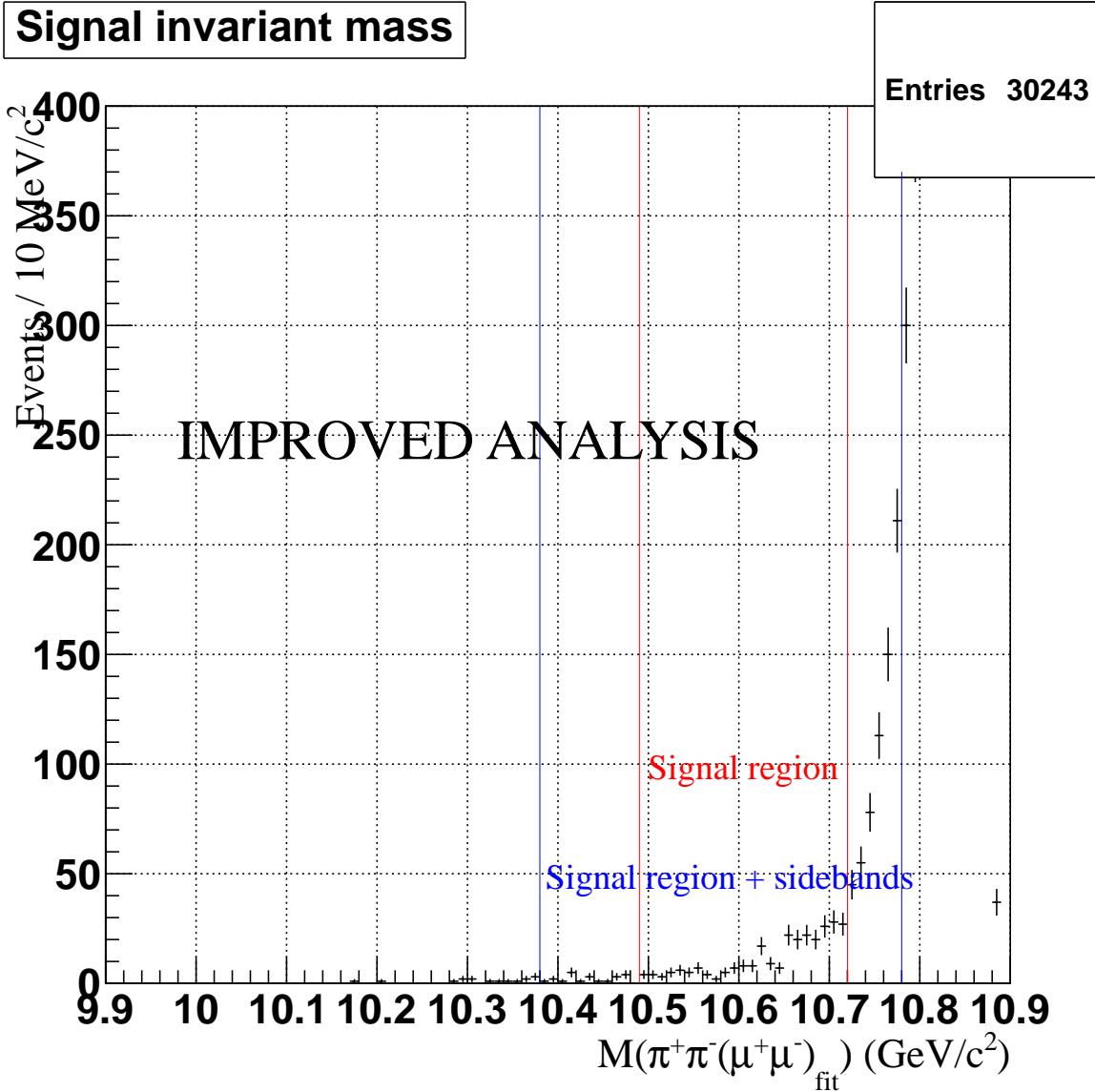


Figure 37: The reconstructed invariant mass $M(\pi^+\pi^-(\mu^+\mu^-)_{\text{fit}})$ for ISR MC sample described in section 6 with relaxed selection criteria. Only best candidates are shown.

788 this interval of $M(\pi^+\pi^-(\mu^+\mu^-)_{\text{fit}})$, however, for the fit performed here we simply want to
 789 see the significance of the worst-case-scenario when the fit “discover” a signal where there
 790 is none. The results of this fit are shown in Fig. 44. Indeed, an obvious enhancement
 791 in the distribution of $M(\pi^+\pi^-(\mu^+\mu^-)_{\text{fit}})$ is “picked-up” by the fitter as the most likely
 792 “signal”, however, as you can observe from the results of the fit, statistical significance of
 793 this “discovery” is consistent with a fluctuation. Such results are also likely to be obtained
 794 in the data, and, in case of low significance and no discovery, this would blow up the upper
 795 limit estimate.

796 Finally, being brave young pioneers, we decide to tackle a simulated data sample where
 797 50 events (with $W_{b,J}$ mass of $10.620 \text{ GeV}/c^2$) are randomly selected from one of our simulated
 798 signal MC sample and are added to the same ISR MC sample we are using for all our fits

Signal invariant mass

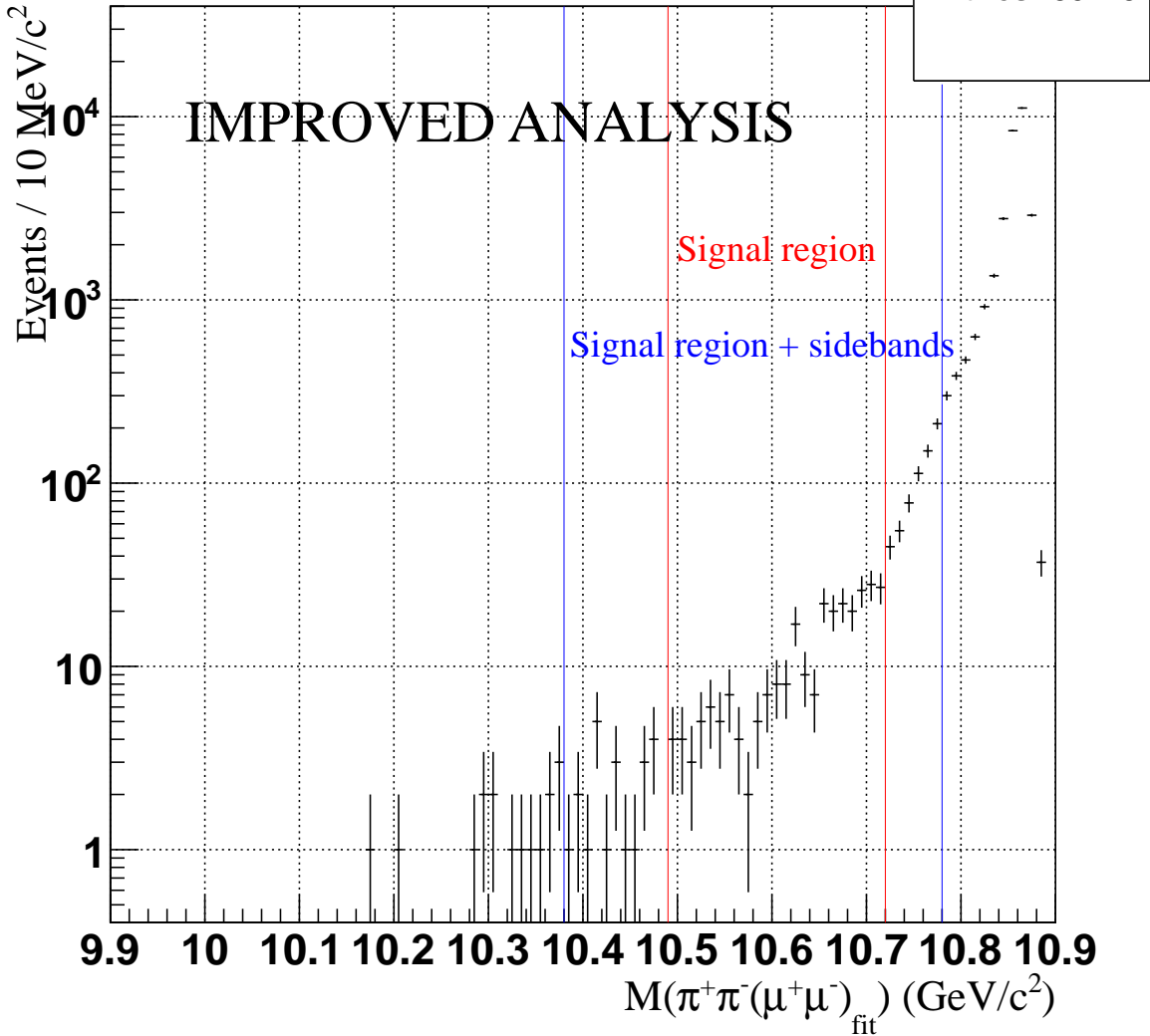


Figure 38: The reconstructed invariant mass $M(\pi^+\pi^-(\mu^+\mu^-)_{\text{fit}})$ for ISR MC sample described in section 6 with relaxed selection criteria shown using the logarithmic scale. Only best candidates are shown.

799 described in this section. We let the fitter search for this signal and report the results in
 800 Fig. 45. The fitter finds the signal of the right magnitude. We conclude that our fitting
 801 procedure is working.

802 Now knowing that our fitting procedure works, we perform a scan on our reweighted ISR
 803 MC sample for the decay $\Upsilon(5S) \rightarrow \Upsilon(1S)\pi^+\pi^-$, holding the nominal mass of W_{bJ} fixed for
 804 values between 10.5 and 10.7 GeV/c^2 in steps of a 5 MeV/c^2 . The results of the scan are
 805 shown in Fig. 46.

806 We perform another (identical) scan on our reweighted ISR MC sample, but this time,
 807 we include 50 toy MC signal events generated from our signal PDF (with the signal mass
 808 fixed at values between 10.5 and 10.7 GeV/c^2 in steps of a 5 MeV/c^2 . The results of the

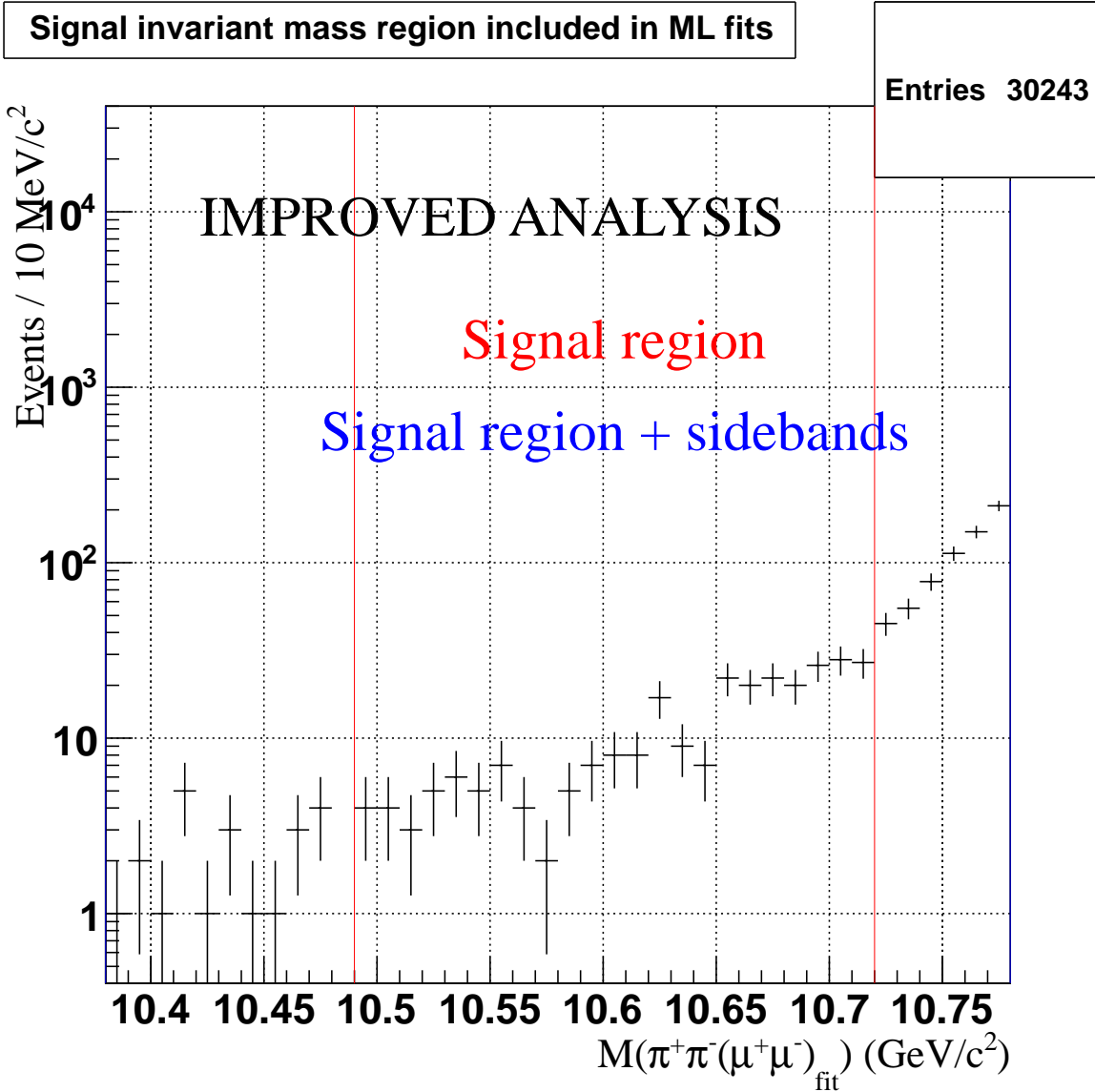


Figure 39: The reconstructed invariant mass $M(\pi^+\pi^-(\mu^+\mu^-)_{\text{fit}})$ for ISR MC sample described in section 6 with relaxed selection criteria shown using the logarithmic scale for the mass region used in the fits. Only best candidates are shown.

809 scan are shown in Fig. 47.

810 Finally, blind data contain 9 events in the lower-mass sideband and 104 events in the
 811 higher-mass sideband, while ISR MC has 22 events in the lower-mass sideband and 652
 812 events in the higher-mass sideband. On basis of this comparison we conclude that our ISR
 813 MC sample is larger than the statistics in data. Therefore, future fits to data will likely yield
 814 results which are more competitive than the estimates shown in this section.

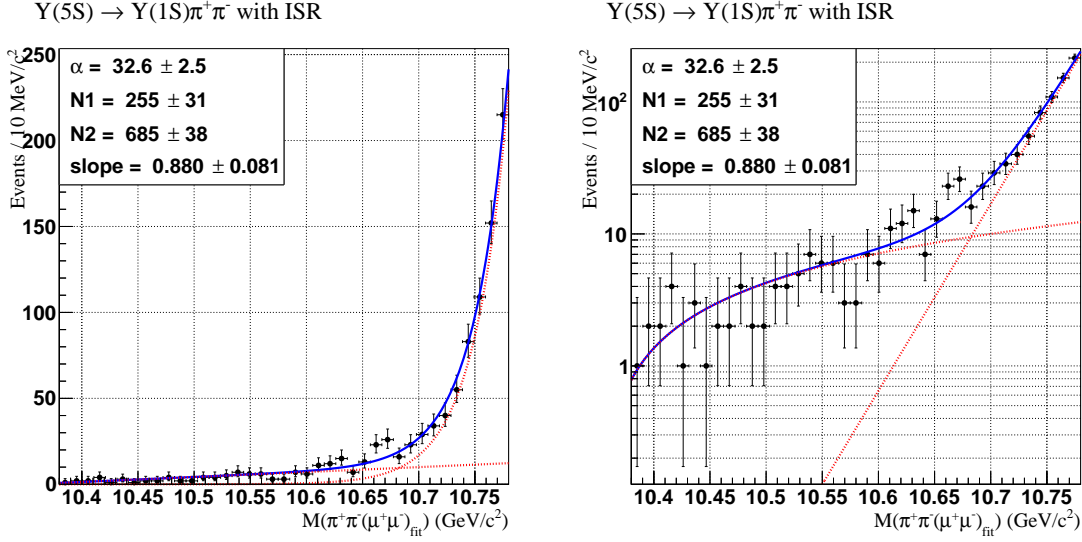


Figure 40: The results of the ML fit for ISR MC sample.

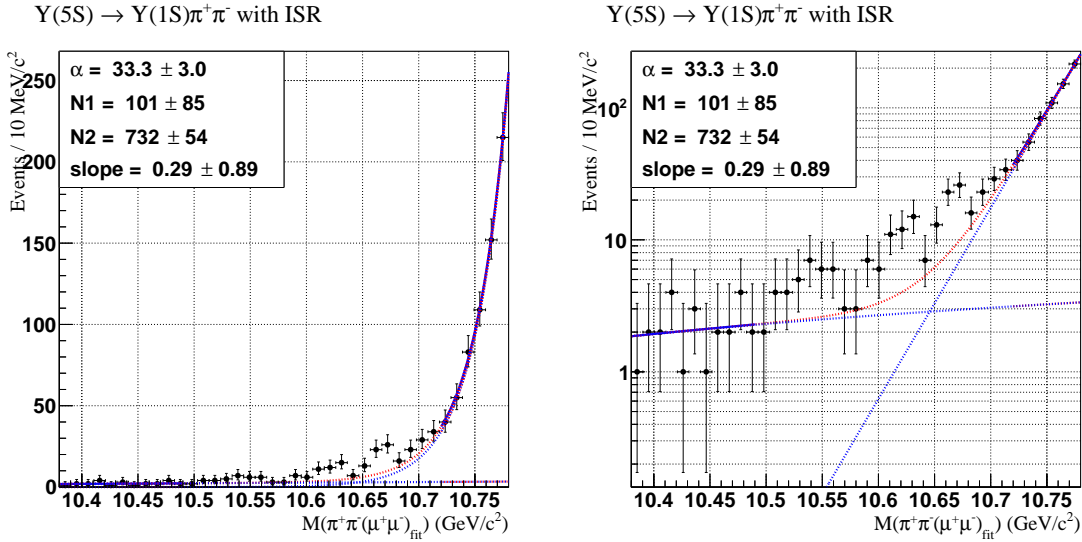


Figure 41: The results of the ML fit for ISR MC sample excluding the signal region.

References

815

816

817

818

819

820

821

- [1] A. Bondar et al. Observation of two charged bottomonium-like resonances in $Y(5S)$ decays. *Phys. Rev. Lett.*, 108:122001, 2012.
- [2] I. Adachi et al. Evidence for a $Z_b^0(10610)$ in Dalitz analysis of $Y(5S) \rightarrow Y(nS)\pi^0\pi^0$. 2012.
- [3] P. Krokovny et al. First observation of the $Z_b^0(10610)$ in a Dalitz analysis of $Y(10860) \rightarrow Y(nS)\pi^0\pi^0$. *Phys. Rev.*, D88(5):052016, 2013.

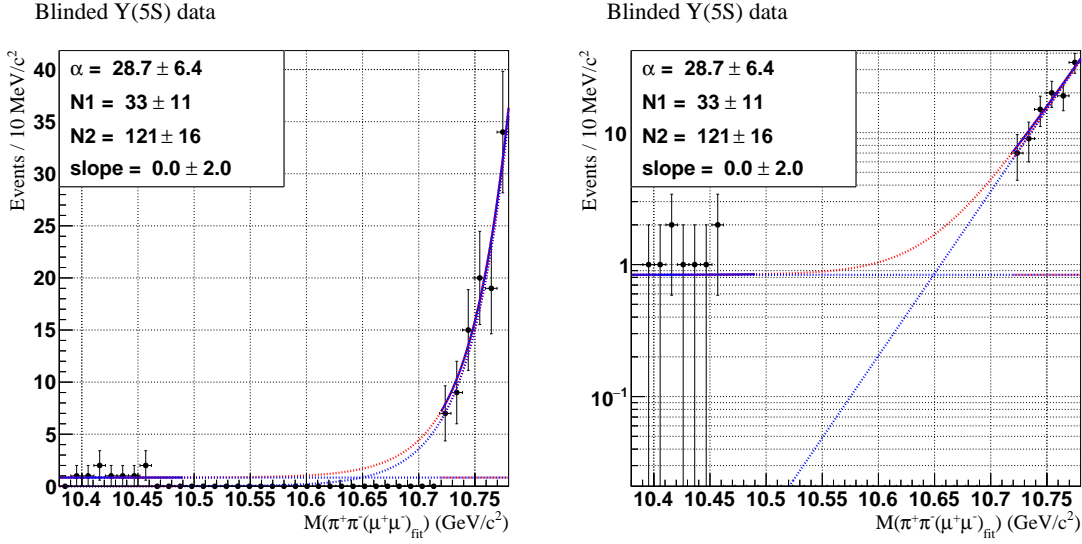


Figure 42: The results of the ML fit for sidebands of the blinded data sample.

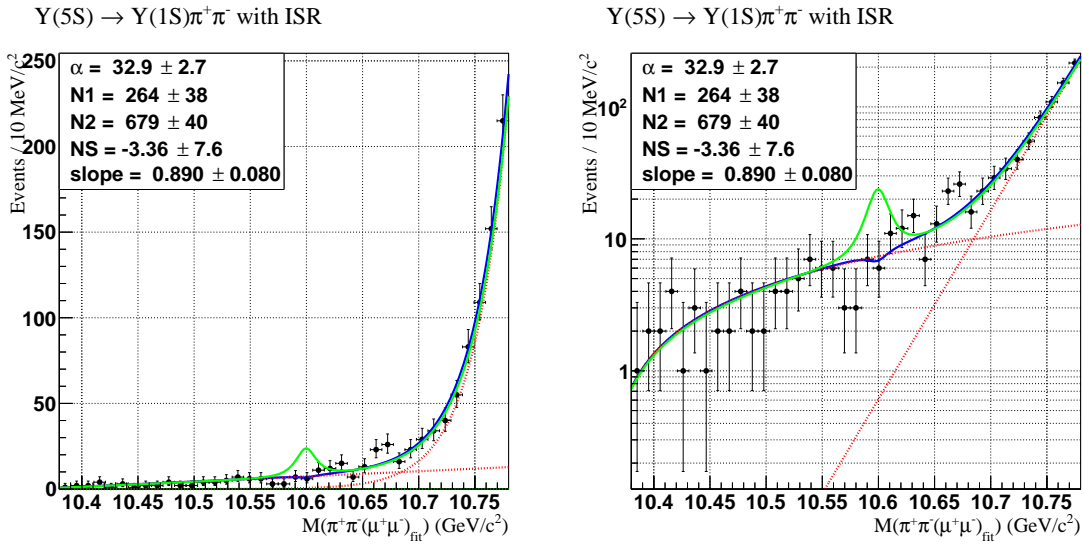


Figure 43: The results of the ML fit for ISR MC sample with background model and signal PDF shape.

- 822 [4] A. Garmash et al. Observation of $Z_b(10610)$ and $Z_b(10650)$ Decaying to B Mesons.
823 *Phys. Rev. Lett.*, 116(21):212001, 2016.
- 824 [5] L. M. Lederman. The discovery of the Upsilon, bottom quark, and B mesons. In
825 *The Rise of the standard model: Particle physics in the 1960s and 1970s. Proceedings,*
826 *Conference, Stanford, USA, June 24-27, 1992*, pages 101–113, 1992.
- 827 [6] M. Tanabashi et al. Review of Particle Physics. *Phys. Rev.*, D98(3):030001, 2018.
- 828 [7] S. Godfrey and N. Isgur. Mesons in a Relativized Quark Model with Chromodynamics.
829 *Phys. Rev.*, D32:189–231, 1985.

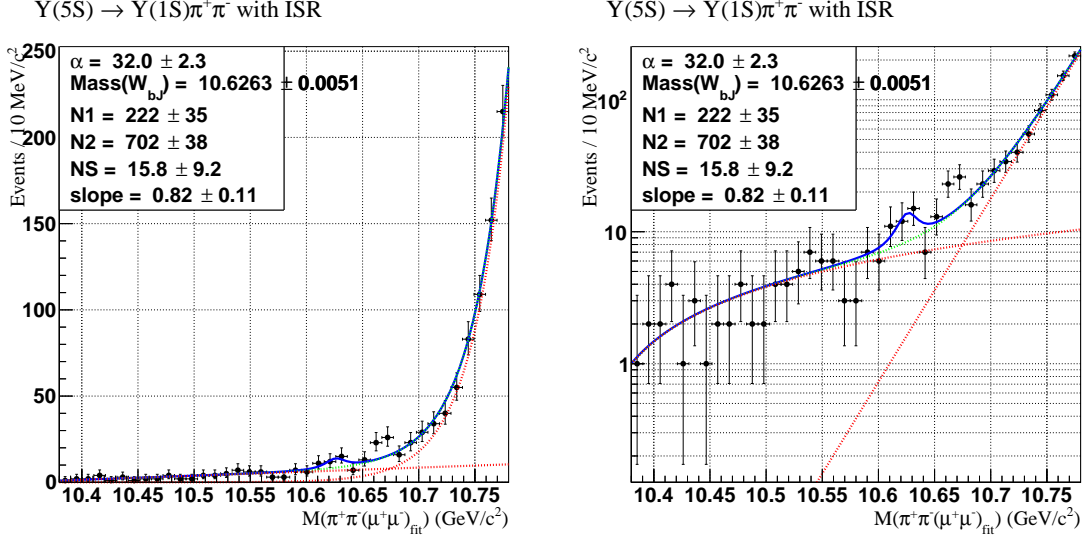


Figure 44: The results of the ML fit for ISR MC sample with background model and signal PDF shape (mass is a free parameter).

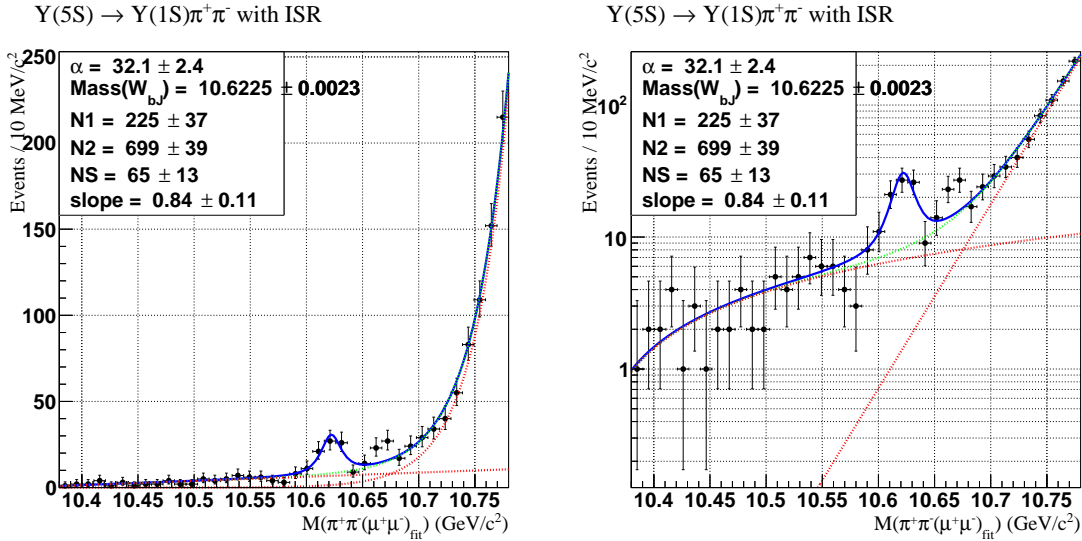


Figure 45: The results of the ML fit for ISR + signal (50 events) MC sample with background model and signal PDF shape (mass is a free parameter).

830 [8] S. Godfrey and K. Moats. Bottomonium Mesons and Strategies for their Observation.
 831 *Phys. Rev.*, D92(5):054034, 2015.

832 [9] S. Godfrey, K. Moats, and E. S. Swanson. B and B_s Meson Spectroscopy. *Phys. Rev.*,
 833 D94(5):054025, 2016.

834 [10] A. E. Bondar, R. V. Mizuk, and M. B. Voloshin. Bottomonium-like states: Physics case
 835 for energy scan above the $B\bar{B}$ threshold at Belle-II. *Mod. Phys. Lett.*, A32(04):1750025,
 836 2017.

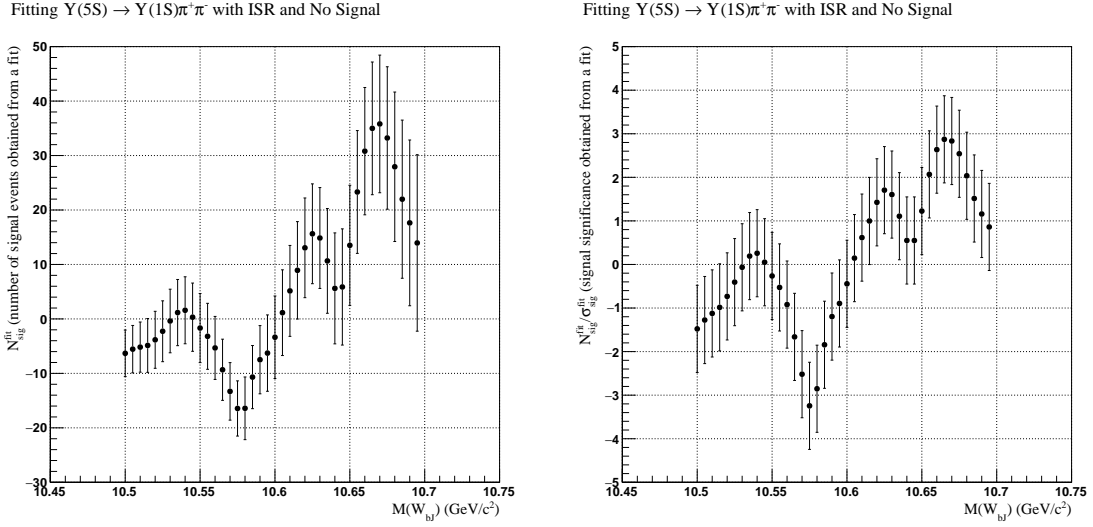


Figure 46: The results of the scan for ISR MC sample with background model and signal PDF shape.

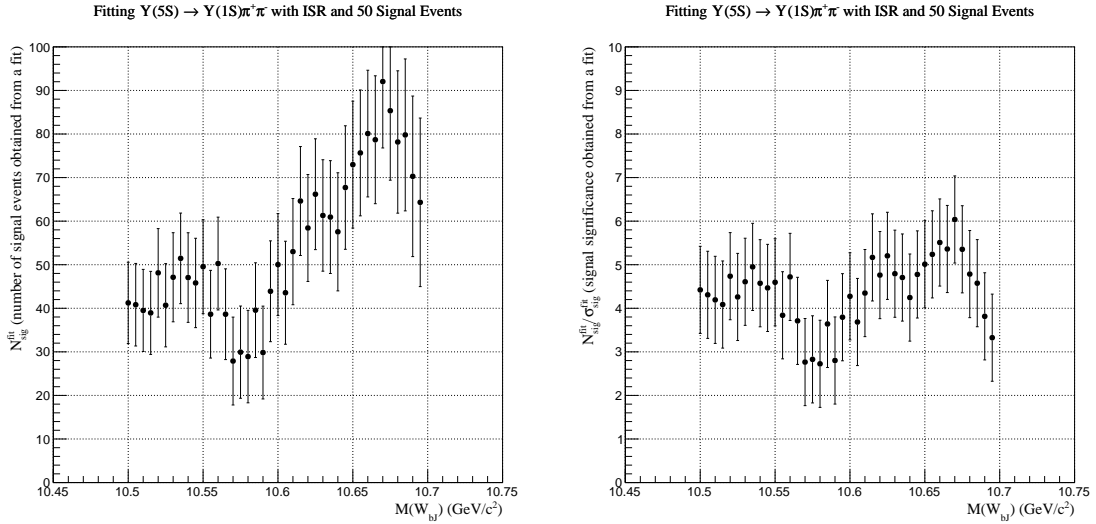


Figure 47: The results of the scan for ISR MC sample + 50 toy MC signal events with background model and signal PDF shape.

- 837 [11] A. E. Bondar, A. Garmash, A. I. Milstein, R. Mizuk, and M. B. Voloshin. Heavy quark
838 spin structure in Z_b resonances. *Phys. Rev.*, D84:054010, 2011.
- 839 [12] Stephen Lars Olsen. A New Hadron Spectroscopy. *Front. Phys.(Beijing)*, 10(2):121–154,
840 2015.
- 841 [13] M. B. Voloshin. Radiative transitions from Upsilon(5S) to molecular bottomonium.
842 *Phys. Rev.*, D84:031502, 2011.
- 843 [14] W. Altmannshofer et al. The Belle II Physics Book, arXiv:hep-ex/1808.10567, 2018.

- 844 [15] I. Adachi et al. Study of Three-Body $Y(10860)$ Decays, arXiv:hep-ex/1209.6450,
845 BELLE-CONF-1272, 2012.
- 846 [16] D. J. Lange. The EvtGen particle decay simulation package. *Nucl. Instrum. Meth.*,
847 A462:152–155, 2001.
- 848 [17] S. Agostinelli et al. GEANT4: A Simulation toolkit. *Nucl. Instrum. Meth.*, A506:250–
849 303, 2003.
- 850 [18] A. Ryd, D. Lange, N. Kuznetsova, S. Versille, M. Rotondo, D. P. Kirkby, F. K. Wuerth-
851 wein, and A. Ishikawa. EvtGen: A Monte Carlo Generator for B -Physics. 2005.
- 852 [19] E. Barberio and Z. Was. PHOTOS: A Universal Monte Carlo for QED radiative cor-
853 rections. Version 2.0. *Comput. Phys. Commun.*, 79:291–308, 1994.
- 854 [20] J. Brodzicka et al. Physics Achievements from the Belle Experiment. *PTEP*,
855 2012:04D001, 2012.
- 856 [21] M. Benayoun, S. I. Eidelman, V. N. Ivanchenko, and Z. K. Silagadze. Spectroscopy at B
857 factories using hard photon emission. *Mod. Phys. Lett.*, A14:2605–2614, 1999. [Frascati
858 Phys. Ser.15(1999)].
- 859 [22] Wouter Verkerke and David P. Kirkby. The RooFit toolkit for data modeling. *eConf*,
860 C0303241:MOLT007, 2003. [186(2003)].